

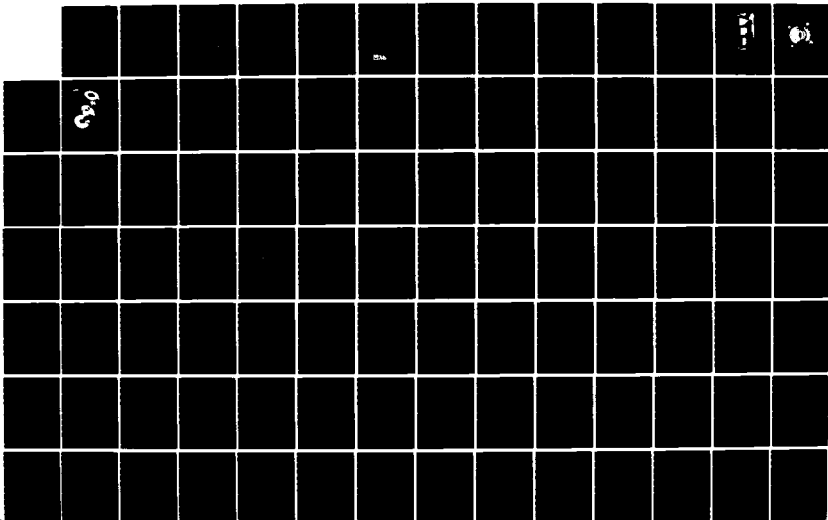
AD-A151 081 COUPLING BETWEEN VELOCITY OSCILLATIONS AND SOLID PROPELLANT COMBUSTION. (U) UNITED TECHNOLOGIES CORP SUNNYVALE CA CHEMICAL SYSTEMS DIV R S BROWN ET AL.

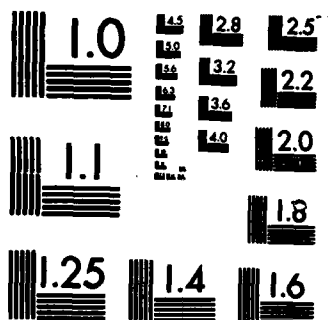
1/2

AUG 84 CSD-2749-AR-3 AFOSR-TR-85-0100

F/G 21/8. 2

NL





MICROCOPY RESOLUTION TEST CHART
NATIONAL BUREAU OF STANDARDS-1963-A

④

AD-A151 081

CSD 2749-AR-3

COUPLING BETWEEN VELOCITY OSCILLATIONS
AND SOLID PROPELLANT COMBUSTION

Final
Annual Progress Report

August 1984

DTIC FILE COPY

DTIC
ELECTE
MAR 05 1985
S
E

Not for public release;
unclassified.

85 02 20 003

4

CSD 2749-AR-3

**COUPLING BETWEEN VELOCITY OSCILLATIONS
AND SOLID PROPELLANT COMBUSTION**

Final
Annual Progress Report

August 1984

Prepared for

**DIRECTOR OF AEROSPACE SCIENCES
AIR FORCE OFFICE OF SCIENTIFIC RESEARCH
BOLLING AIR FORCE BASE
DISTRICT OF COLUMBIA 20332**

by

DTIC
ELECTE
S MAR 05 1985 **D**
E

R. S. Brown, A. M. Blackner, P. G. Willoughby, and R. Dunlap

The views and conclusions contained in this document are those of the authors and should not be interpreted as necessarily representing the official policies or endorsements, either expressed or implied, of the Air Force Office of Scientific Research or the U. S. Government.

AIR FORCE OFFICE OF SCIENTIFIC RESEARCH (AFSC)
NOTICE OF TRANSMITTAL TO DTIC
This technical report has been reviewed and is
approved for public release IAW AFR 190-12.
Distribution is unlimited.
MATTHEW J. KEEPER
Chief, Technical Information Division

UNCLASSIFIED

SECURITY CLASSIFICATION OF THIS PAGE (When Data Entered)

REPORT DOCUMENTATION PAGE		READ INSTRUCTIONS BEFORE COMPLETING FORM
1. REPORT NUMBER AFOSR-TR- 85 - 0 1 0 0	2. GOVT ACCESSION NO. AD A151 081	3. RECIPIENT'S CATALOG NUMBER
4. TITLE (and Subtitle) Coupling Between Velocity Oscillations and Solid Propellant Combustion		5. TYPE OF REPORT & PERIOD COVERED FINAL: 15 Mar 83 - 15 Aug 84
		6. PERFORMING ORG. REPORT NUMBER
7. AUTHOR(s) R. S. Brown, A. M. Blackner, P. G. Willoughby, and R. Dunlap		8. CONTRACT OR GRANT NUMBER(s) F49620-81-C-0027
9. PERFORMING ORGANIZATION NAME AND ADDRESS United Technologies/Chemical Systems Division P. O. Box 50010 San Jose, CA 95150-0015		10. PROGRAM ELEMENT, PROJECT, TASK AREA & WORK UNIT NUMBERS 61102F 2308/A1
11. CONTROLLING OFFICE NAME AND ADDRESS Air Force Office of Scientific Research/NA Bolling AFB DC 20332-6448		12. REPORT DATE August 1984
		13. NUMBER OF PAGES
14. MONITORING AGENCY NAME & ADDRESS (if different from Controlling Office)		15. SECURITY CLASS. (of this report) Unclassified
		15a. DECLASSIFICATION DOWNGRADING SCHEDULE
16. DISTRIBUTION STATEMENT (of this Report) Approved for public release; distribution unlimited		
17. DISTRIBUTION STATEMENT (of the abstract entered in Block 20, if different from Report)		
18. SUPPLEMENTARY NOTES (Fr 1473B)		
19. KEY WORDS (Continue on reverse side if necessary and identify by block number) → Velocity Coupling, and → Combustion Instability ←		
20. ABSTRACT (Continue on reverse side if necessary and identify by block number) Studies are being conducted to define and characterize the basic fluid mechanics and heat transfer mechanism controlling the coupling between acoustic and radial profiles of the mean and oscillatory velocity are being measured at several axial stations in a cold flow rocket simulator. Recent studies have concentrated on measuring the structure of the acoustic waves and how this structure relates to the oscillatory heat flux data reported earlier. In particular, the radial profiles of the magnitude and phase.		

DD FORM 1 JAN 73 1473 EDITION OF 1 NOV 65 IS OBSOLETE

UNCLASSIFIED

1 SECURITY CLASSIFICATION OF THIS PAGE (When Data Entered)

UNCLASSIFIED

SECURITY CLASSIFICATION OF THIS PAGE(When Data Entered)

cont.
20. Abstract

(relative to the head end acoustic pressure) of the acoustic velocity have been measured at several axial stations.)

At low acoustic pressures (i.e., 0.05%) the acoustic waves extend across the entire cross-section in the region upstream of the transition in the mean velocity profile. Nonplanar and nonlinear behavior is also observed in the near surface regions. Downstream of the velocity transition, the acoustic waves do not penetrate through the near wall turbulence. At higher acoustic pressures (i.e., 0.4%) the upstream nonlinearities increase in magnitude and extend across the entire port. Downstream of the velocity transition the core nonlinearities decay while the linear component penetrates through the turbulence to the wall. *Originator-Supplied Keywords include;*

(to 1473A)

B.

UNCLASSIFIED

CSD 2749-AR-3

COUPLING BETWEEN VELOCITY OSCILLATIONS
AND SOLID PROPELLANT COMBUSTION

Annual ~~Progress~~ Report

August 1984

Prepared for

DIRECTOR OF AEROSPACE SCIENCES
AIR FORCE OFFICE OF SCIENTIFIC RESEARCH
BOLLING AIR FORCE BASE
DISTRICT OF COLUMBIA 20332

by

R.S. Brown, A.M. Blackner, P.G. Willoughby and R. Dunlap



Accession For	
NTIS GRA&I	<input checked="checked" type="checkbox"/>
DTIC TAB	<input type="checkbox"/>
Unannounced	<input type="checkbox"/>
Justification	
By	
Distribution/	
Availability Codes	
Dist	Avail and/or Special
A-1	



TABLE OF CONTENTS

<u>Section</u>	<u>Page</u>
1.0 INTRODUCTION	1
2.0 EXPERIMENTAL STUDIES	3
2.1 Apparatus Description	3
2.2 Progress Since Second Annual Report	7
Oscillatory Heat Transfer Measurements	7
Approximate Heat Transfer Analysis	19
Measurement of Oscillatory Flow	26
3.0 CONCLUSIONS	89
REFERENCES	91
Appendix A	
Appendix B	
Appendix C	

1.0 INTRODUCTION

Coupling between velocity oscillations and the combustion zone can be significant in determining the acoustic stability of solid propellant rocket motors (1-4). Observations of nonlinear wave behavior, pulsed instabilities in motors and laboratory burners, and shifts in mean pressures have been used to formulate qualitative heuristic models for this coupling (5-7). Attempts to quantify these models have been unsuccessful in the sense that scaling laboratory results to motor environments has produced conflicting results (8-10). Hence, the basic mechanisms have not been properly characterized by these models.

A review of studies on flow fields in chambers and acoustics in ducts suggests that these coupling phenomena include the effects of acoustic disturbances on turbulence in flows with high surface transpiration rates, acoustic streaming in the presence of combustion, and unsteady heterogeneous combustion processes. These processes involve fluid-dynamic and combustion-related phenomena which in themselves have not been studied qualitatively. In particular, the effect of substantial gas injection at lateral walls on acoustic streaming, on the acoustic boundary layer, on turbulence, on wall heat transfer, on heterogeneous combustion processes, and on their interactions have never been thoroughly examined. These processes, however, determine how acoustic waves interact with the propellant combustion processes and thereby influence the generation or absorption of acoustic energy in a solid propellant rocket motor. Studies of steady-state flows (11-13) have determined that wall blowing has a significant influence on the character of the flow-field. It is therefore reasonable to expect a similar influence under oscillatory conditions as well.

The objective of the experimental aspects of this program is to investigate oscillatory flow phenomena in a simulated rocket motor flowfield. Thus, meeting the technical objectives of this program provides basic knowledge and understanding of fundamental physical phenomena involved in the coupling between acoustic waves and combustion phenomena.

To investigate these phenomena, a cold flow apparatus was constructed to simulate the internal flow field in the combustor. Nitrogen flowing through large porous bronze tubes simulates the flow of gas from the propellant surface. The overall length and nozzle throat diameter can be adjusted to be investigated. A rotating valve at the nozzle exhaust plane provides a means of generating acoustic oscillations at a controlled frequency. Specific experimental studies described herein address the effect of acoustic disturbances on velocity profiles, turbulence, and surface heat flux. The motor length, surface Mach number, and amplitude and frequency of the acoustic oscillations are the primary variables. This report describes the technical progress made during the third year of technical effort.

2.0 EXPERIMENTAL STUDIES

The primary objective of the cold flow studies is to determine the effect of velocity oscillations on the oscillatory wall heat transfer and the acoustic wave behavior in a simulated rocket motor geometry. The results will provide direct experimental evidence for comparison with the velocity coupling models and a basis for the development of improved models.

2.1 APPARATUS DESCRIPTION

To conduct these experiments, the apparatus shown schematically in figure 1 has been fabricated. Nitrogen flowing through porous cylindrical bronze tubes simulates the combustion process at the propellant surface (this technique has been used successfully in previous studies at CSD on the effects of both steady-state (10,14) and oscillatory characteristics (15) on the internal ballistics). A flow distribution tube is used to equalize the flow to the 4-in. internal diameter porous tubing from the nitrogen supply system. Sonic flow is achieved either through this distribution tube or by orifices in the manifold to each section. Figures 2 and 3 show the construction of each section.

Each section is equipped with two ports for heat flux gages (as shown in figure 3) or for hot wire anemometers. Pressure taps are also located at these axial stations on the "grain" surface and one tap is located between the porous tubing and the flow distribution tubing. These taps lead to a Scanivalve/pressure transducer multiplexing system for recording the mean pressure distribution throughout the apparatus. The hot wire anemometers and the hot film flux gages are connected to TSI Model 1050 constant temperature anemometers. By operating them in the constant temperature mode, frequencies up to 50 kHz can be recorded faithfully.

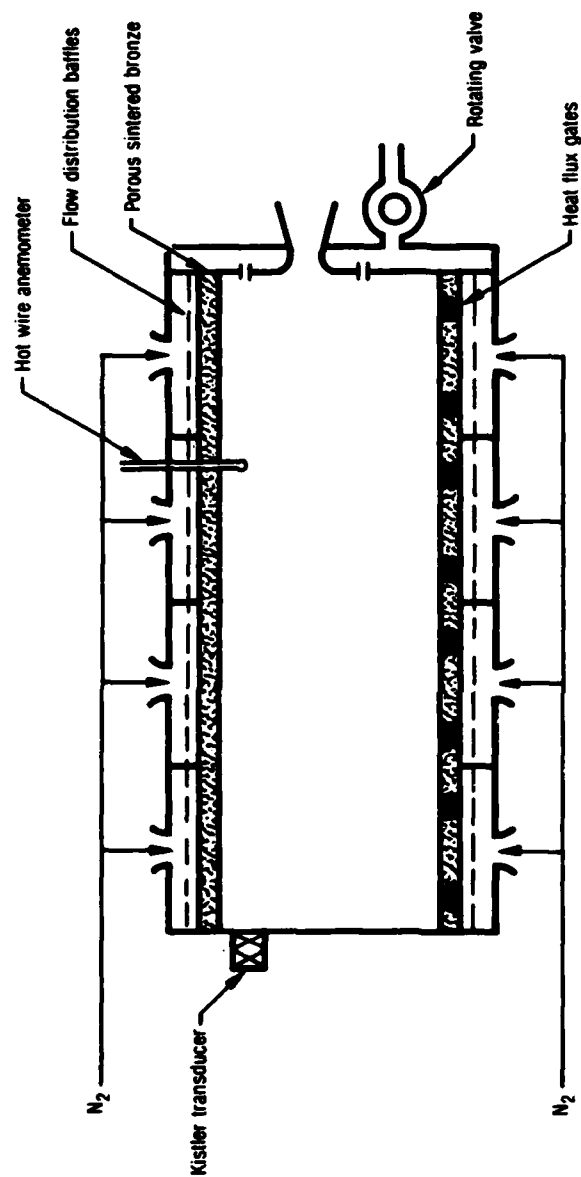


Figure 1. Cold Flow Velocity Coupling Apparatus

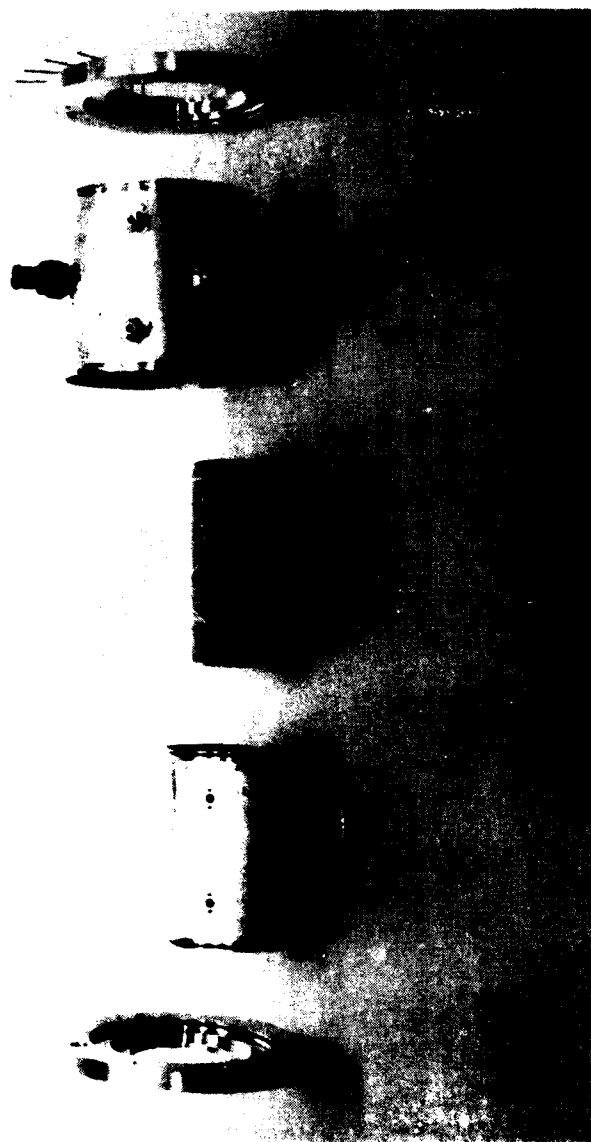


Figure 2. Exploded View of "Segment"

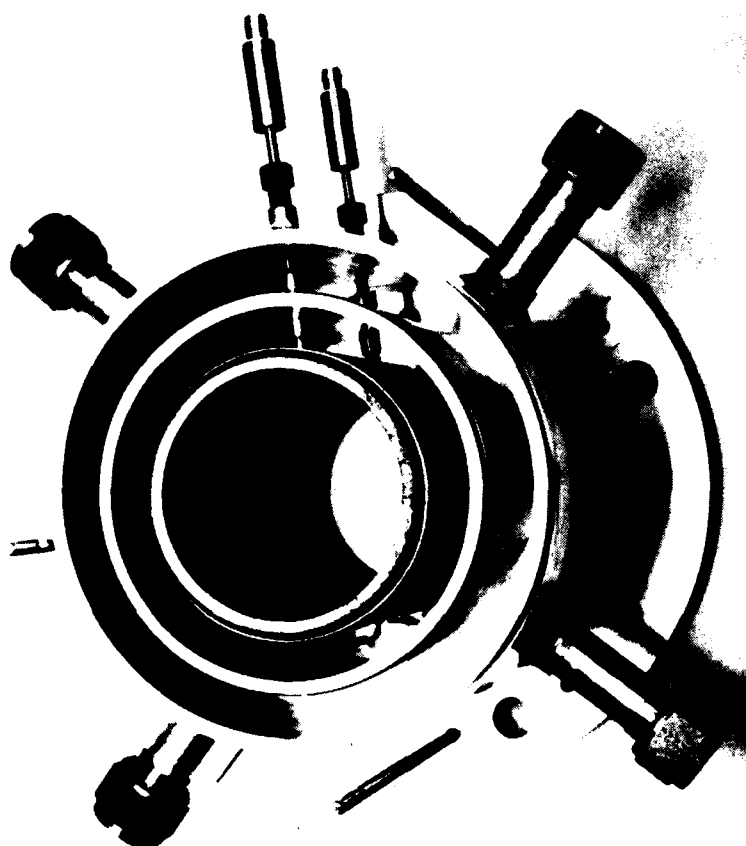


Figure 3. End View of "Segment"

The simulator is equipped with a rotating valve at the aft end to generate acoustic velocity oscillations. The frequency is controlled by varying the rotational speed of the electric motor driving the valve. To minimize the development of planar acoustic waves at the aft-end, the rotating valve is attached to an annular chamber which surrounds the steady-state nozzle. This annular chamber is open at the forward face to the main motor cavity. Figure 4 shows an exploded view of the aft-end hardware. The AN fitting leads to the rotating valve. The cavity for collecting the flow to the rotating valve is also equipped with a Kistler pressure transducer.

Considerable attention has been given to generating a realistic flow environment. By sectioning the apparatus, the length-to-diameter ratio can be varied from 2 and 23; however, the primary interest is between 9.5 and 23. This range encompasses the transition in velocity profile predicted by Beddini (11).

2.2 PROGRESS SINCE SECOND ANNUAL REPORT

The primary effort during the third year has been directed to two areas: first, extending the oscillatory heat transfer measurements to include more data in the flow transition region and to include the aft-end of the high L/D cavity; and second to measuring the oscillatory flow profiles across the port at several axial stations. The following sections describe the principal results obtained in each of these areas.

2.2.1 Oscillatory Heat Transfer Measurements

An additional series of tests was conducted to measure the oscillatory heat transfer coefficient to augment the data reported last year (16). By switching the head-end closure and the aft-end nozzle assembly, end for end data at six additional axial locations were obtained. As in the previously reported results (16), oscillations were driven at frequencies of approximately 85 Hz and 170 Hz, corresponding closely to the first two axial



Figure 4. Exploded View of Nozzle

modes predicted by classical acoustics*. Two rotating valves of different sizes were used to study the effect of acoustic pressure amplitude on the oscillatory heat flux. In these tests, the signals from all six heat flux gages, as well as the signals from the head end and two aft-end Kistler pressure transducers, were recorded on FM tape for later analysis. The signal from an optical tachometer on the drive shaft of the rotating valve was also recorded. This signal was used during playback of the data to provide a coherent trigger signal for the spectral analyzer.

Two forms of spectral analysis of these data were conducted because the flux oscillations include the response to the driven flow oscillations, as well as the response to any natural turbulence in the flow. First, the rms heat transfer coefficient was derived from the power spectra. This form reflects the response to both the driven and natural turbulence oscillations. Second, the rms heat transfer was derived from linear spectra by coherently averaging 50 ensembles of data using the reflecting tachometer as a trigger source. This "coherent" or "phase averaging" approach tends to remove the random fluctuations and thereby provides a better estimate of the heat transfer coefficient oscillations produced by the driven oscillations alone.

Figures 5 through 8 present the oscillatory heat transfer coefficient versus length for two test frequencies and amplitudes of area oscillation. The surface Mach number is approximately 0.001. Figures 9 through 12 show the corresponding results obtained for a surface Mach number

*Frequency sweeps were made to identify the frequencies of maximum acoustic response. No clearly defined peaks were observed which suggest high acoustic damping.

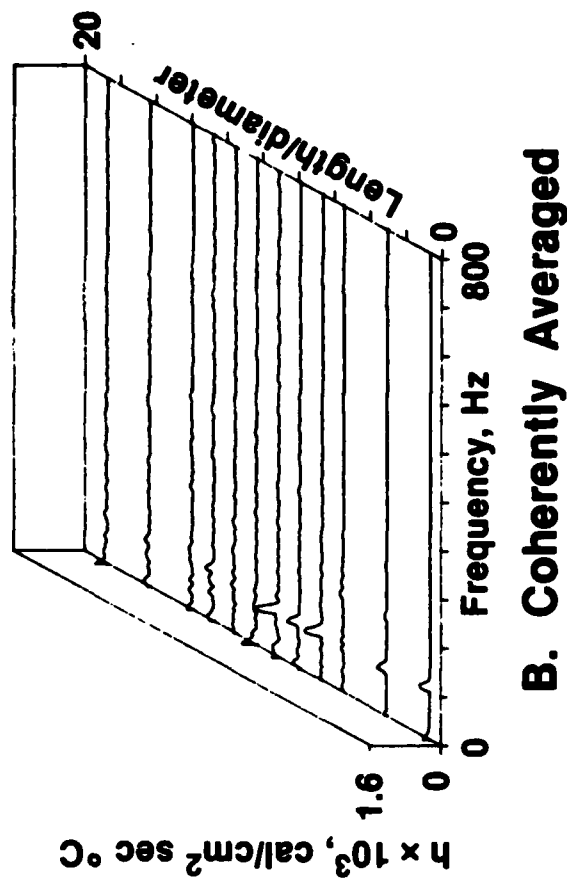
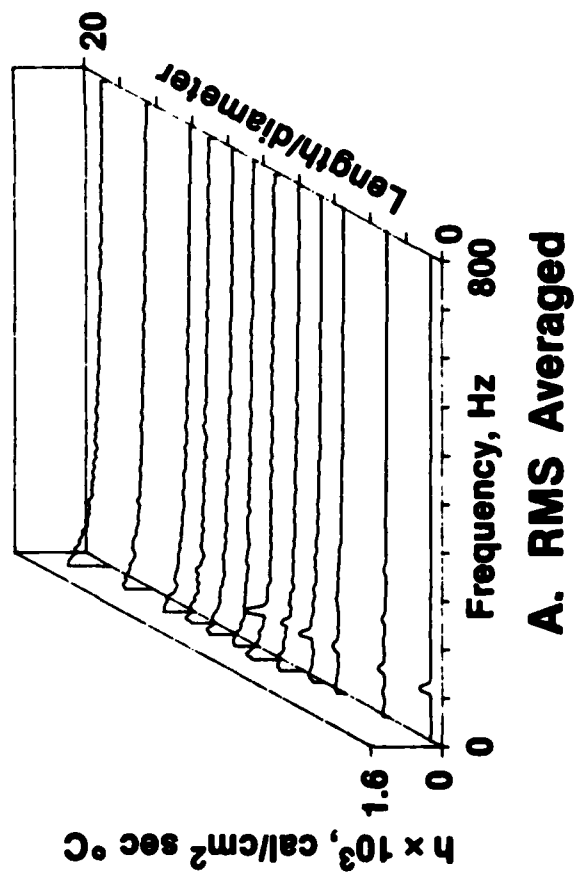
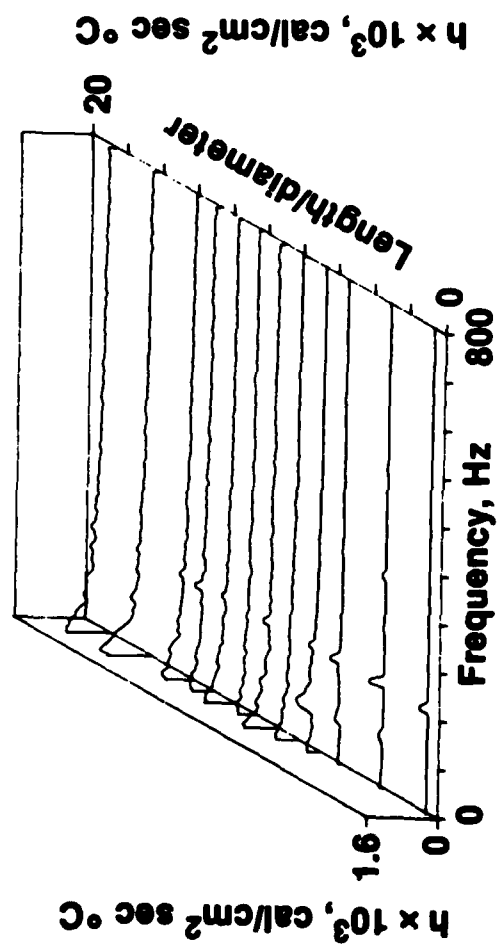
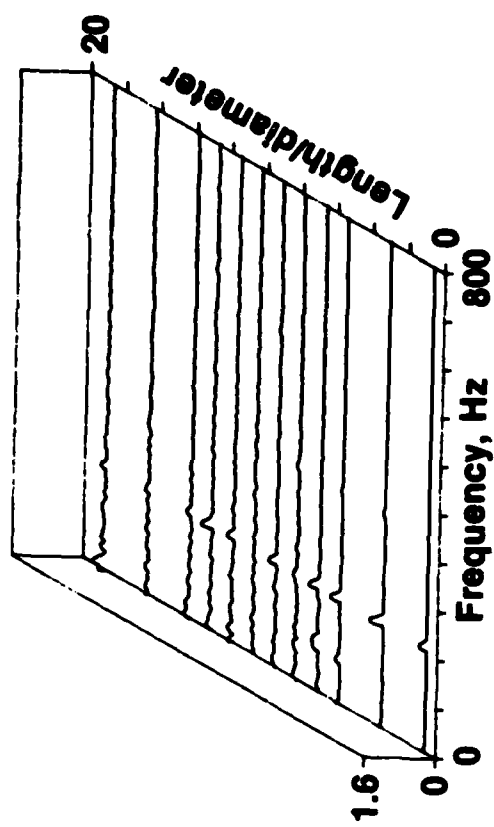


Figure 5. Oscillatory Heat Transfer Coefficient Spectra
 $(\epsilon_H = 0.061\%$, $A/\bar{A} = 1.1\%$, $f = 84$ Hz, $\bar{M}_3 = 0.0001)$

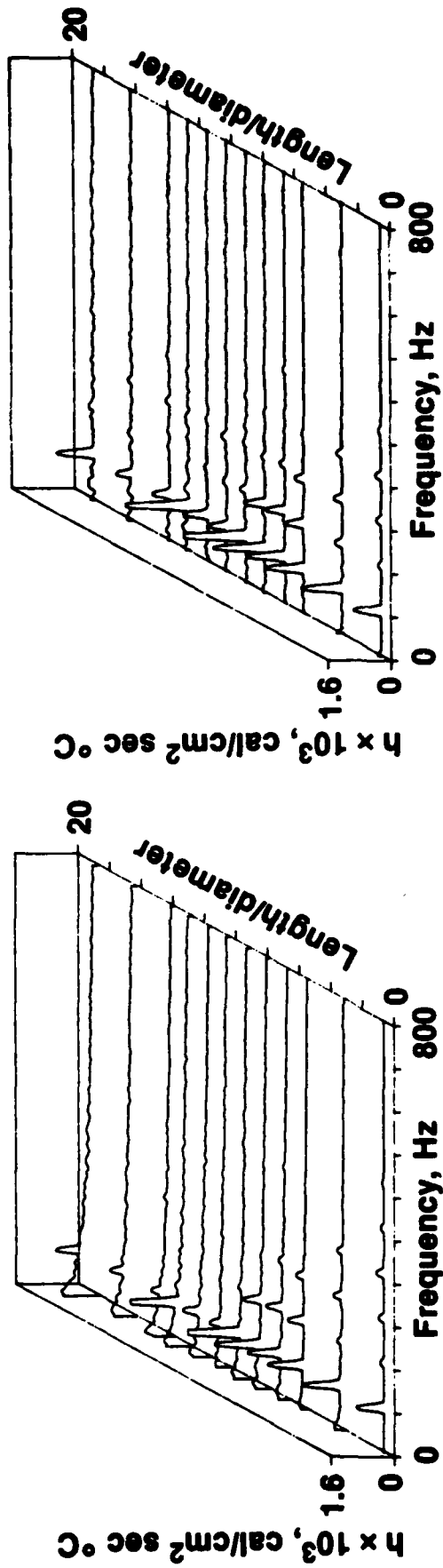


A. RMS Averaged



B. Coherently Averaged

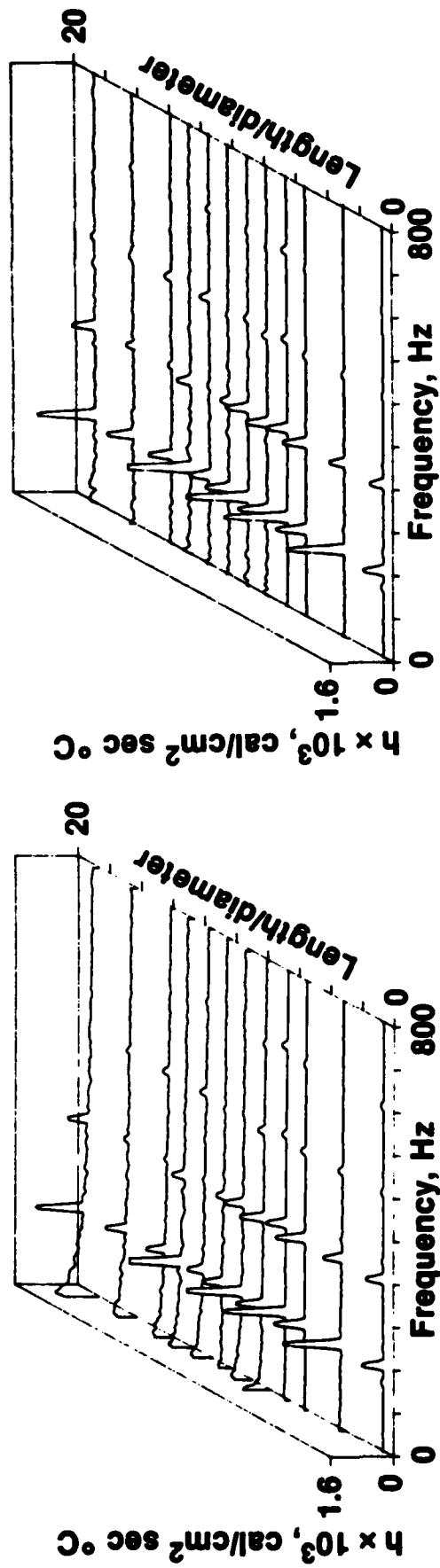
Figure 6. Oscillatory Heat Transfer Coefficient Spectra
 $(\epsilon_H = 0.048\%, \tilde{A}/K = 1.1\%, f = 176 \text{ Hz}, \bar{N}_3 = 0.00095)$



B. Coherently Averaged

A. RMS Averaged

Figure 7. Oscillatory Heat Transfer Coefficient Spectra
 $(\epsilon_H = 0.43\%, A/\bar{A} = 5.9\%, f = 85 \text{ Hz}, \bar{M}_3 = 0.00095)$

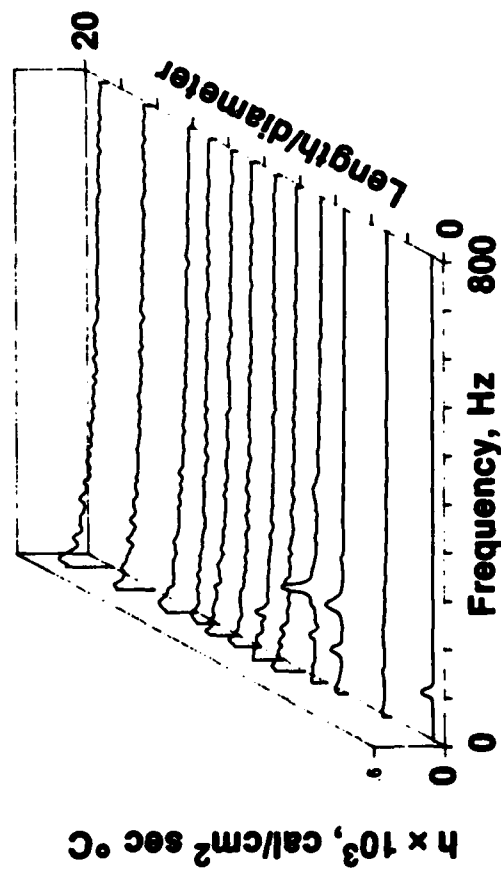


A. RMS Averaged

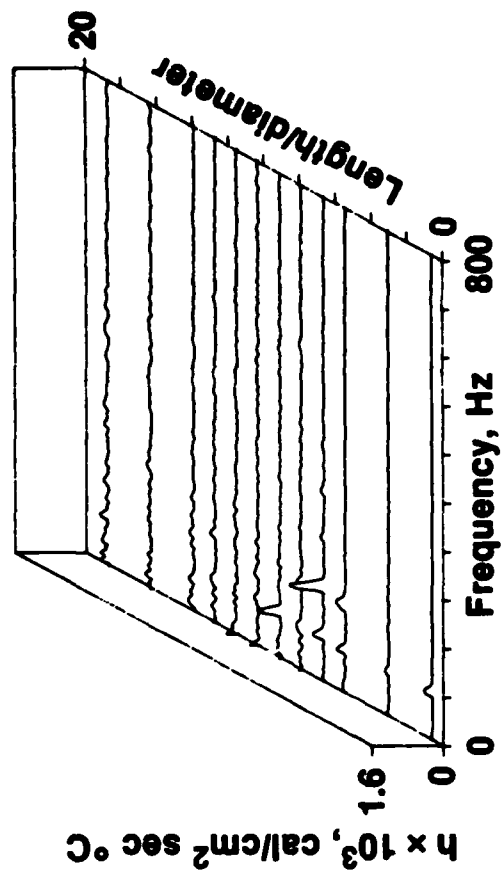
B. Coherently Averaged

Figure 8. Oscillatory Heat Transfer Coefficient Spectra

($\epsilon_H = 0.38\%$, $\tilde{A}/\bar{A} = 5.9\%$, $f = 165$ Hz, $\bar{M}_3 = 0.0001$)

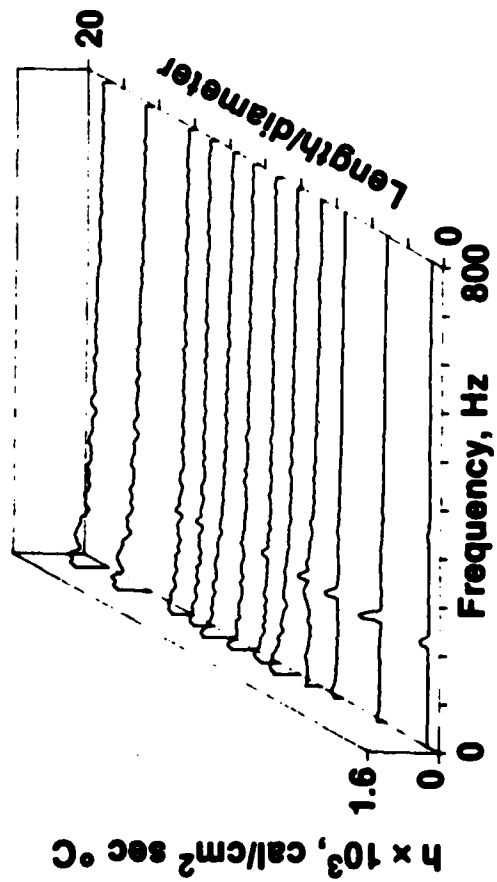


A. RMS Averaged

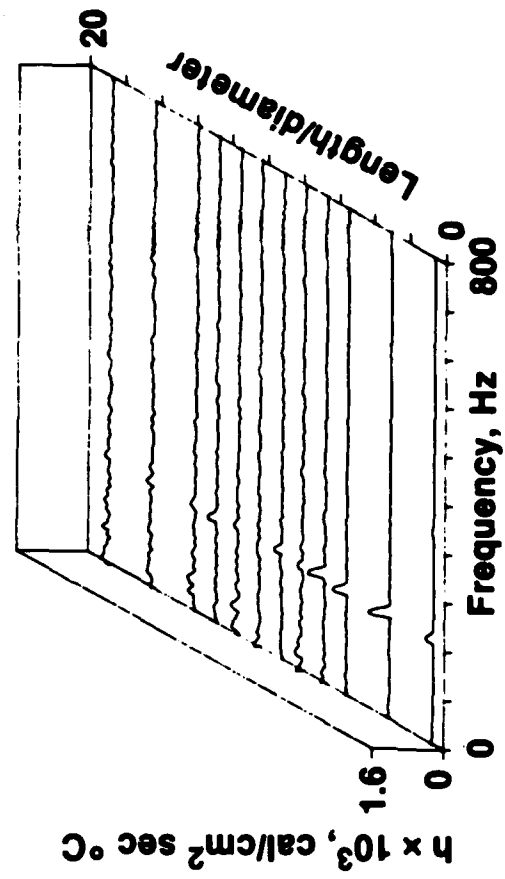


B. Coherently Averaged

Figure 9. Oscillatory Heat Transfer Coefficient Spectra
 $(\epsilon_H = 0.055\%, \bar{A}/\bar{A} = 0.6\%, f = 78 \text{ Hz}, \bar{M}_3 = 0.0017)$

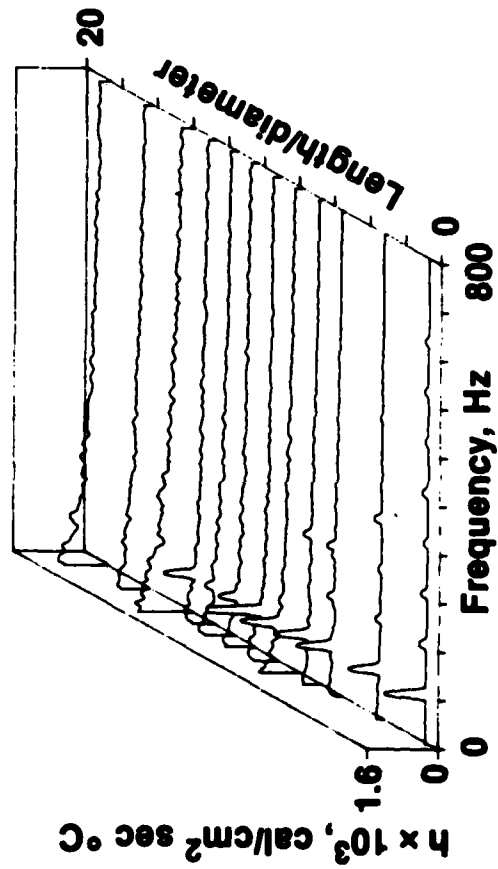


A. RMS Averaged

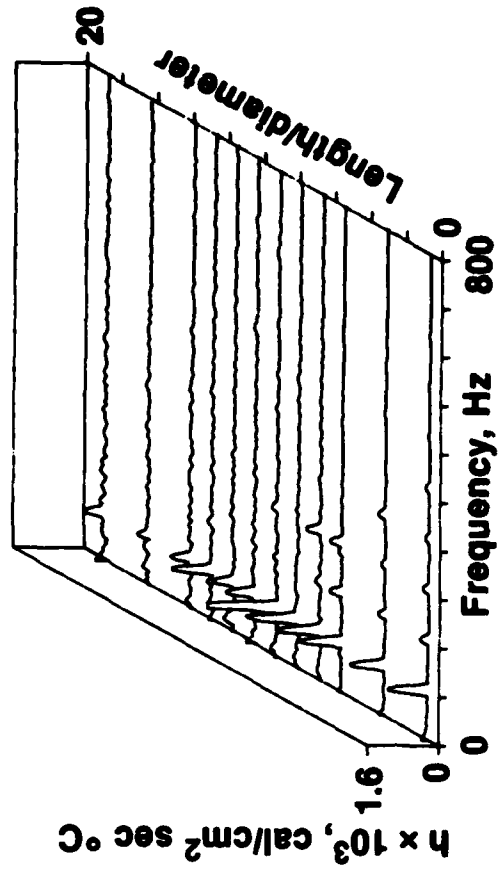


B. Coherently Averaged

Figure 10. Oscillatory Heat Transfer Coefficient Spectra
 $(\epsilon_H = 0.049\%, A/\bar{A} = 0.62\%, f = 175 \text{ Hz}, \bar{M}_3 = 0.0017)$

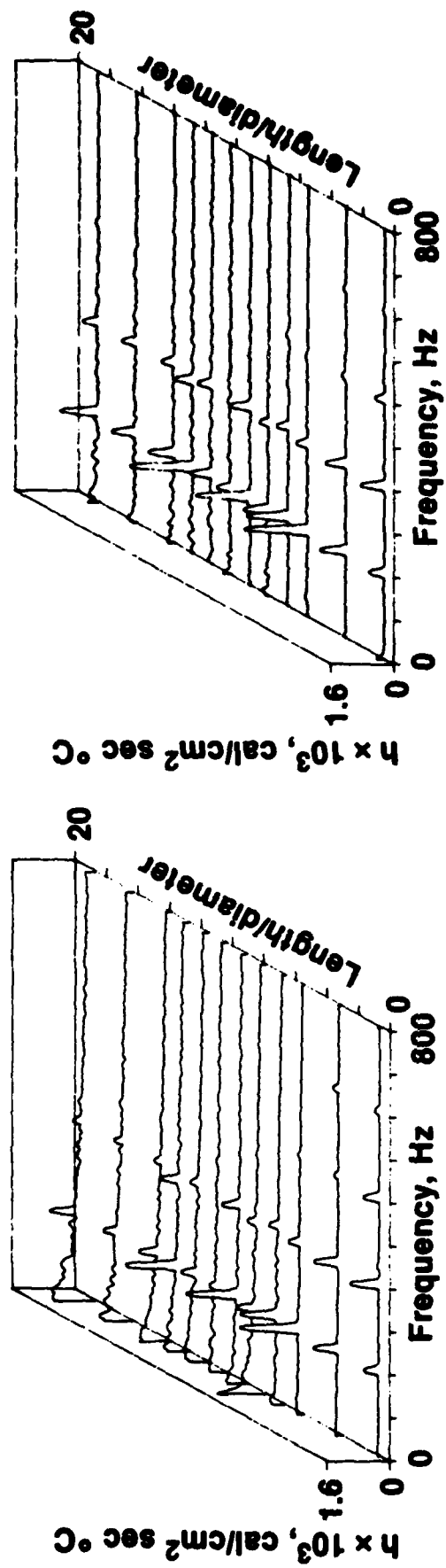


A. RMS Averaged



B. Coherently Averaged

Figure 11. Oscillatory Heat Transfer Coefficient Spectra
 $(\epsilon_H = 0.39\%, A/\bar{A} = 3.3\%, f = 85 \text{ Hz}, \bar{M}_3 = 0.0018)$



B. Coherently Averaged

A. RMS Averaged

Figure 12. Oscillatory Heat Transfer Coefficient Spectra
 $(\epsilon_H = 0.35\%, A/\bar{A} = 3.3\%, f = 170 \text{ Hz}, \bar{M}_3 = 0.0018)$

of 0.0018. Each figure presents two waterfalls showing the variation in spectral content as a function of axial location. The left hand figure waterfall shows the rms averaged spectra while the right hand figure waterfall shows the coherently averaged spectra.

A number of important observations can be made from these data. First, the rms averaged spectra all show a substantial increase in noncoherent fluctuations at axial locations greater than 7 diameters. This is particularly apparent when one examines the spectra at frequencies below 50 Hz. This behavior suggests that turbulence in the gas flow has penetrated to the wall. Interestingly, the axial pressure drop and velocity profile data also show the initial departure from the rotational inviscid flow model at about this same location (17). Thus, these data are consistent with the basic concept of the flow transition proposed by Beddini (9).

A second observation results from examining the axial variations in the spectra of the oscillatory heat transfer coefficients. In all cases, heat flux oscillations at the simulated propellant surface were generated from near the head-end of the simulated motor (i.e., $Z/D = 0.6$), to Z/D if approximately 6 to 8 even at acoustic pressures as low as 0.05%. Proceeding downstream, no coherent heat flux oscillations which accompany the lowest acoustic pressures were observed. This behavior is more apparent at the higher driving frequency than at the lower frequency. At the higher driver amplitudes (i.e., $\hat{A}/A > 3\%$), the driven oscillations in the heat flux are observed at all the axial locations.

A third observation is that significant harmonic content is generated at the higher frequencies and at the higher driving amplitudes, and consequently at the higher acoustic pressures. The harmonics first appear upstream of the transition and are most apparent near the head end of the motor. Interestingly, these nonlinear effects are also observed in the acoustic pressures.

These results are not consistent with either the linear or the nonlinear models for velocity coupling. According to the liner model, one would expect a sinusoidal variation in the amplitude of the heat transfer with axial position at the lower frequency (fundamental axial mode). At the higher frequency, one would expect the oscillatory heat transfer coefficient to vary as the full cycle of a rectified sine wave. Neither pattern is observed.

According to the nonlinear model, the surface heat transfer does not respond to flow oscillations until some threshold velocity is exceeded. Downstream at this threshold, the linear model would be expected to apply. Nonlinear behavior would be expected where the mean and oscillatory velocities are approximately equal the threshold velocity. Clearly the data show the heat transfer oscillations first appear at the head-end, while no response is observed at the aft-end. This behavior is also illustrated by the coherence between the oscillatory heat transfer and the head-end acoustic pressure. Figure 13 shows that at low driving amplitudes, high coherence is only found at the head-end. Furthermore, the region of high coherence spreads downstream towards the aft-end with increasing driving amplitude. Thus it is clear the observed behavior is contrary to the behavior expected from the models. This may explain why motor stability predictions have been misleading when high velocity coupling contributions are predicted.

2.2.2 Approximate Analysis of Oscillatory Heat Flux

A very simplified analysis of the oscillatory heat flux was conducted to provide some basic insights into the data. The primary intent was to determine if the oscillatory heat transfer is consistent with the behavior expected from convective transfer from one dimensional mean and oscillatory behavior.

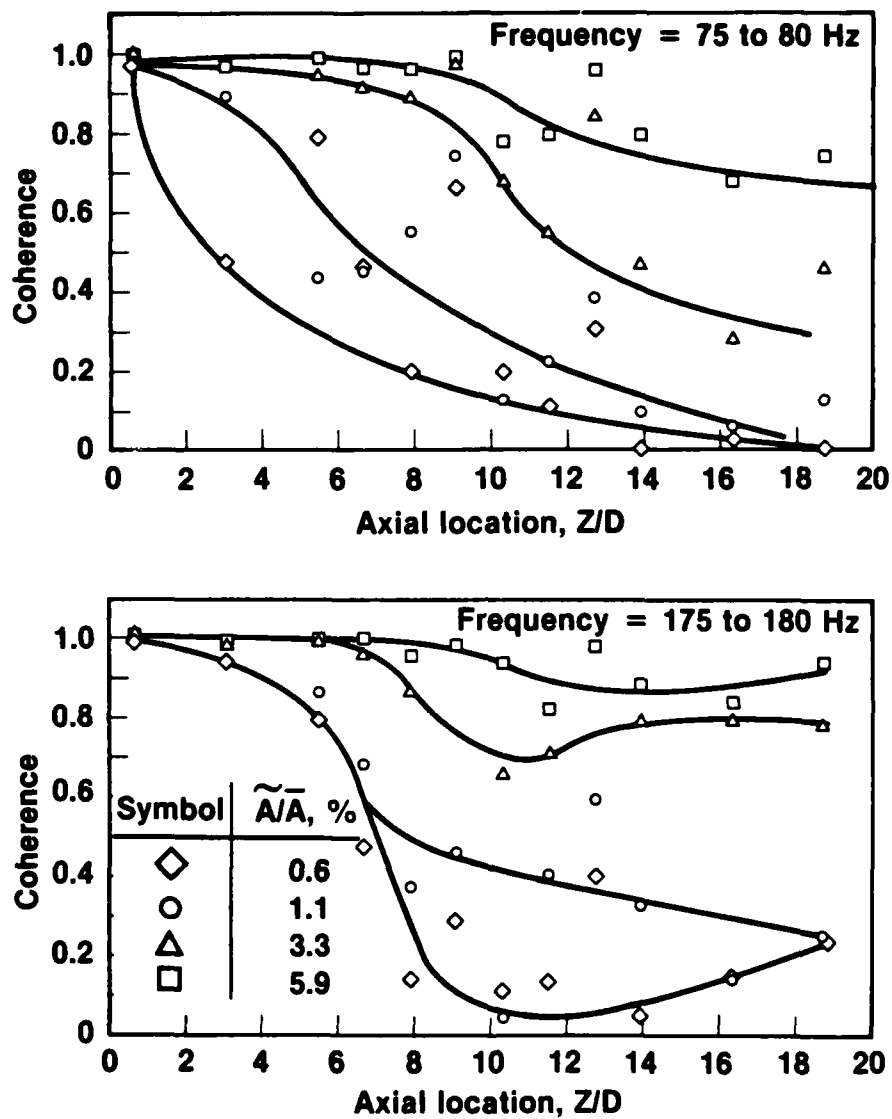


Figure 13. Coherence Between Heat Transfer and Head-End Acoustic Pressure

The basic assumption was that the oscillatory heat transfer coefficient is related to the oscillatory mass velocity.

$$\frac{\hat{h}}{\bar{h}} \propto \frac{\hat{p}}{\bar{p}} + \frac{\hat{u}}{\bar{u}} \quad (1)$$

For a cylindrical cavity with hard walls, the density and velocity oscillations were assumed to have the classical organ pipe axial distribution. Note that the mean velocity, \bar{U} , also appears in equation (1). Assuming a one-dimensional flow,

$$\bar{u}/\bar{a} = \frac{4L}{D} \bar{M}_b \quad (Z/L) \quad (2)$$

Combining the classical modal distributions of the acoustic pressure and velocity with equations (1) and (2) yields

$$\frac{\hat{h}}{\bar{h}} \propto \frac{\hat{p}}{\bar{p}} \left[\cos(\pi Z/L) - \frac{1 \sin(\pi Z/L)}{\bar{M}_b (4L/D) (Z/L)} \right] \quad (3)$$

Parametric studies of equation (3) show the maximum oscillatory heat flux occurs at the head end of the motor, which agrees with the data.

Next, pulse tests suggested that the porous tubing simulating the propellant surface provides large acoustic damping. Furthermore, previous in-house studies showed the admittance could be explained from measurements of the steady-state pressure drop across the porous tubing. The details associated with these statements will be covered in Appendix A. This large damping could influence the axial distribution of the acoustic pressure and velocity.

To estimate the effect of this admittance on the oscillatory heat transfer coefficient, the Kummer's function solutions of the one dimensional acoustics were used to predict the acoustic pressure and velocity (18). These predicted acoustic parameters were combined with equations (1) and (2) to estimate the phase angle between the heat transfer and the head-end acoustic pressure. These predicted phase angles are compared with measured values in Figure 14.

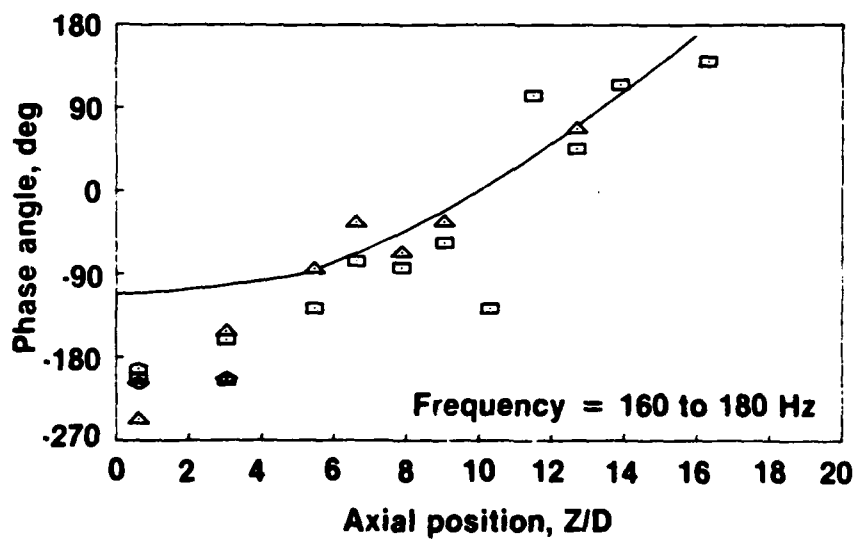
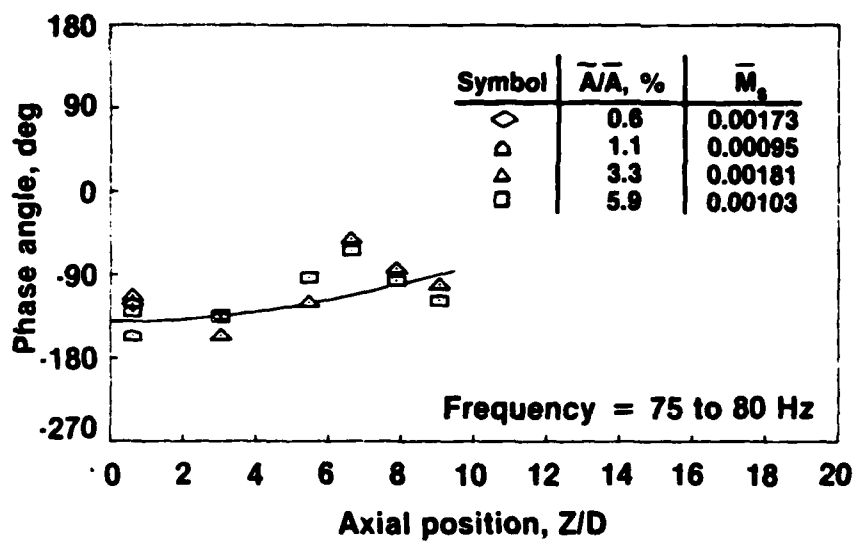


Figure 14. Phase Angle Between Heat Transfer
and Head-End Acoustic Pressure

Note that at 78 to 84 Hz, the observed phase angles follow the predicted angles with reasonable accuracy. At the higher frequency however, substantial deviations occur, particularly near the head-end of the motor. This is consistent with Flandro's prediction (19) and Ben Reuven's prediction (20) that Stokes layer effects will be more significant at higher frequencies.

In addition to comparing the predicted and observed phase angles, one would like to compare predicted and observed amplitudes. To do this however, requires the measurement of the mean heat transfer coefficient so the data can be normalized properly. The steady-state performance of the flux gages presented in reference 16 showed that heat losses from these gages to the apparatus constitute a large correction which is needed. A method for measuring these losses was developed when the gages are used in the wall of a plastic pipe. In the cold flow simulator, however, the plastic wall is replaced by the porous bronze. Furthermore, the nitrogen flows through this wall and thereby the gage heat losses may depend on the gas flow. Thus, the methods reported previously (16) cannot be used.

The special apparatus shown in Figure 15 was then adapted from an earlier design (21) to minimize the effects of gas flow across the end face of the gage. Total energy losses from each of the gages over then measured using the two Mach numbers of interest (i.e., 0.001 and 0.0018) over a range of gas pressures. These losses were determined using the equation

$$\text{Loss} = \frac{E^2 R_g}{(R_g + 41)^2} \cdot \frac{1}{(T_g - T_\infty)} \quad (4)$$

where E is the time average voltage, R_g is the gage resistance, T_g is the gage temperature and T is the gas temperature. Figure 16 shows these losses to be essentially independent of the gas mass flow parameter Pd_t^2 . This suggests that the temperature of the porous bronze and the nitrogen are nearly equal to

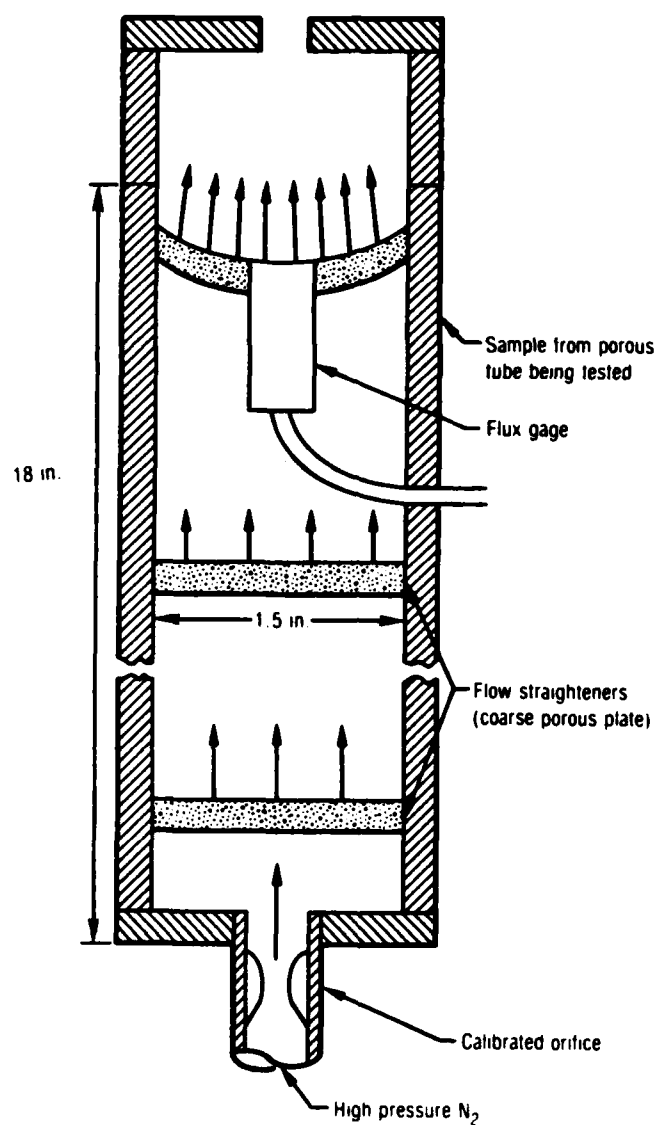


Figure 15. Apparatus to Calibrate Heat Loss

HEAT LOSS CALIBRATION

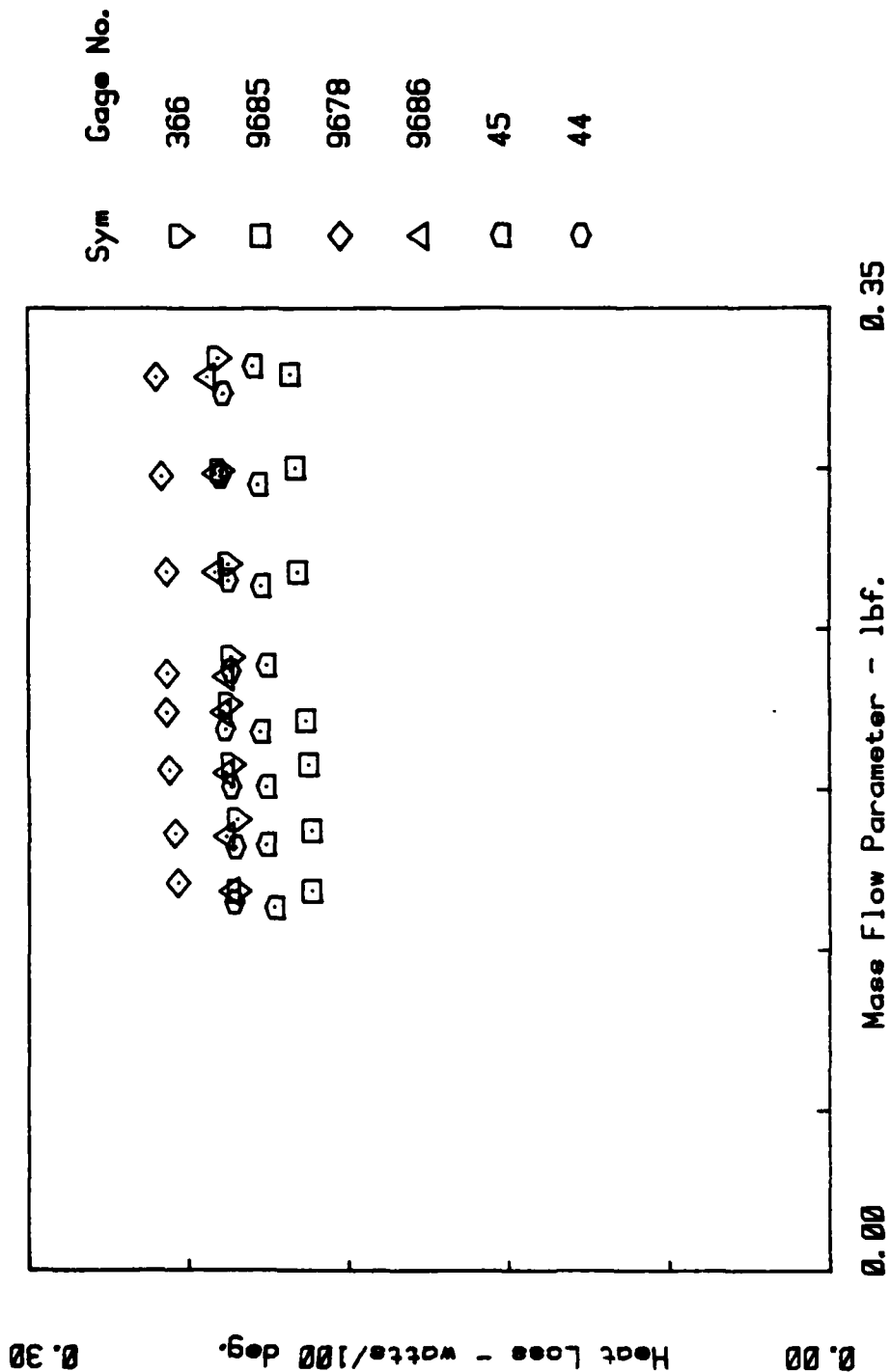


Figure 16.

that conductive from the gage to the bronze is the dominate mechanism. This result might have been expected since the surface area for conduction is much smaller than the area for transferring energy between the porous bronze and the nitrogen.

2.2.3 Measurement of the Oscillatory Flow Environment

The oscillatory heat transfer measurements suggest that information on the oscillatory flow field is needed to interpret the observed behavior. Hence, significant effort was directed to measuring the oscillatory flow field. Specifically, single-element hot-wire anemometer measurements were made at five axial stations; $Z/D = 1.8, 4.22, 6.64, 11.5$ and 17.6 . The first station is characteristic of the flow field prior to transition. The second two stations were chosen to examine the behavior in the flow transition region while the last two allow measurements in the transitioned flow.

Three sets of conditions were tested. The first two sets duplicate the surface Mach number, frequency, and damping conditions used in oscillatory heat transfer tests. Thus, the flow field and heat transfer measurements can be compared directly over a range of conditions. The third series of tests were conducted with a reduced acoustic admittance of the simulated propellant surface. Several years ago, CSD conducted a small analytical and experimental study to measure the response of these porous bronze tubes. The results of this study, which are reported in Appendix A, show the response of the surface is

$$R = \frac{-2i\lambda}{(2-n)} \left\{ \left(\frac{2}{2-n} \right) \left(\frac{\bar{P}_A}{\bar{P}_W} \right)^2 + i\lambda \left[\left(\frac{\bar{P}_A}{\bar{P}_W} \right)^2 - 1 \right] \right\}^{-1} \quad (5)$$

Thus the real part is negative and provides acoustic damping. This damping increases with increasing frequency. Under the baseline conditions, the real part varies between -5 and -8.

To alter the damping, equation (5) shows that the magnitude of the response can be decreased by decreasing the volume in the annular cavity between the flow distribution tubes and the porous bronze tubing. Therefore, 3/16 inch polypropylene casting beads were used to fill approximately 65% of this volume. This reduces the real part of the response to approximately -1. The flow field measurements were then repeated using a surface Mach number of 0.0018.

Initial tests were made to determine the frequencies at which peaks in acoustic pressure amplitude occur. The rotational speed of the rotary valve was varied and peaks were noted at 65 hz and 135 hz. The magnitude of the oscillatory pressure increased by a factor of two, as shown in Table I. This decrease in resonant frequency from the classical organ pipe mode is at first surprising. However, examining equation (5) shows the imaginary part of the response is also negative, which depresses the resonant frequency.

At each set of conditions, the oscillatory flowfield was analyzed from two points of view. The first viewpoint approaches the flowfield on the basis of the turbulence properties; here the spectra of turbulence intensity (velocity oscillations normalized to the local mean speed) is the primary property of interest. The second viewpoint looks at the flowfield on the basis of acoustics; here the amplitude phase and coherence of the normalized acoustic particle velocity (with respect to the normalized head-end acoustic pressure) are the properties of primary interest.

Figure 17 through 20 show the radial profiles of the turbulence intensity spectra for two frequencies at $Z/D = 1.8$ and $Ms = 0.001$. A log scale was

Table I. Summary of Acoustic Pressures

$M_S \times 10^3$	$\tilde{A}/\bar{A}, \%$	Frequency, Hz	Damping	Acoustic Pressure (P_{rms}/\bar{P}), %	
				Head-End	Aft-End
0.93	1.1	85	Baseline	0.061	0.078
		170		0.048	0.087
1.03	5.9	85		0.43	0.55
		170		0.38	0.73
1.73	0.6	76	Baseline	0.055	0.075
		170		0.049	0.092
1.81	3.3	85		0.39	0.57
		170		0.35	0.73
1.73	0.6	65	Reduced Damping	0.134	0.157
		135		0.089	0.124
1.81	0.6	65		0.84	1.02
		135		0.60	0.89

TURBULENCE INTENSITY PROFILE

Z/D = 1.80 Freq = 84.00 Hz. $\Lambda/\Lambda_t = 1.10 \times$ $Max10f3 = 1.00$

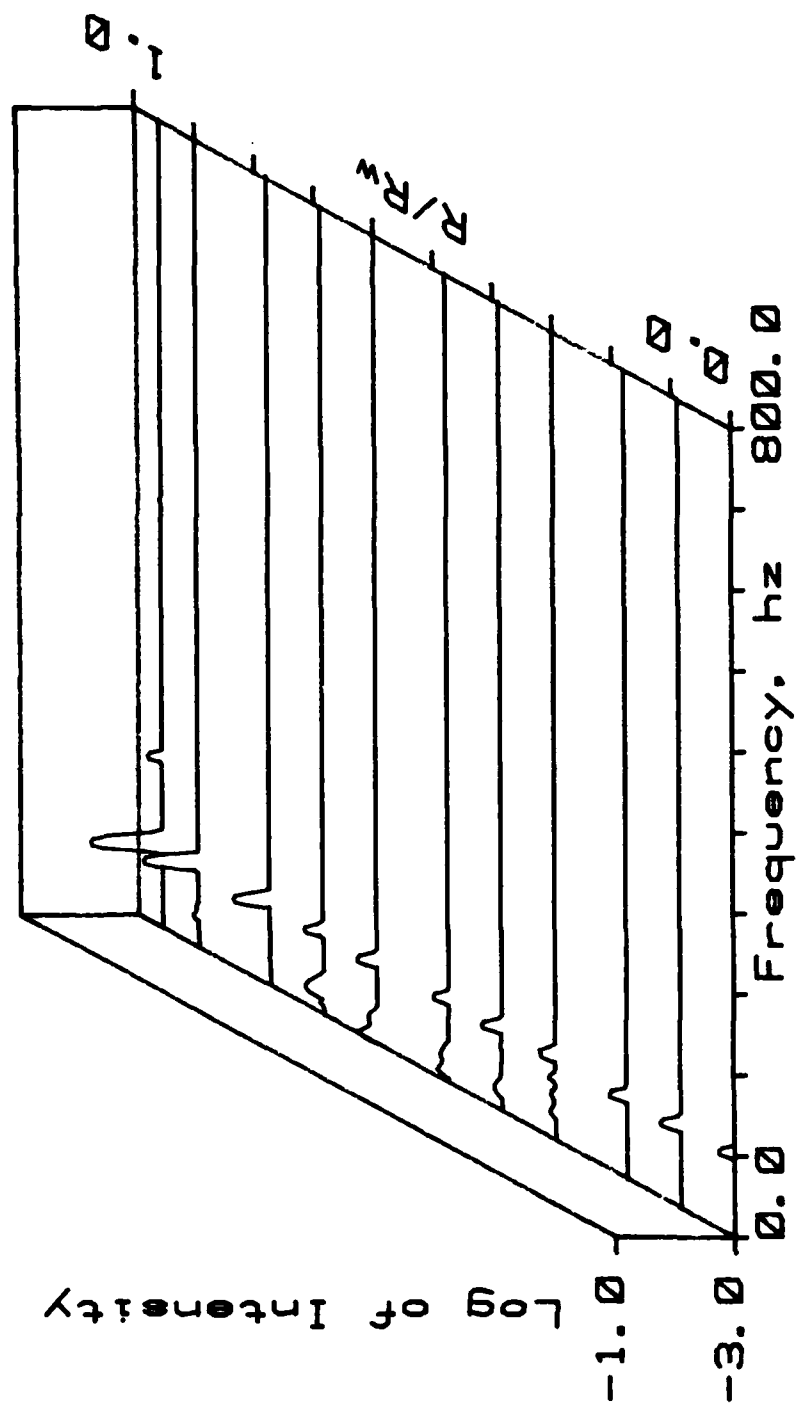


Figure 17.

TURBULENCE INTENSITY PROFILE

Z/D = 1.80 Freq = 170.00 Hz. $\Delta/\Delta t = 1.10 \times$ $\text{Max}10\text{f3} = 1.00$

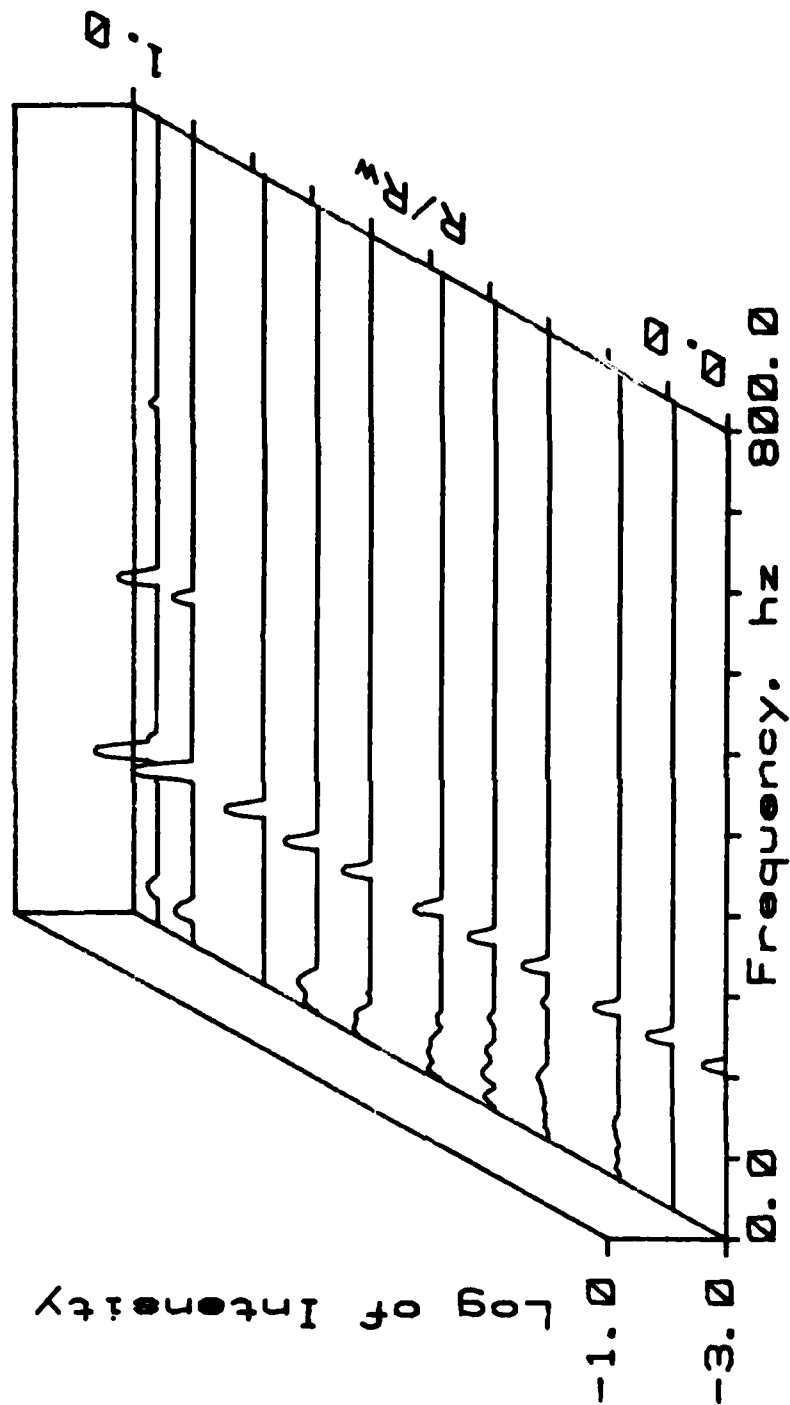


Figure 18.

TURBULENCE INTENSITY PROFILE

Z/D = 1.80 Freq = 84.00 Hz. $\Delta/\Delta t = 5.60 \times 10^{-3}$ Max10f3 = 1.00

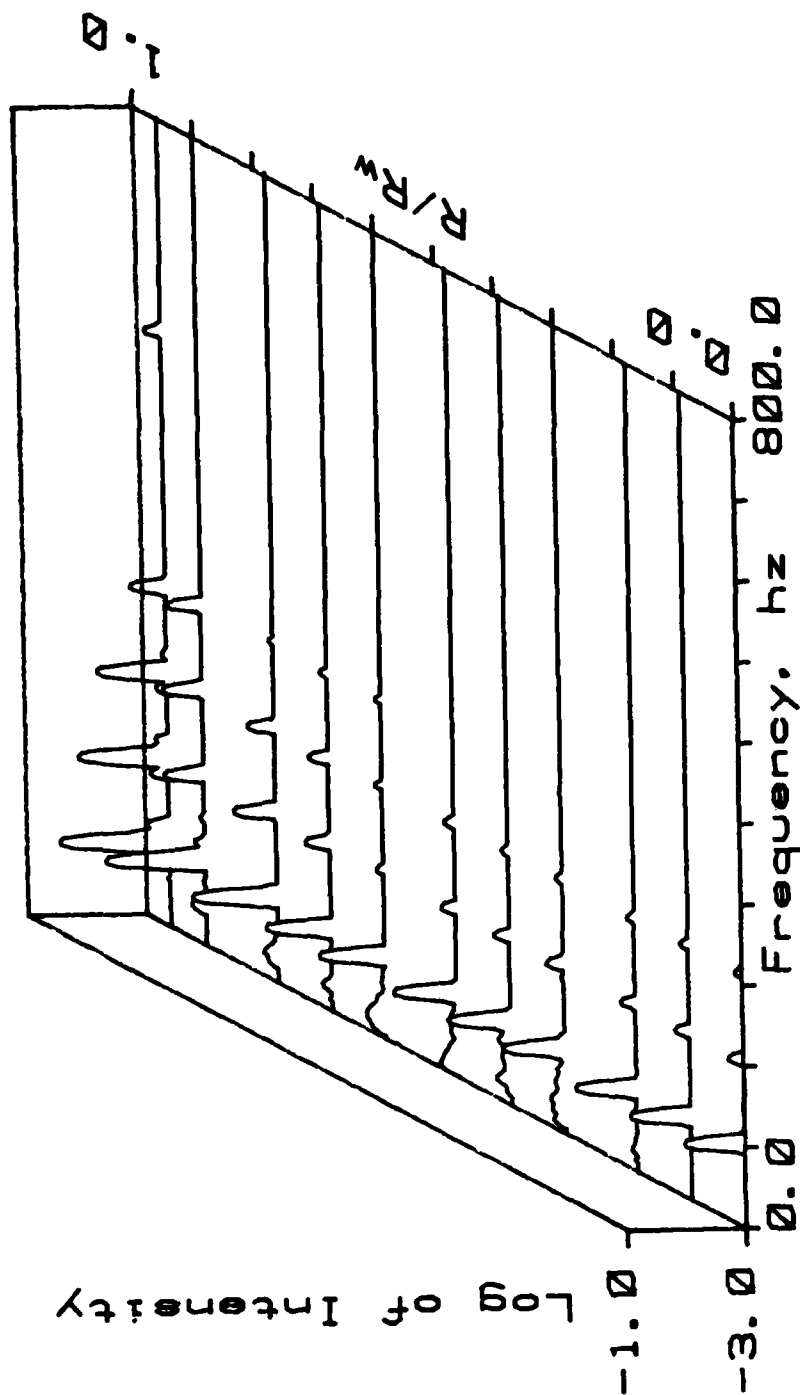


Figure 19.

TURBULENCE INTENSITY PROFILE

Z/D = 1.00 Freq = 170.00 Hz. A/A_t = 5.00 x Max10f3 = 1.00

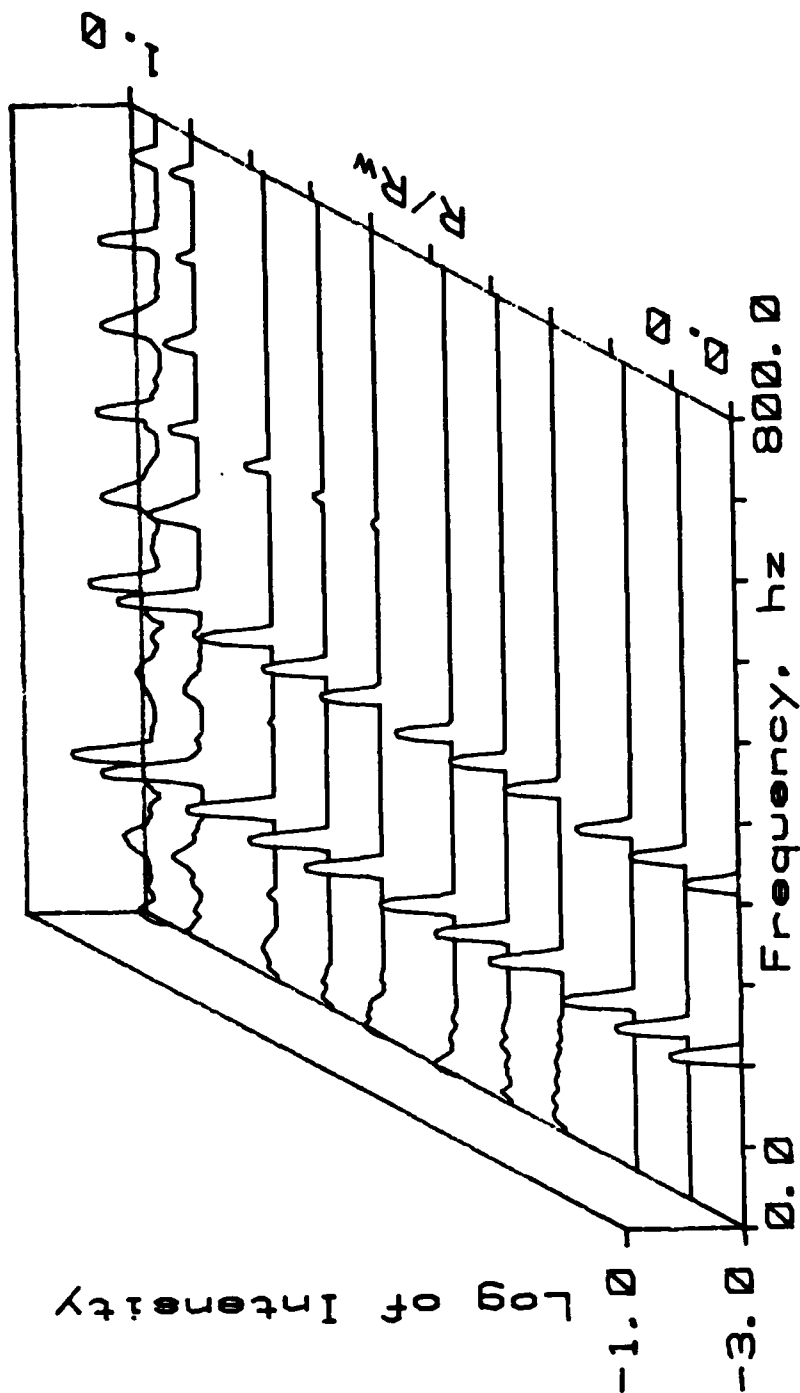


Figure 20.

chosen so both the low intensity near the centerline, as well as the higher intensities near the wall, could be displayed conveniently in the same waterfall. Figure 21 shows the turbulence intensity spectra without any acoustic driving. Several observations can be made. First, the acoustic oscillation appear to reduce the low level background turbulence to even lower levels. Second, the intensity of the driven oscillations increases significantly near the wall. This could result from a combination of an increased acoustic particle velocity and/or the decreased mean flow velocity near the wall. This point leads to an interest in analyzing the data from the acoustics viewpoint. Third, nonlinear behavior (as indicated by the harmonic content) first appears in the near wall region. This nonlinear behavior increases with both increasing frequency and increasing driving amplitude, which is consistent with the oscillatory heat transfer observations.

Figures 22 through 25 show the radial profile of these same data from the acoustics viewpoint, that is the coherence, amplitude, and phase of the acoustic particle velocity relative to the head-end acoustic pressure at the driving frequency. These plots all show the amplitude and phase to be essentially constant in the center cone flow. Near the wall, however, there are significant changes in both amplitude and phase. This behavior is qualitatively consistent with the acoustic/wall interactions predicted by Flandro (19) and suggested by Ben Reuven (20). Quantitative comparisons between these two models and these data are planned during the next year.

Figure 26 shows the corresponding radial profile in the mean speed. Note that the single element hot-wire anemometer was oriented to measure the total velocity in the r - z plane. Also shown on figure 26 are the total velocity profiles predicted by the Berman, Taylor, Culick (BTC) models and $1/7$ power

TURBULENCE INTENSITY PROFILE

$Z/D = 1.00$ $\text{Freq} = 0.00 \text{ Hz.}$ $\Delta/\Delta t = 0.00 \times$ $M \times 10^{13} = 0.96$

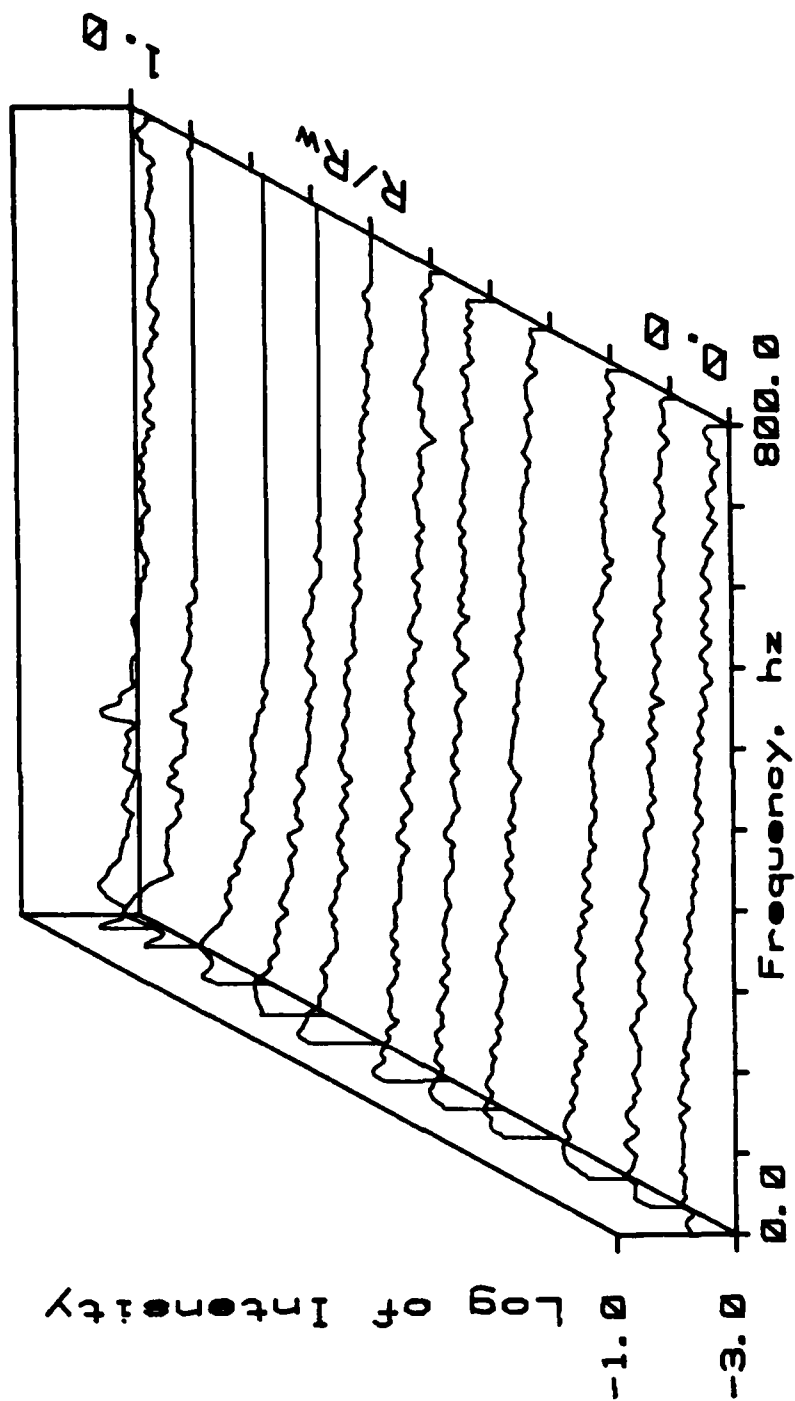


Figure 21.

NORMALIZED ACOUSTIC VELOCITY PROFILE

$Z/D = 1.88$ Freq = 84.88 A/Ac = 1.18 \times Max1013 = 1.88

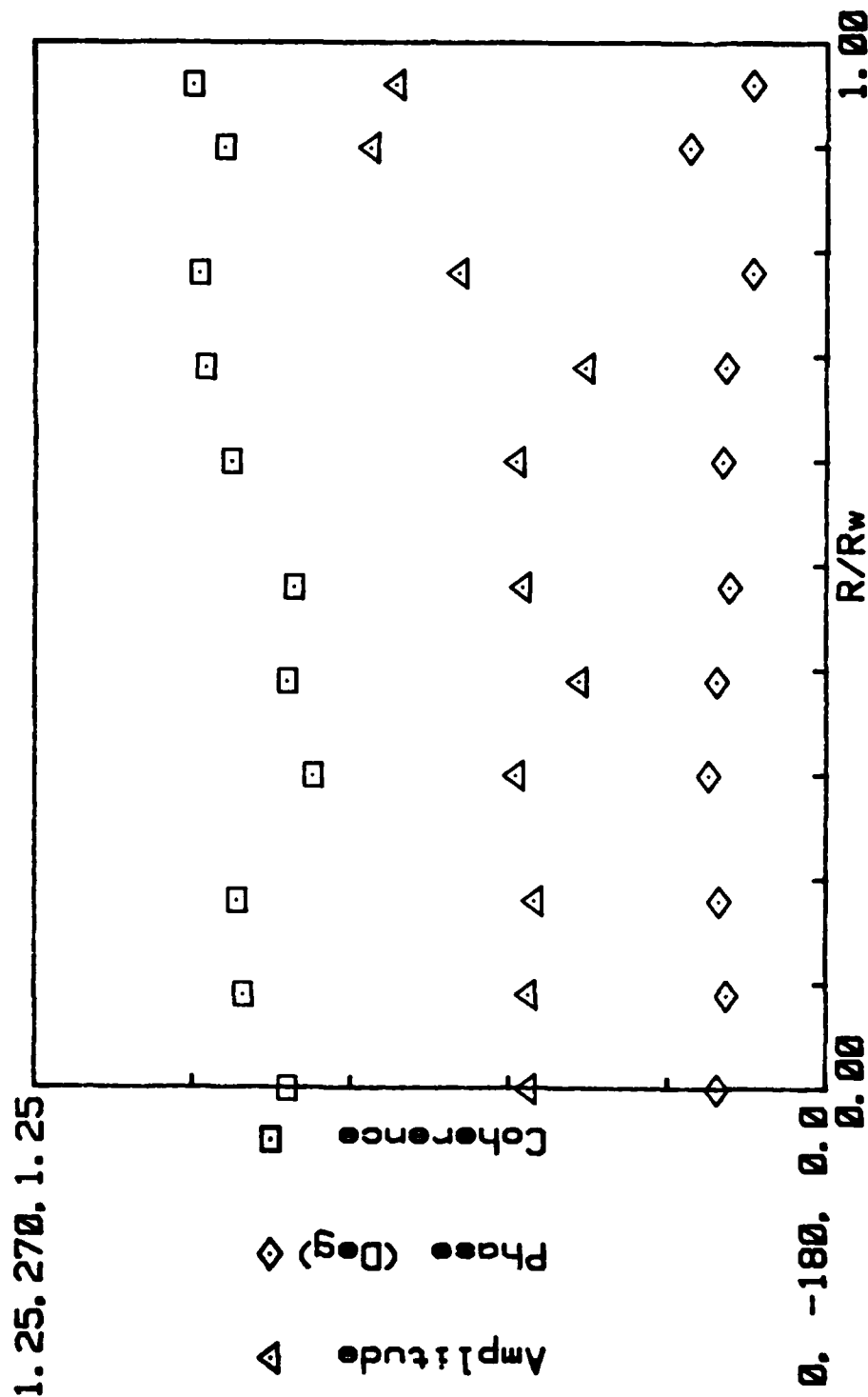


Figure 22.

NORMALIZED ACOUSTIC VELOCITY PROFILE

Z/D = 1.88 Freq = 178.88 A/Ac = 1.18 X Max18f3 = 1.08

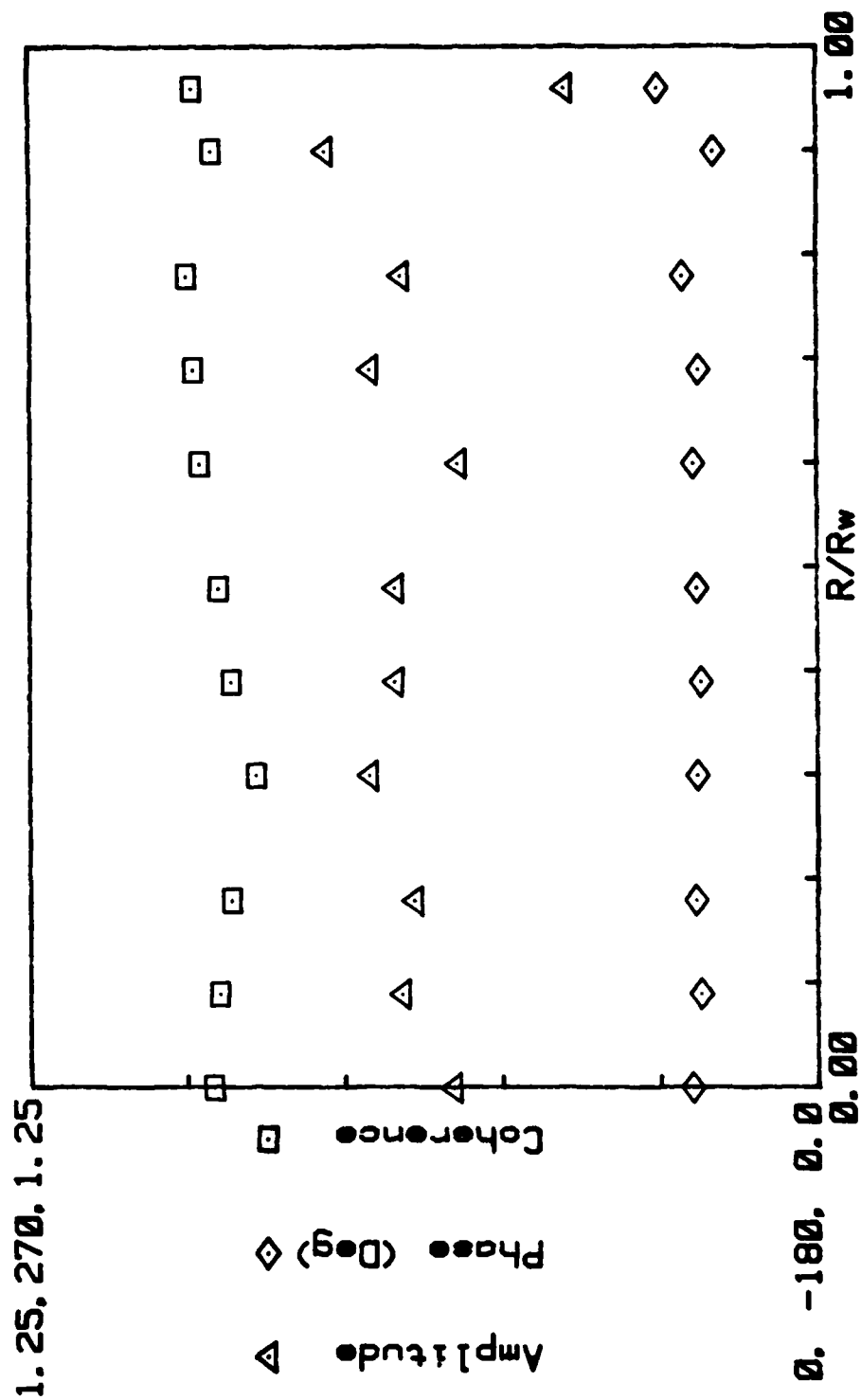


Figure 23.

NORMALIZED ACOUSTIC VELOCITY PROFILE

$Z/D = 1.00$ Freq = 84.00 A/Ac = 5.00 X Max1013 = 1.00

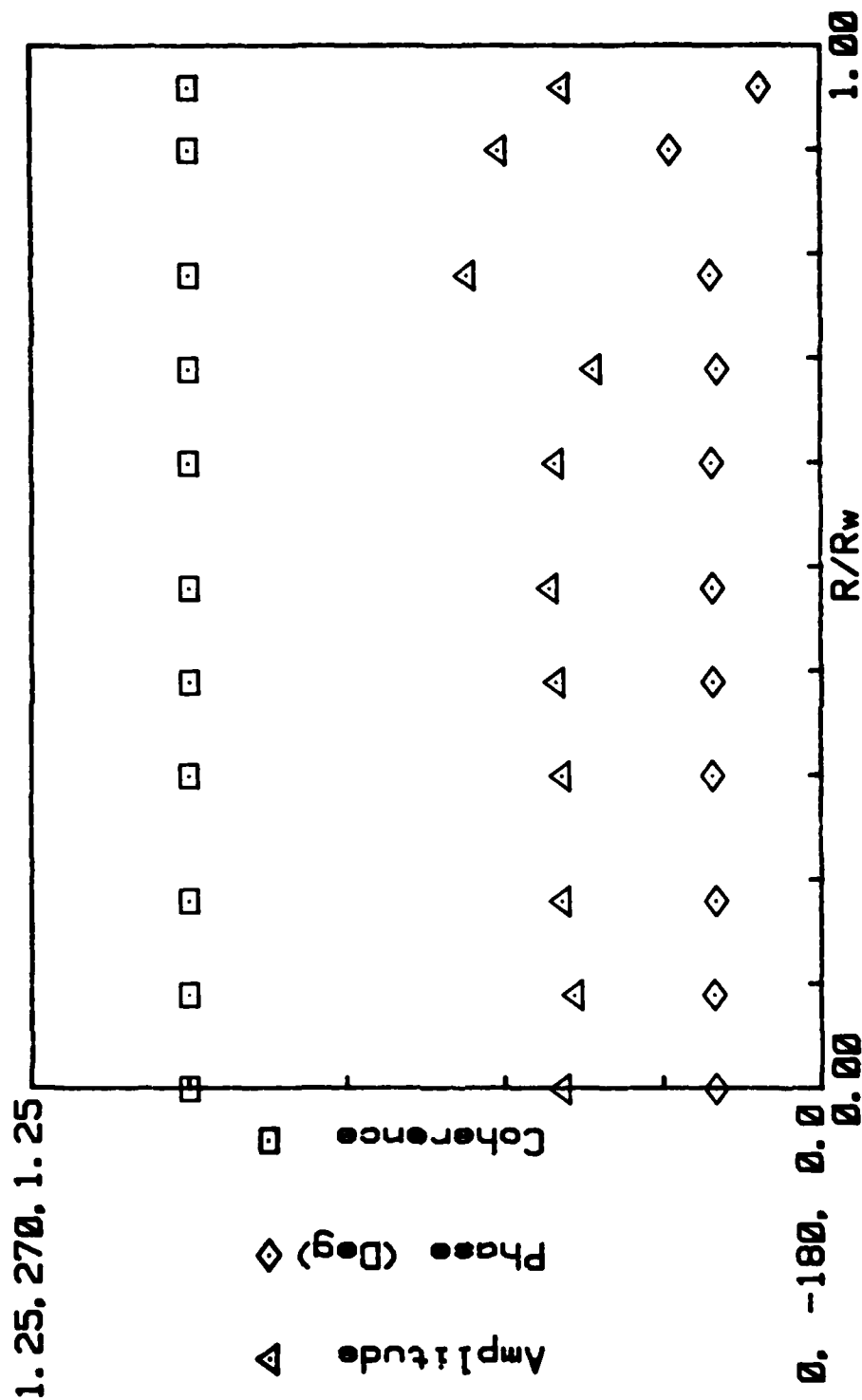


Figure 24.

NORMALIZED ACOUSTIC VELOCITY PROFILE

Z/D = 1.00 Freq = 170.00 A/Ac = 5.68 X Mex18f3 = 1.00

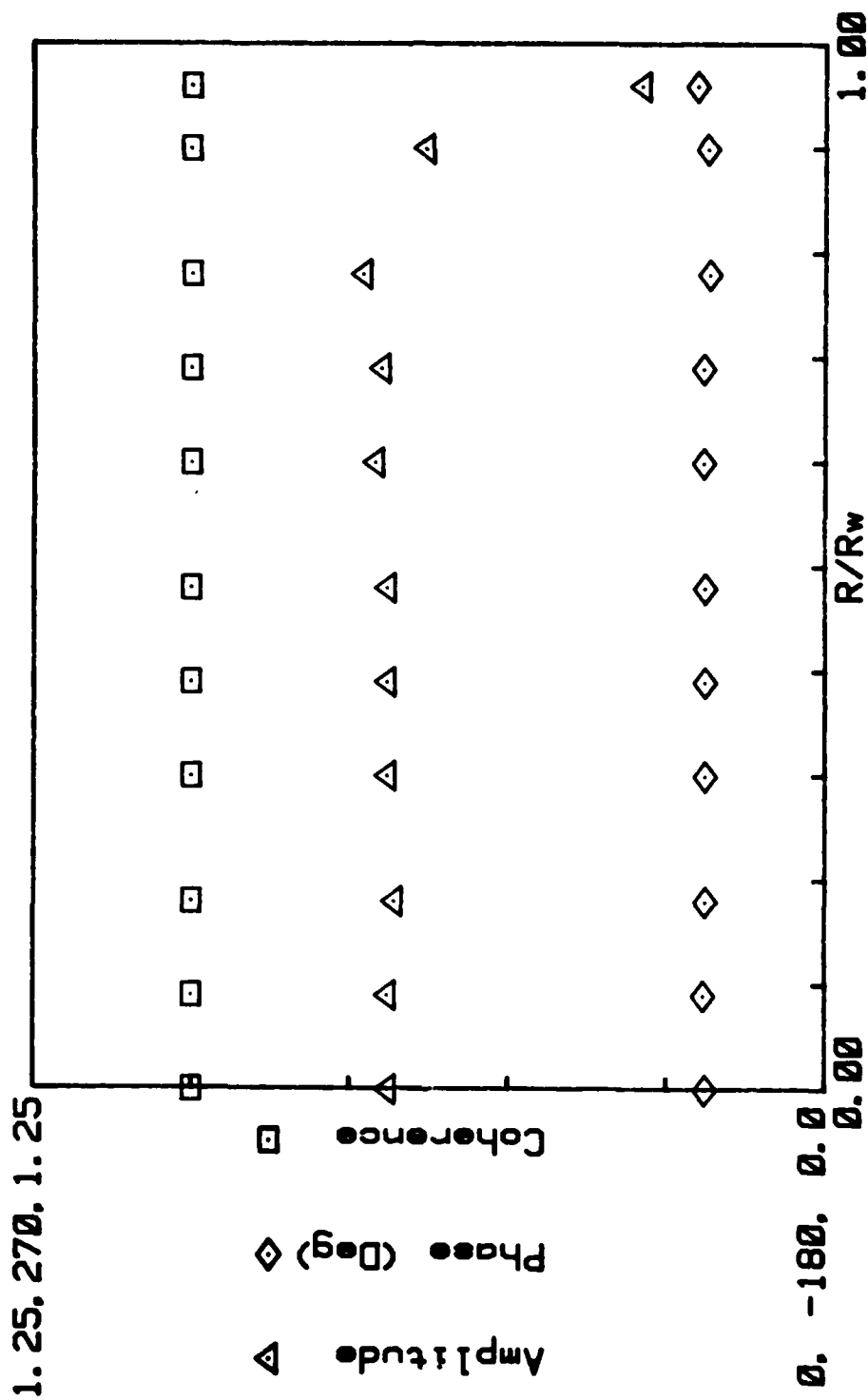


Figure 25.

MEAN VELOCITY PROFILE

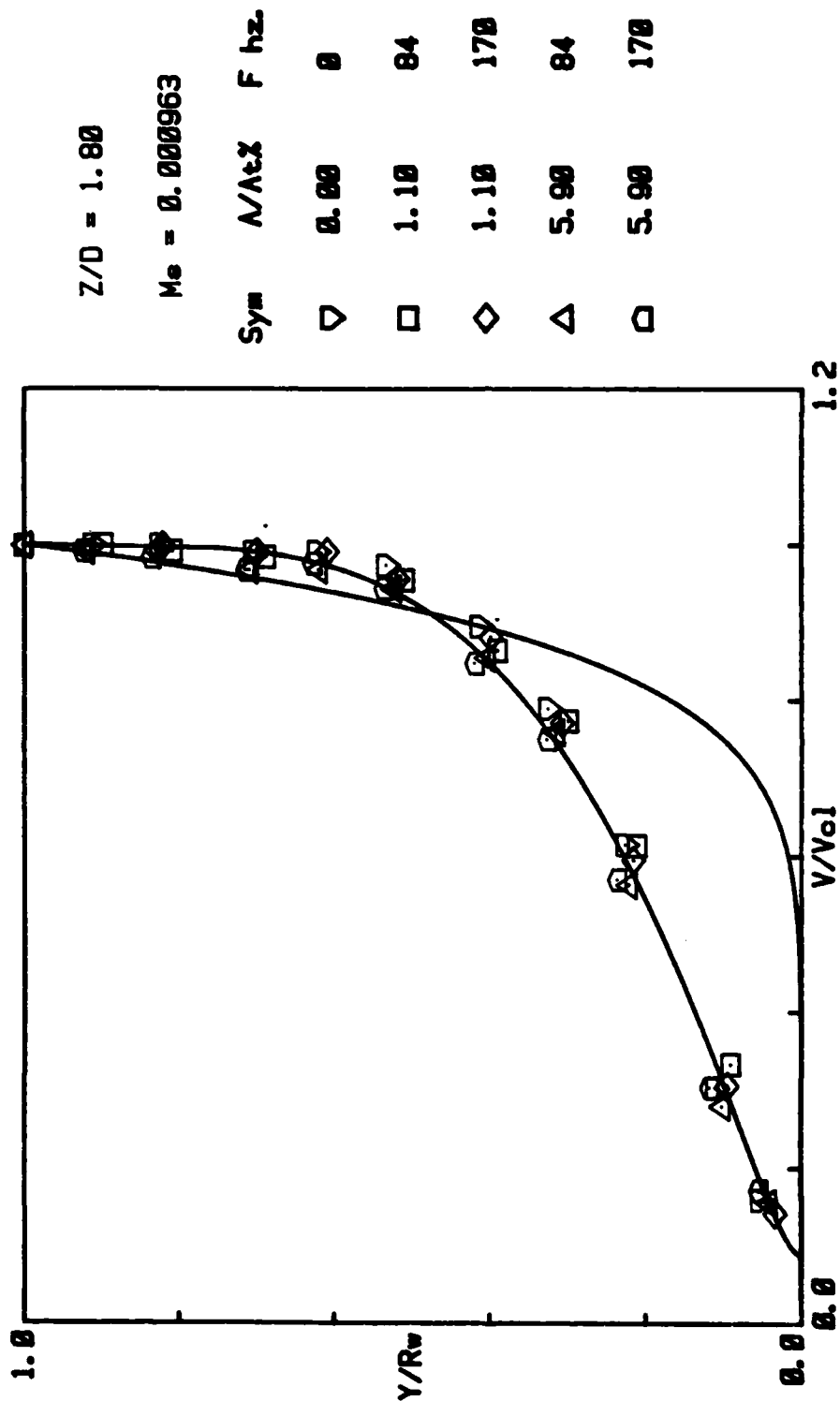


Figure 26.

law for turbulent pipe flow. Note that the data agree with BTC model predictions and also that driving amplitude and frequency have little effect. Thus, the flow nonlinearities in the near wall region do not have a significant effect on the gas speed.

Figures 27 through 36 show similar data at the higher surface Mach number of 0.0018. These data show basically the same overall behavior found at the lower surface Mach number. At the lower driving amplitude, however, the coherence shows a larger decrease mid-way between the centerline and the wall than was observed at the lower surface Mach number. Also the wall effect on the amplitude extends much farther into the case flow at the higher Mach number (at the lower driving amplitude).

Figures 37 through 46 show the corresponding results when the response of the surface was reduced by filling the annular flow distribution cavity with beads. While the qualitative behavior is similar, a number of potentially significant differences are apparent. Note that now the background turbulence is influenced by the presence of the acoustic wave. Second, the deviation from planar wave behavior near the wall are much larger, but the effect does not penetrate as far into the core flow.

To explore this near wall behavior further, two efforts are underway. First, Flandro's analysis is being modified to incorporate the acoustic wall conditions of cold flow experiment in his model, i.e. equation (5). Parametric studies will then be made to examine how the acoustic response of the wall influences the local acoustic velocity. In addition, preparations are being made to make split film anemometer measurements. These measurements will resolve the vector direction of the acoustic velocity in the r - z plane near the wall and thereby provide a better basis for comparing the data to the models.

TURBULENCE INTENSITY PROFILE

Z/D = 1.80 Freq = 84.00 Hz. $\lambda/\lambda_t = 0.60 \times$ $\text{Max}10^{13} = 1.80$

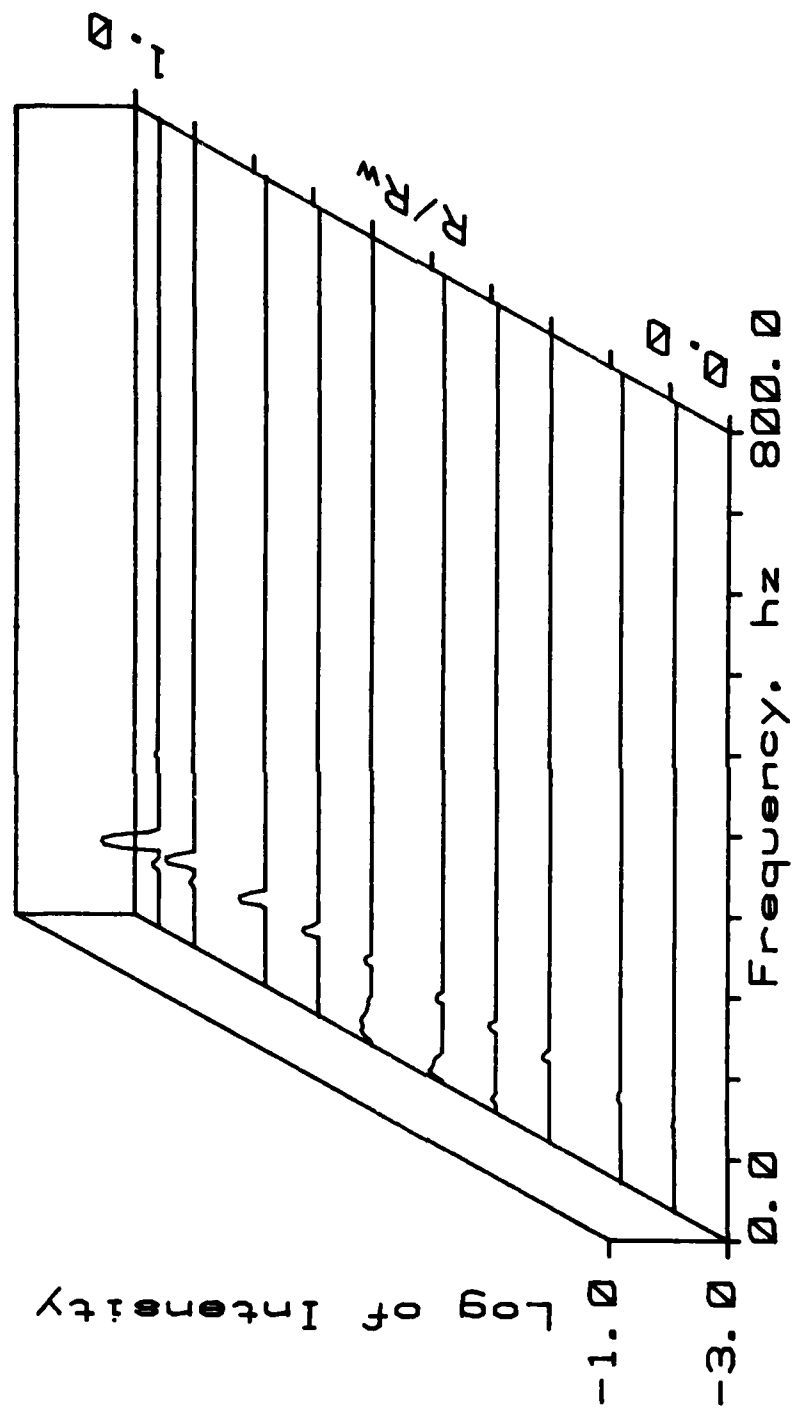


Figure 27.

TURBULENCE INTENSITY PROFILE

$Z/D = 1.80$ $\text{Freq} = 170.00 \text{ Hz.}$ $A/\Delta t = 0.60 \times 10^3$ $M \times 10^3 = 1.80$

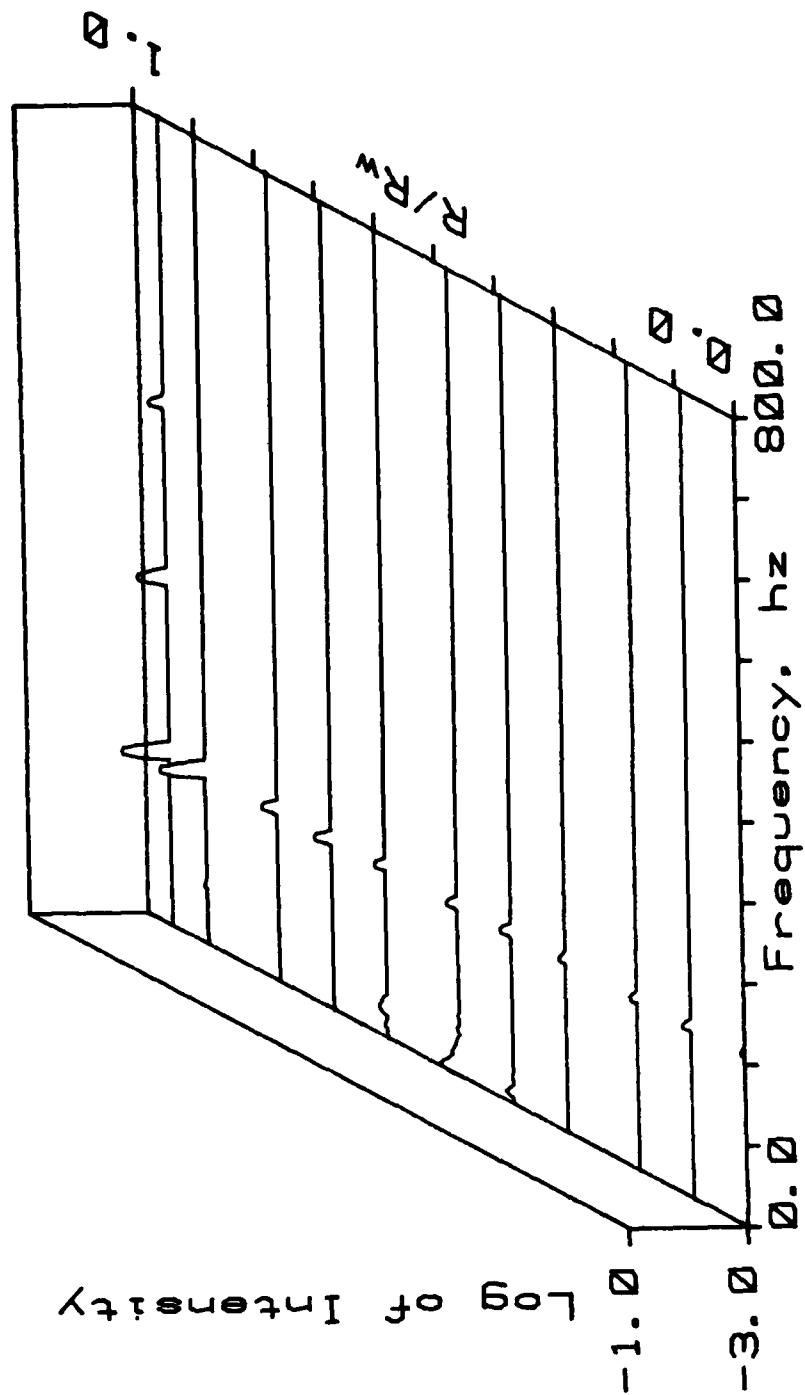


Figure 28.

TURBULENCE INTENSITY PROFILE

Z/D = 1.80 Freq = 84.00 Hz. $\Delta/\Delta t = 3.30 \times 10^{-3}$ Max1013 = 1.80

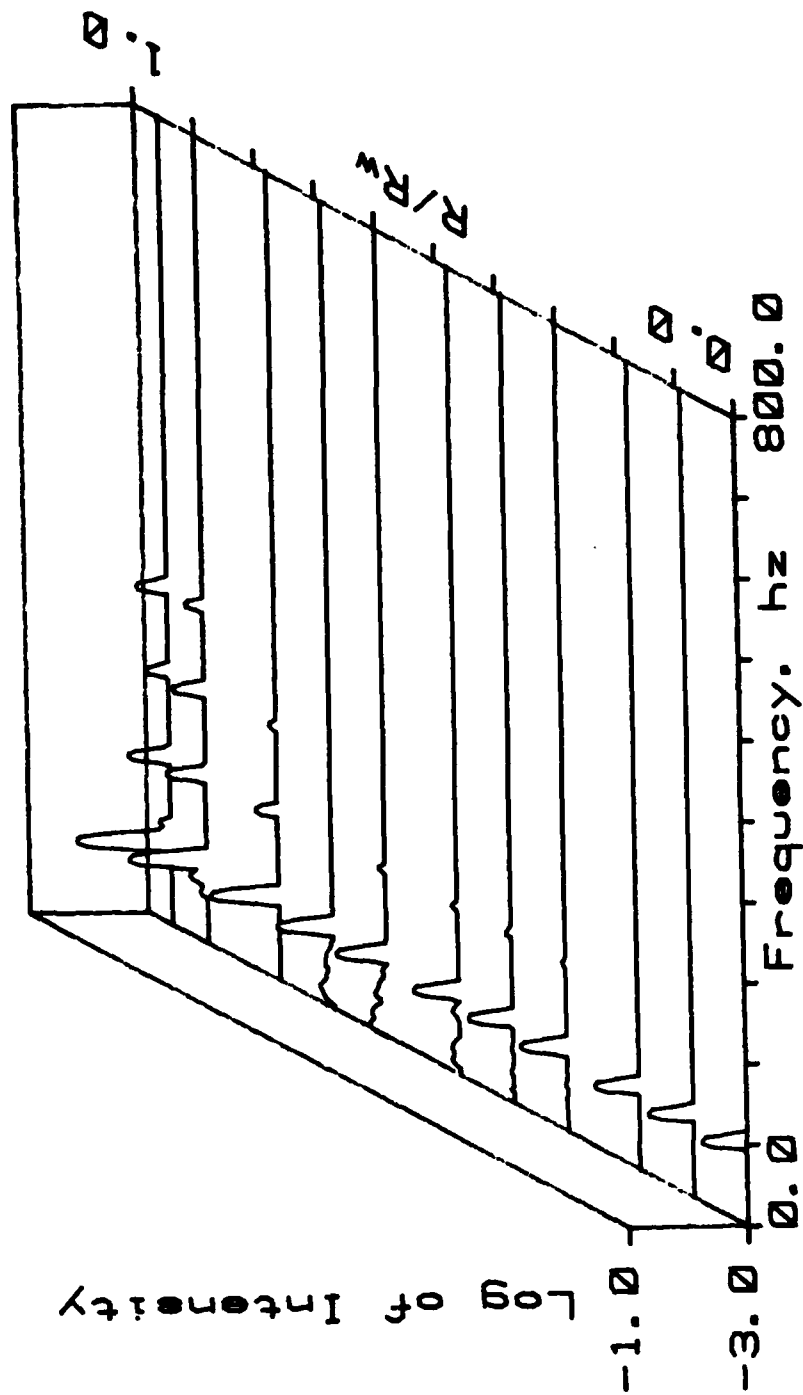


Figure 29.

TURBULENCE INTENSITY PROFILE

Z/D = 1.80 Freq = 170.00 Hz. $\Lambda/\Delta t = 3.30 \times 10^3$ $Mex10t3 = 1.80$

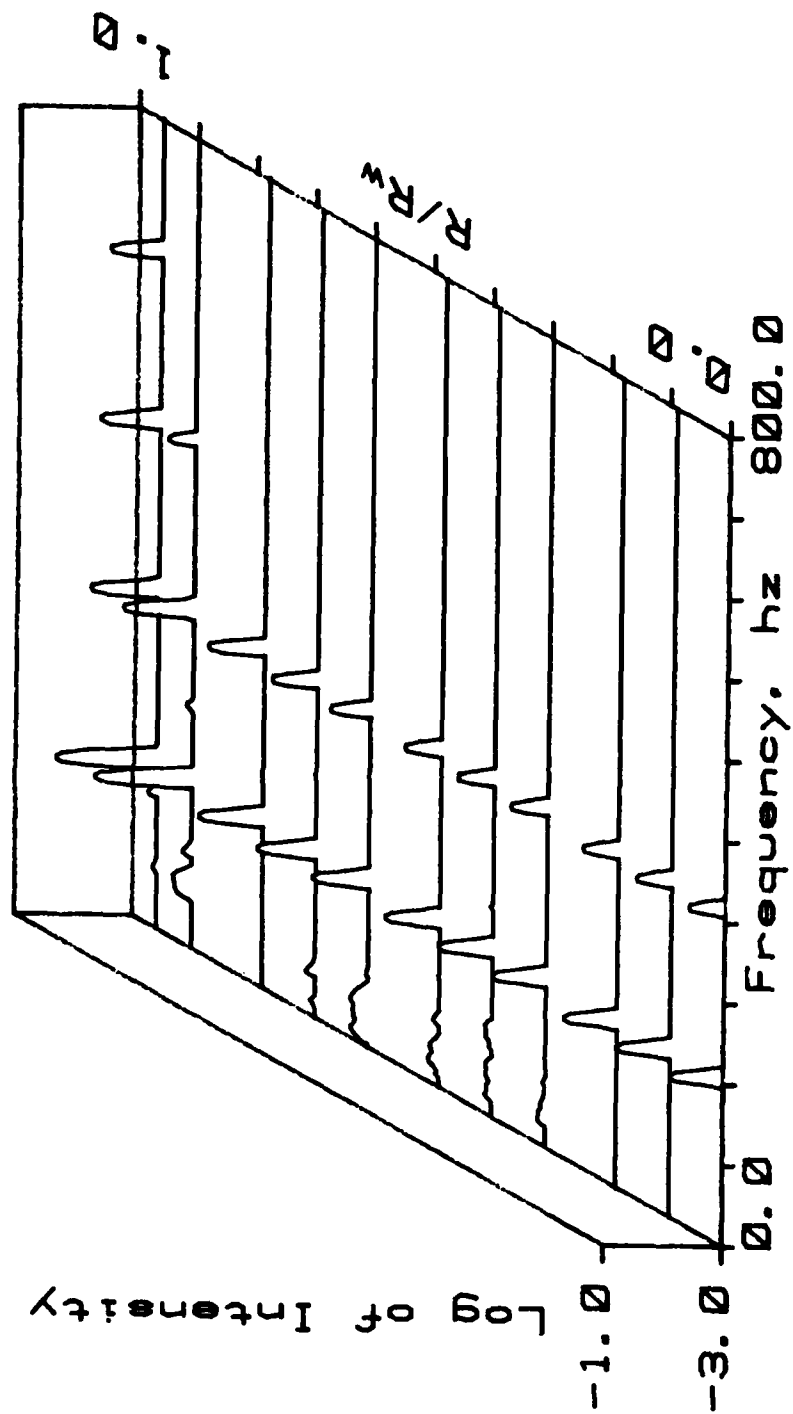


Figure 30.

TURBULENCE INTENSITY PROFILE

Z/D = 1.88 Freq = 0.00 Hz A/A_t = 0.00 X Max10f3 = 1.75

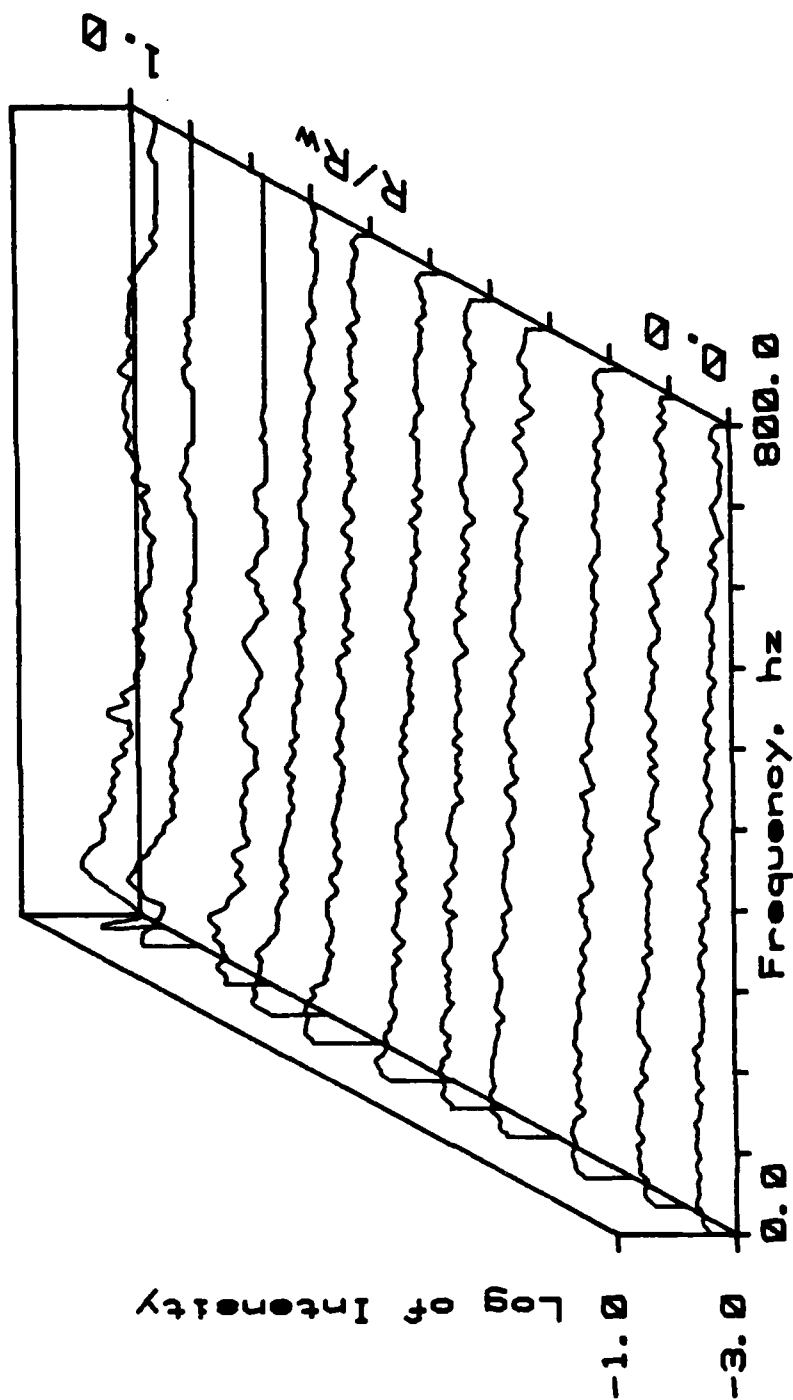


Figure 31.

NORMALIZED ACOUSTIC VELOCITY PROFILE

$Z/D = 1.80$ $\text{Freq} = 84.00$ $\Lambda/\Lambda_t = 0.60$ $\% \text{ Max} 10^{13} = 1.80$

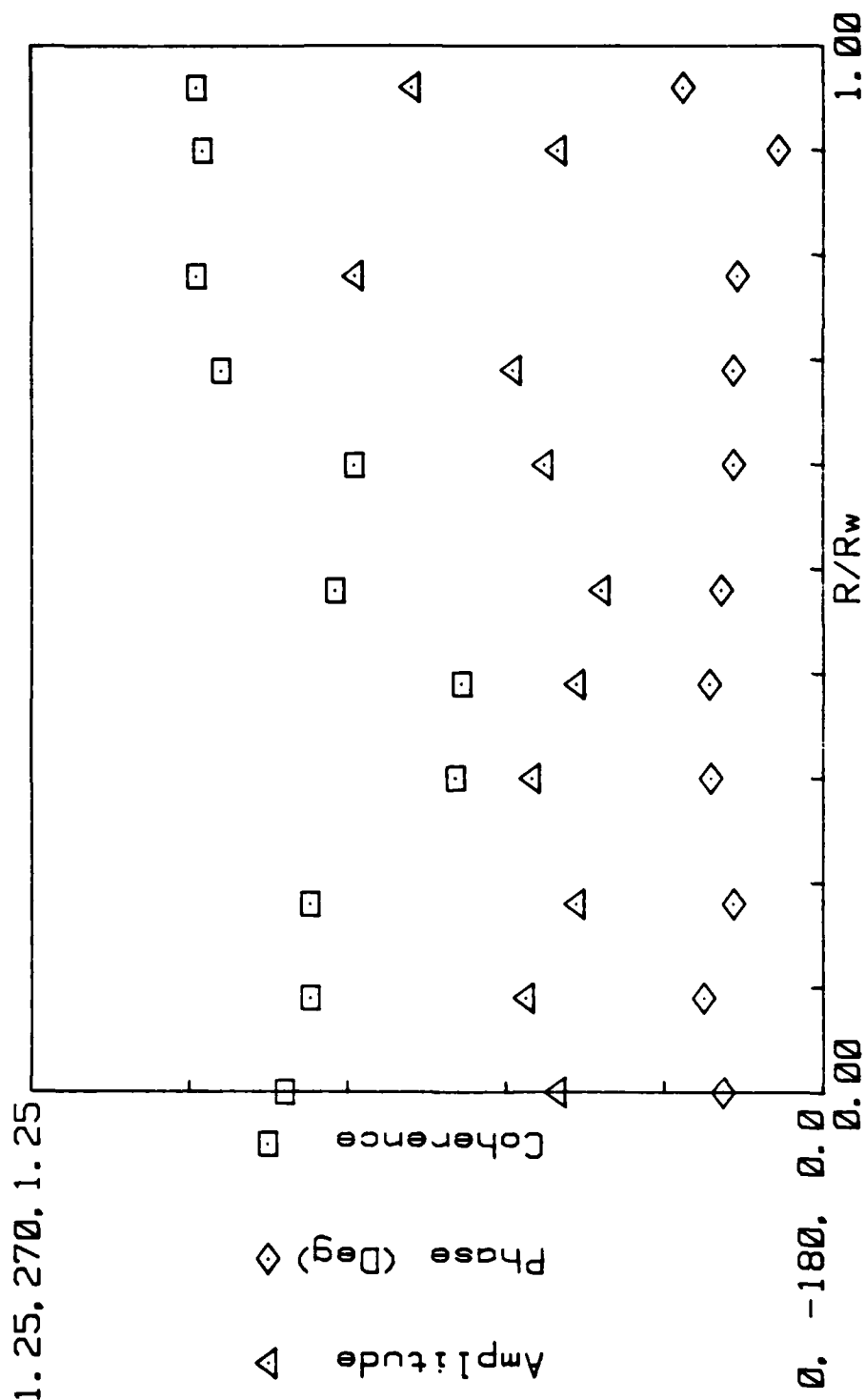


Figure 32.

NORMALIZED ACOUSTIC VELOCITY PROFILE

Z/D = 1.80 Freq = 170.00 $\Delta/\Delta t = 0.60 \times 10^{-3} = 1.80$

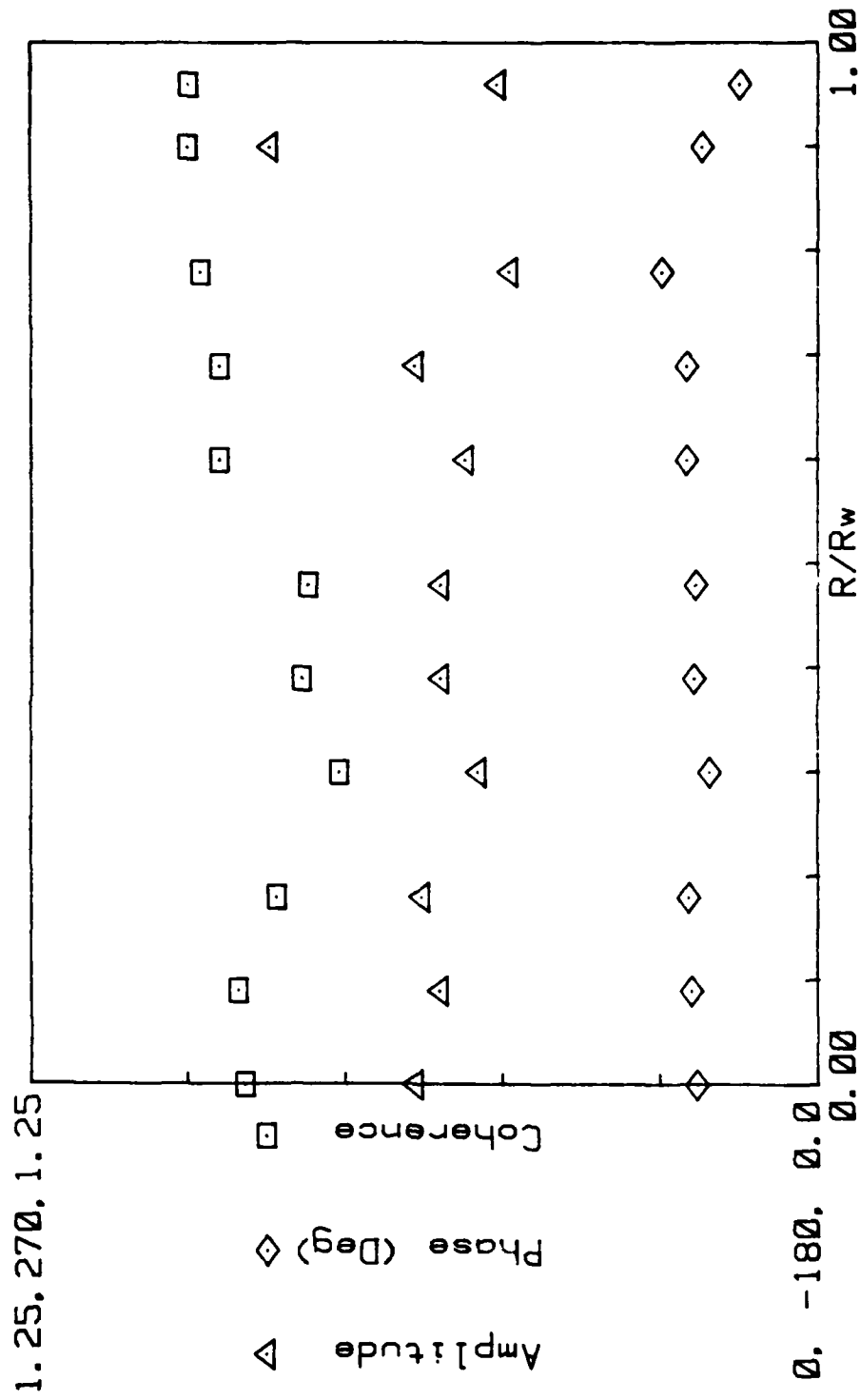


Figure 33.

NORMALIZED ACOUSTIC VELOCITY PROFILE

$Z/D = 1.80$ Freq = 84.00 $\Delta/\Delta t = 3.30 \times 10^{-3} = 1.80$

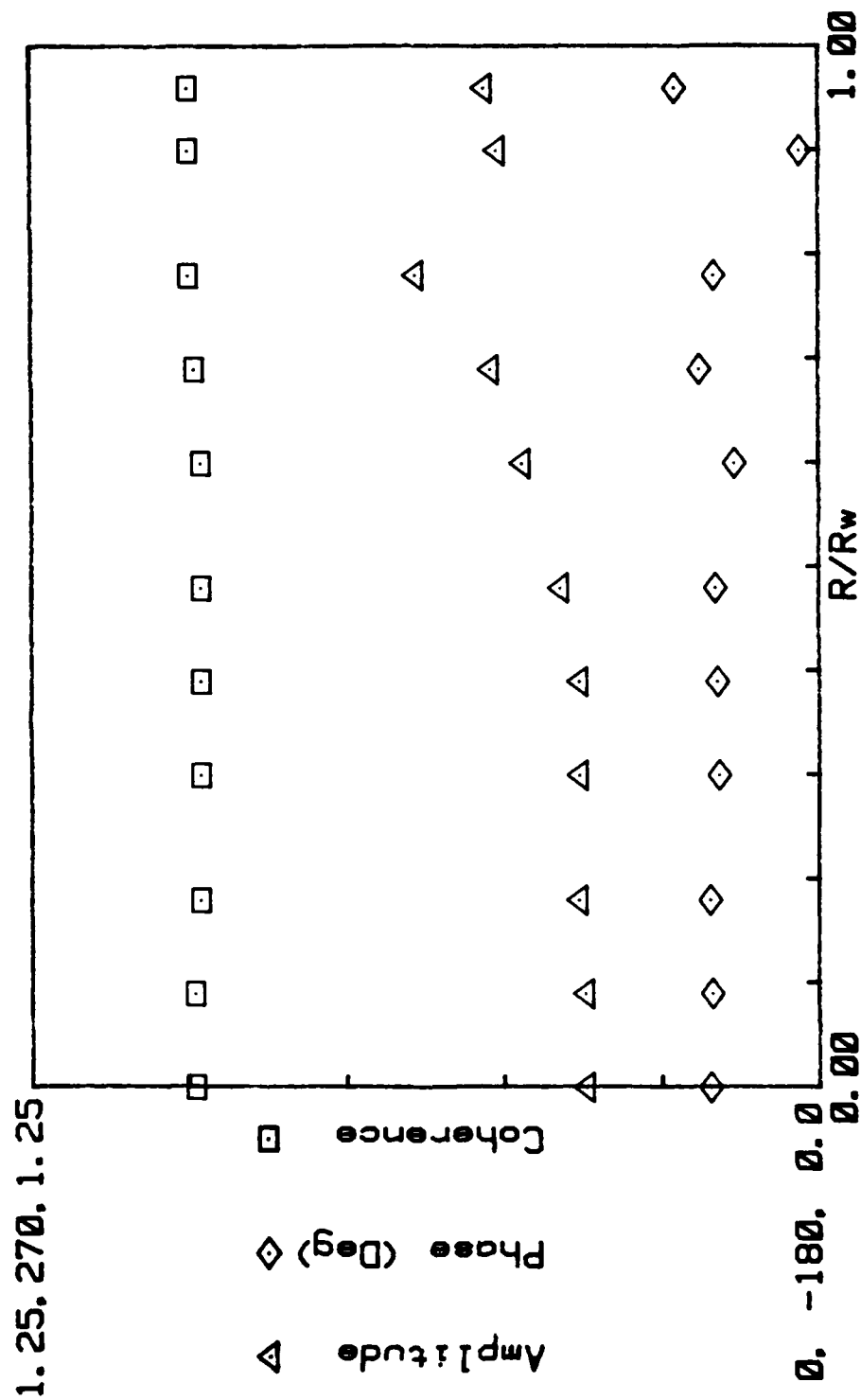


Figure 34.

NORMALIZED ACOUSTIC VELOCITY PROFILE

$Z/D = 1.00$ Freq = 178.00 A/Ac = 3.30 \times Max1013 = 1.00

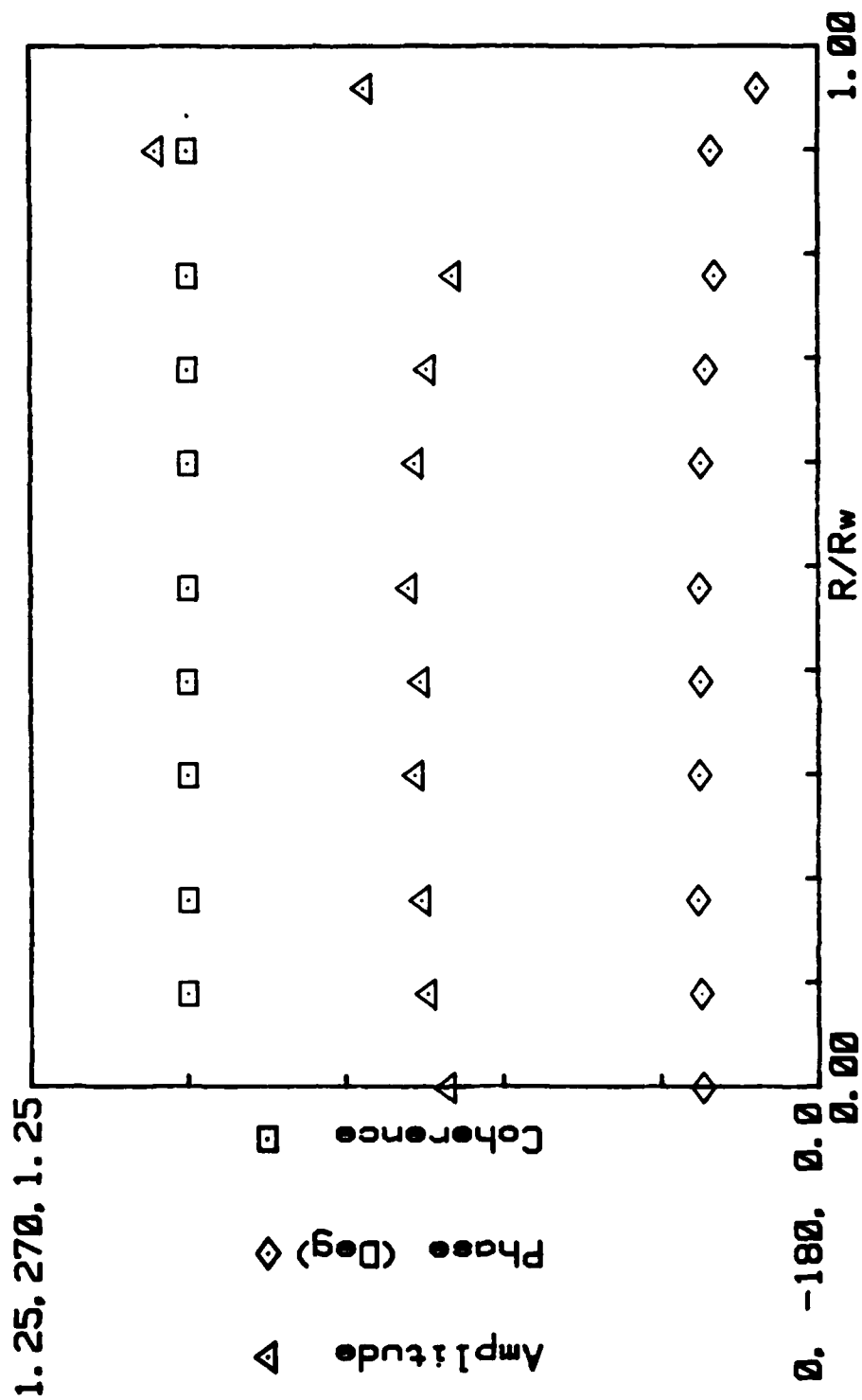


Figure 35.

MEAN VELOCITY PROFILE

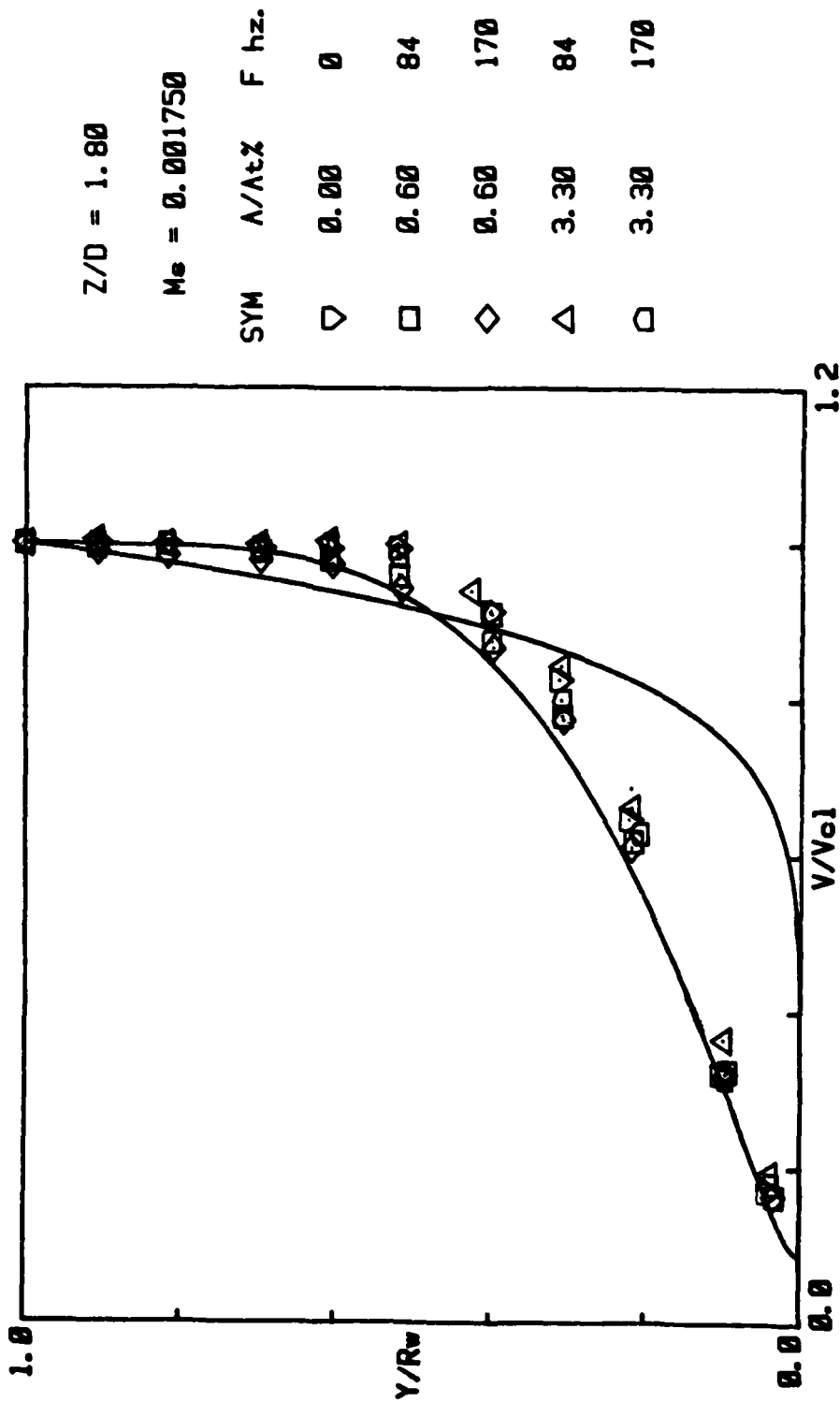


Figure 36.

TURBULENCE INTENSITY PROFILE

Z/D = 1.80 Freq = 65.00 Hz. $\Delta/\Delta t = 0.00 \times$ Max1013 = 1.00

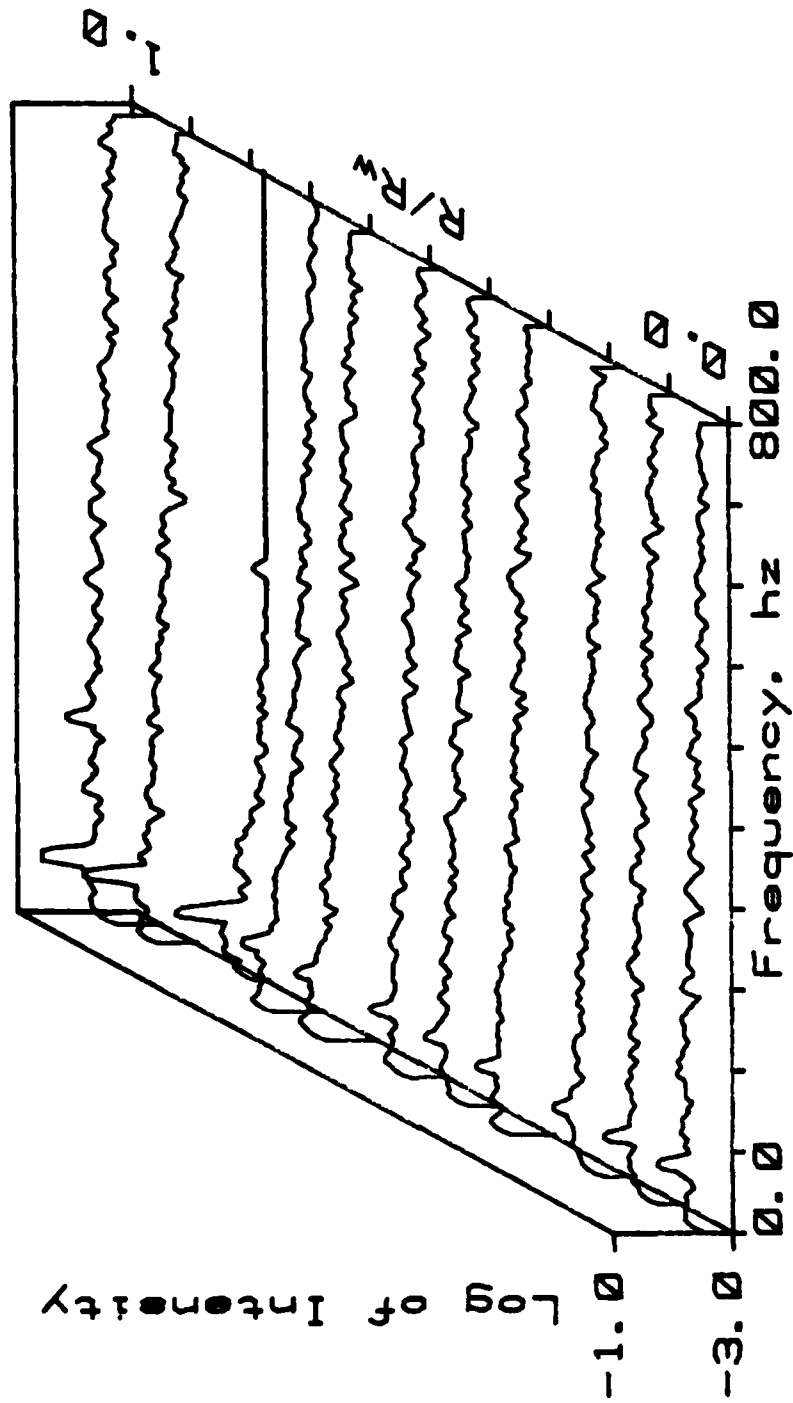


Figure 37.

TURBULENCE INTENSITY PROFILE

Z/D = 1.80 Freq = 135.00 Hz. $\Delta/\Delta t = 0.00 \times 10^{-3} = 1.00$

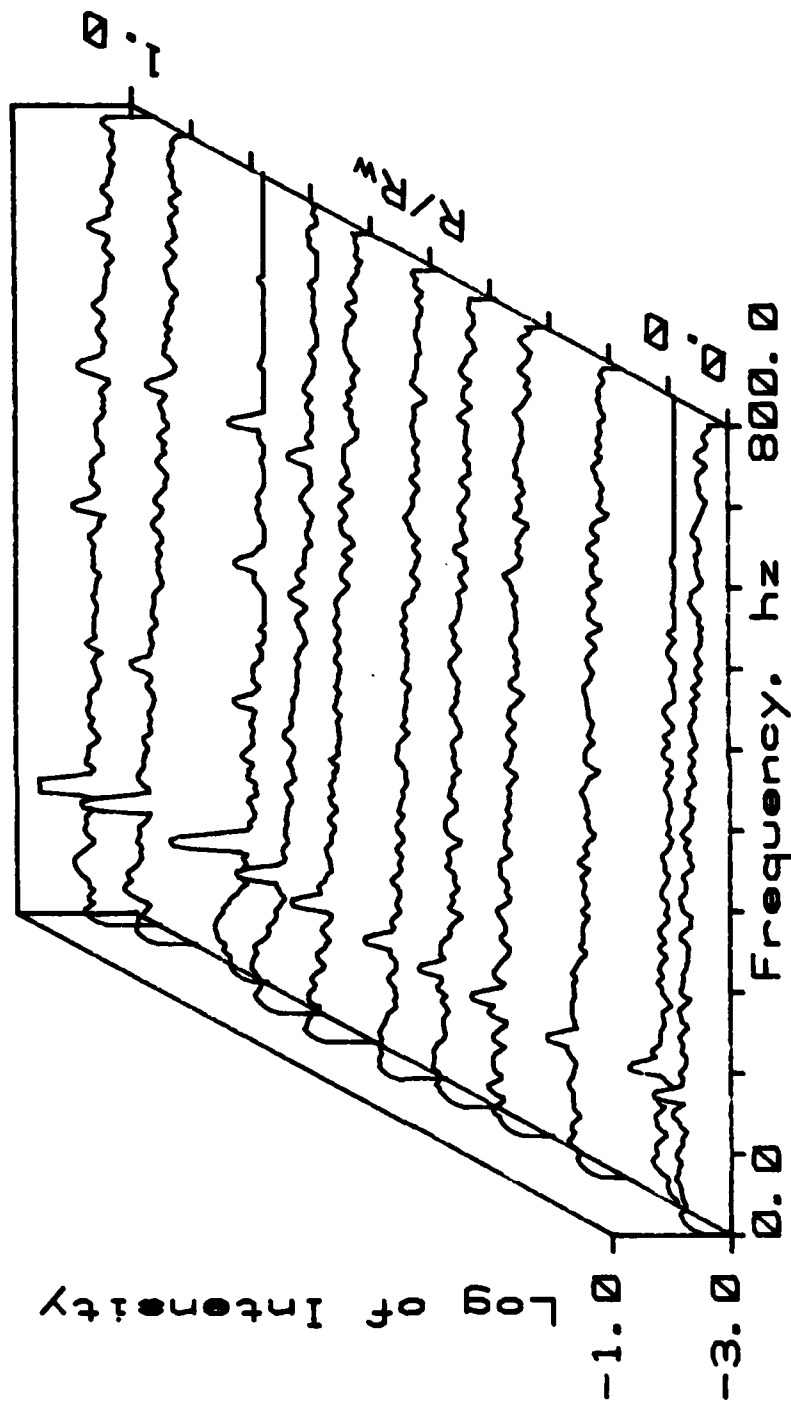


Figure 38.

TURBULENCE INTENSITY PROFILE

Z/D = 1.80 Freq = 65.00 Hz. $\Delta/\Delta t = 3.30 \times$ Max10f3 = 1.80

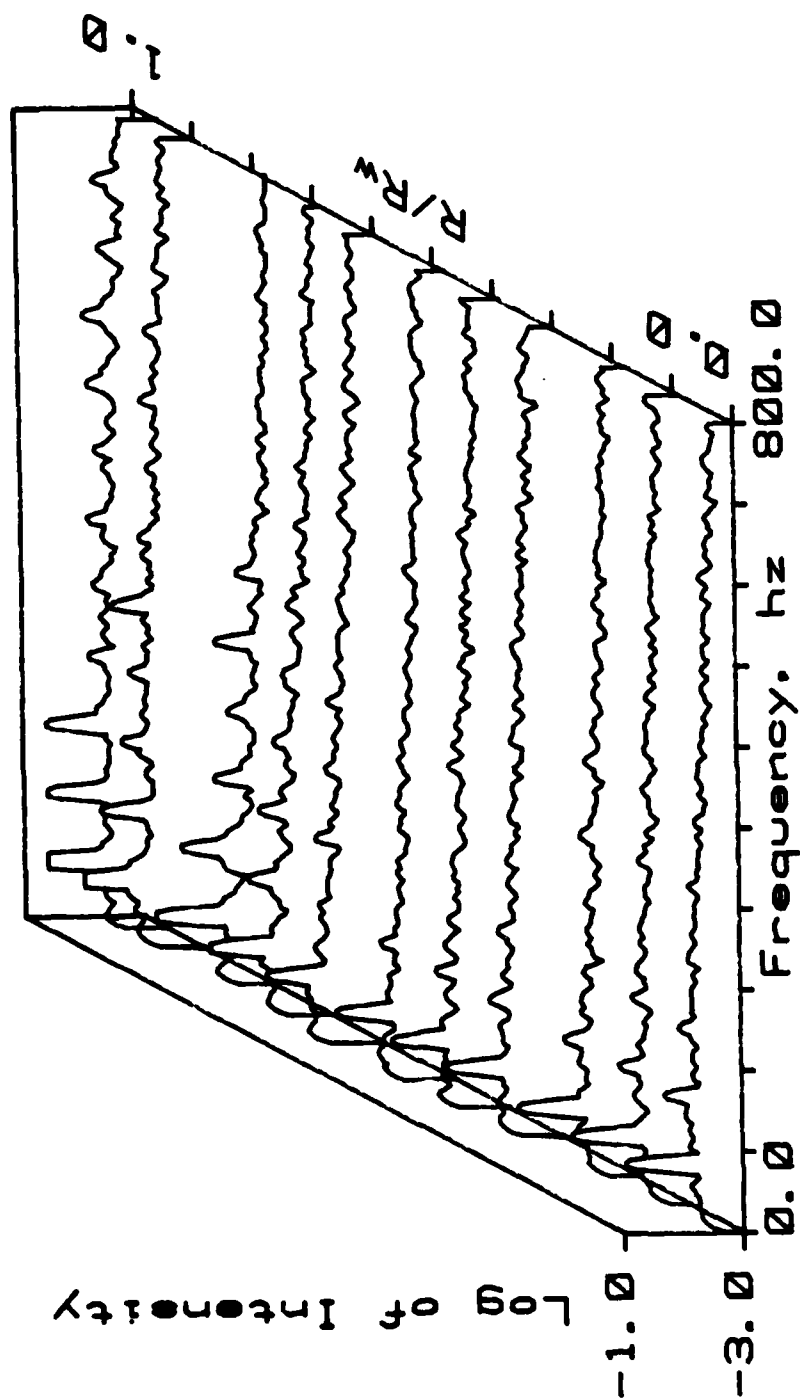


Figure 39.

TURBULENCE INTENSITY PROFILE

Z/D = 1.00 Freq = 135.00 Hz. $\Delta/\Delta t = 3.30 \times 10^{-3}$ Max10f3 = 1.00

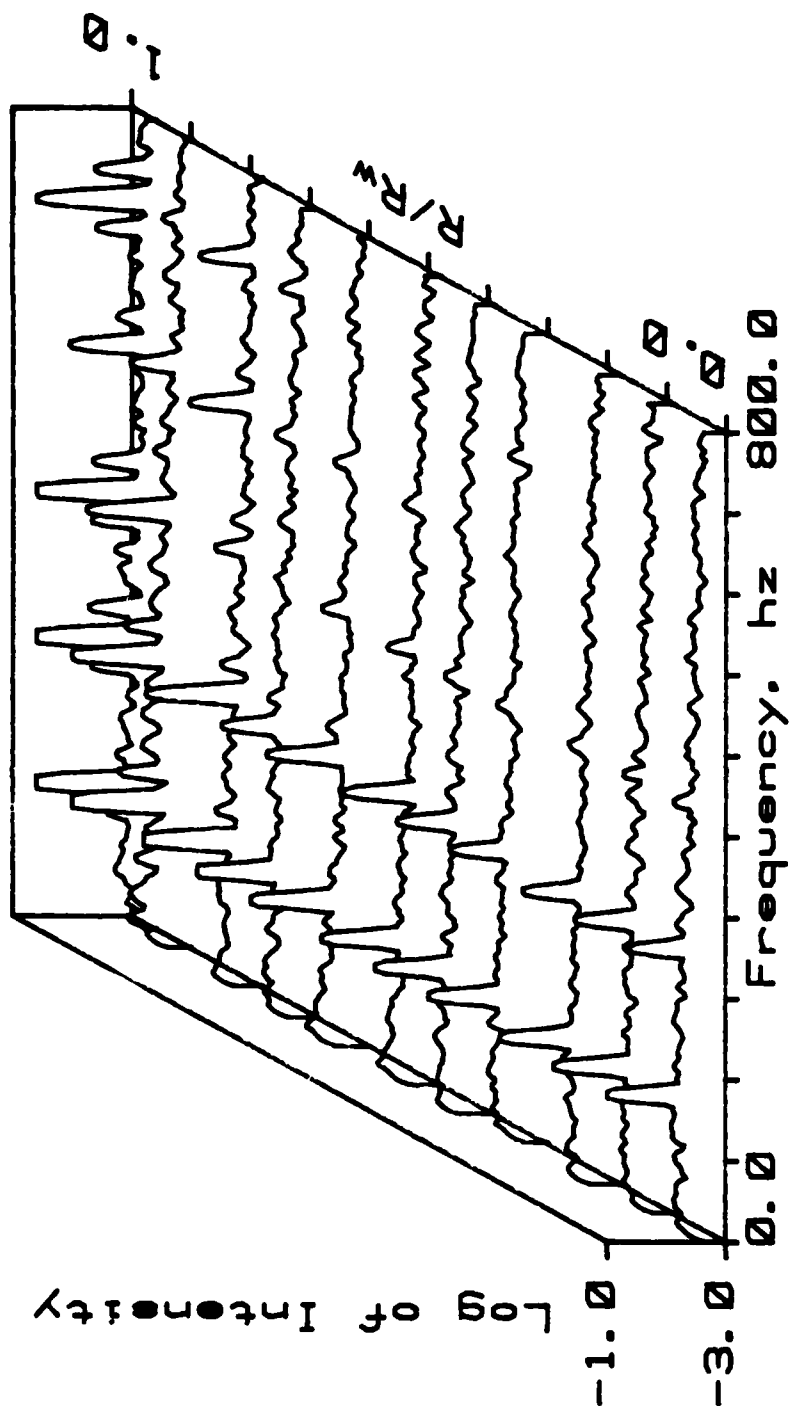


Figure 40.

TURBULENCE INTENSITY PROFILE

Z/D = 1.00 Freq = 0.00 Hz. $\Delta/\Delta t = 0.00 \times$ Max10t3 = 1.00

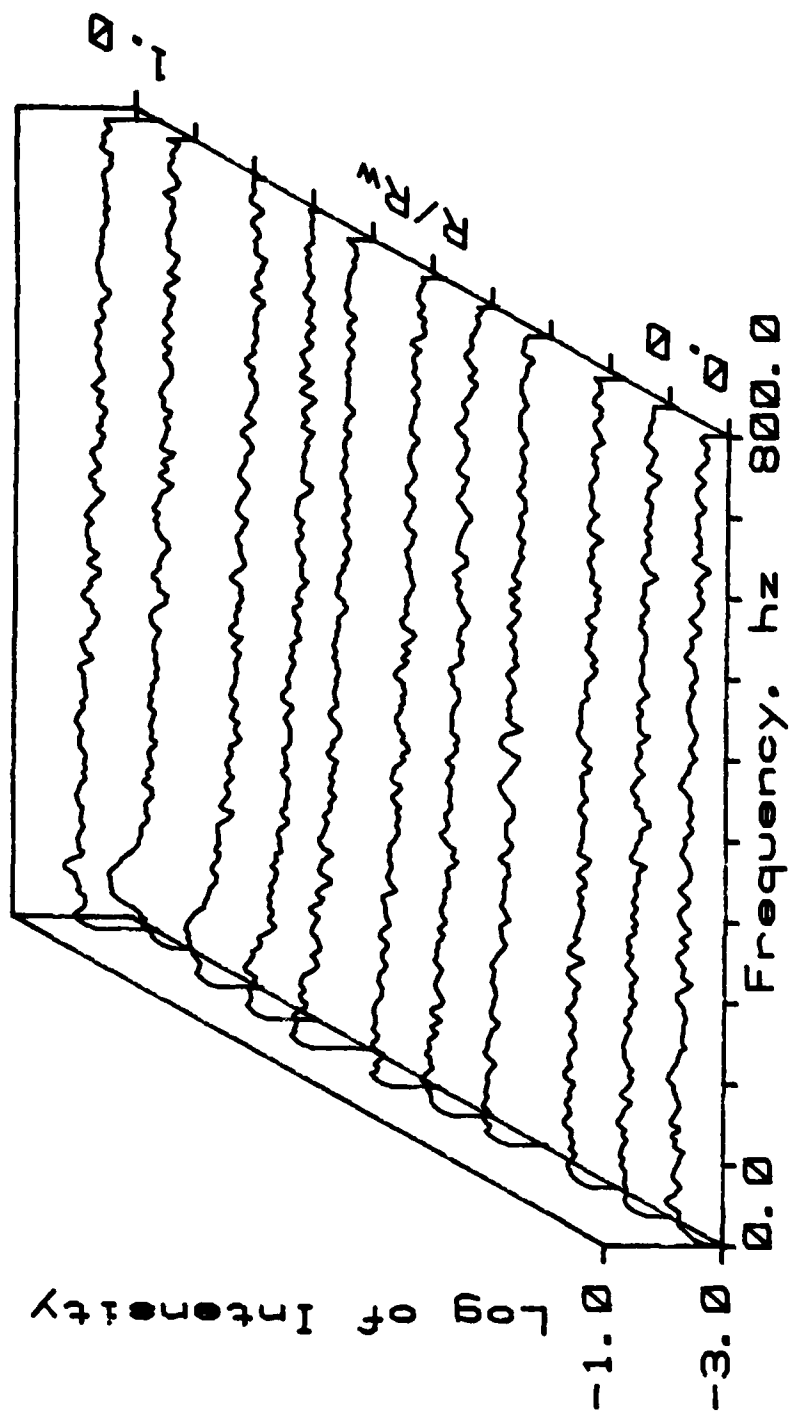


Figure 41.

NORMALIZED ACOUSTIC VELOCITY PROFILE

Z/D = 1.00 Freq = 65.00 A/Ac = 0.60 x Max10T3 = 1.00

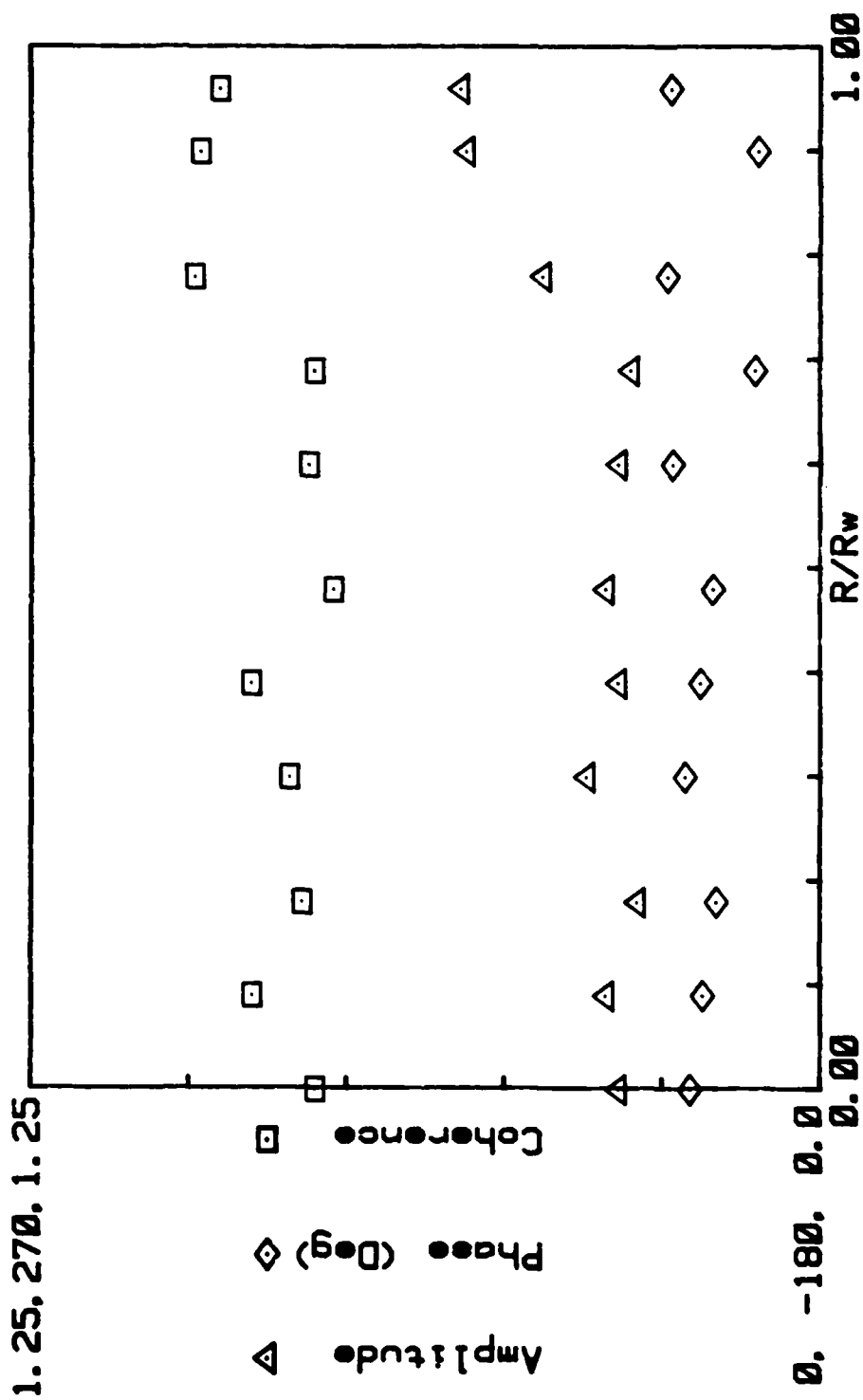


Figure 42.

NORMALIZED ACOUSTIC VELOCITY PROFILE

Z/D = 1.00 Freq = 135.00 A/Ac = 0.60 X Max1813 = 1.00

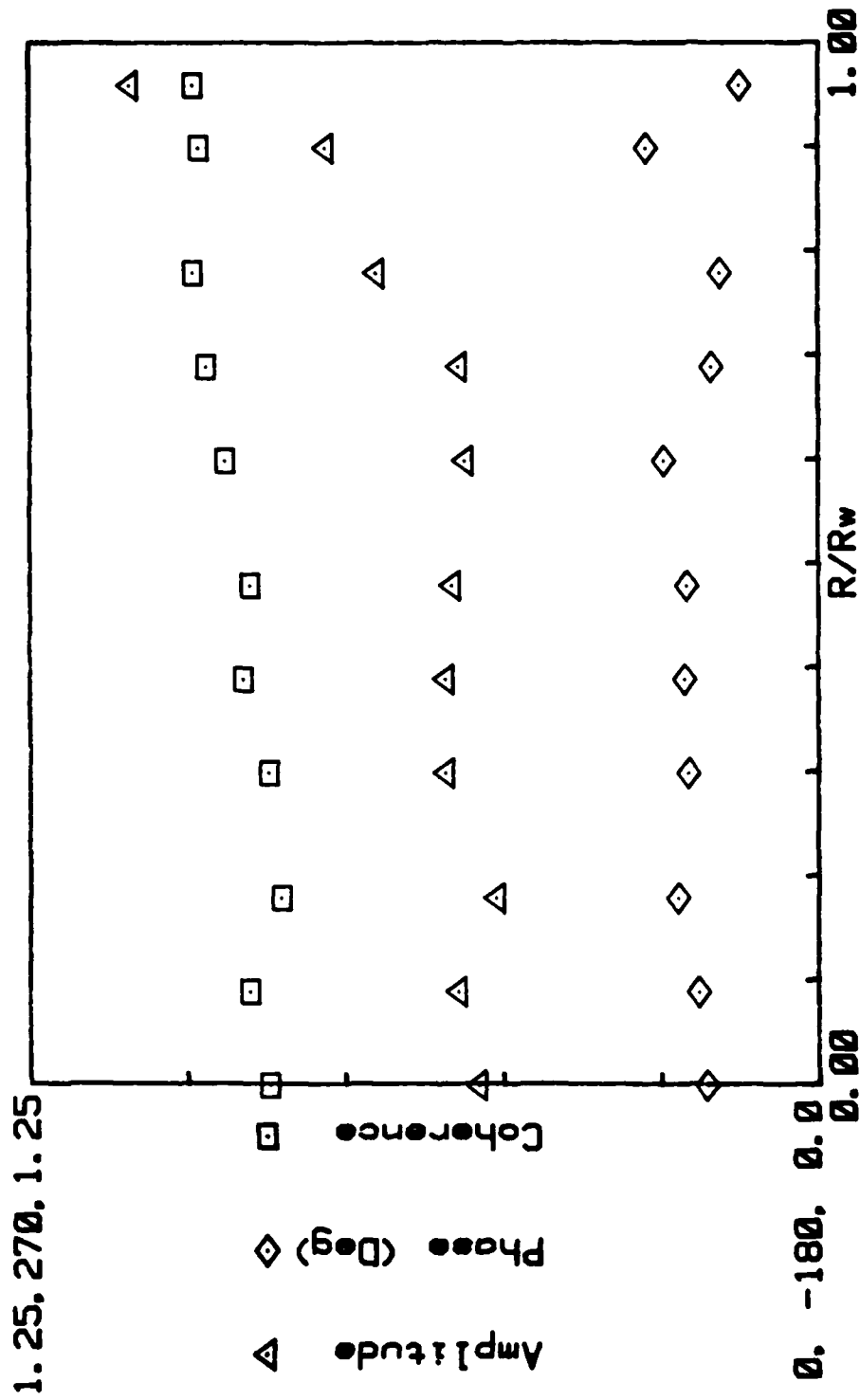


Figure 43.

NORMALIZED ACOUSTIC VELOCITY PROFILE

$Z/D = 1.00$ Freq = 65.00 A/Lt = 3.30 X Max18t3 = 1.00

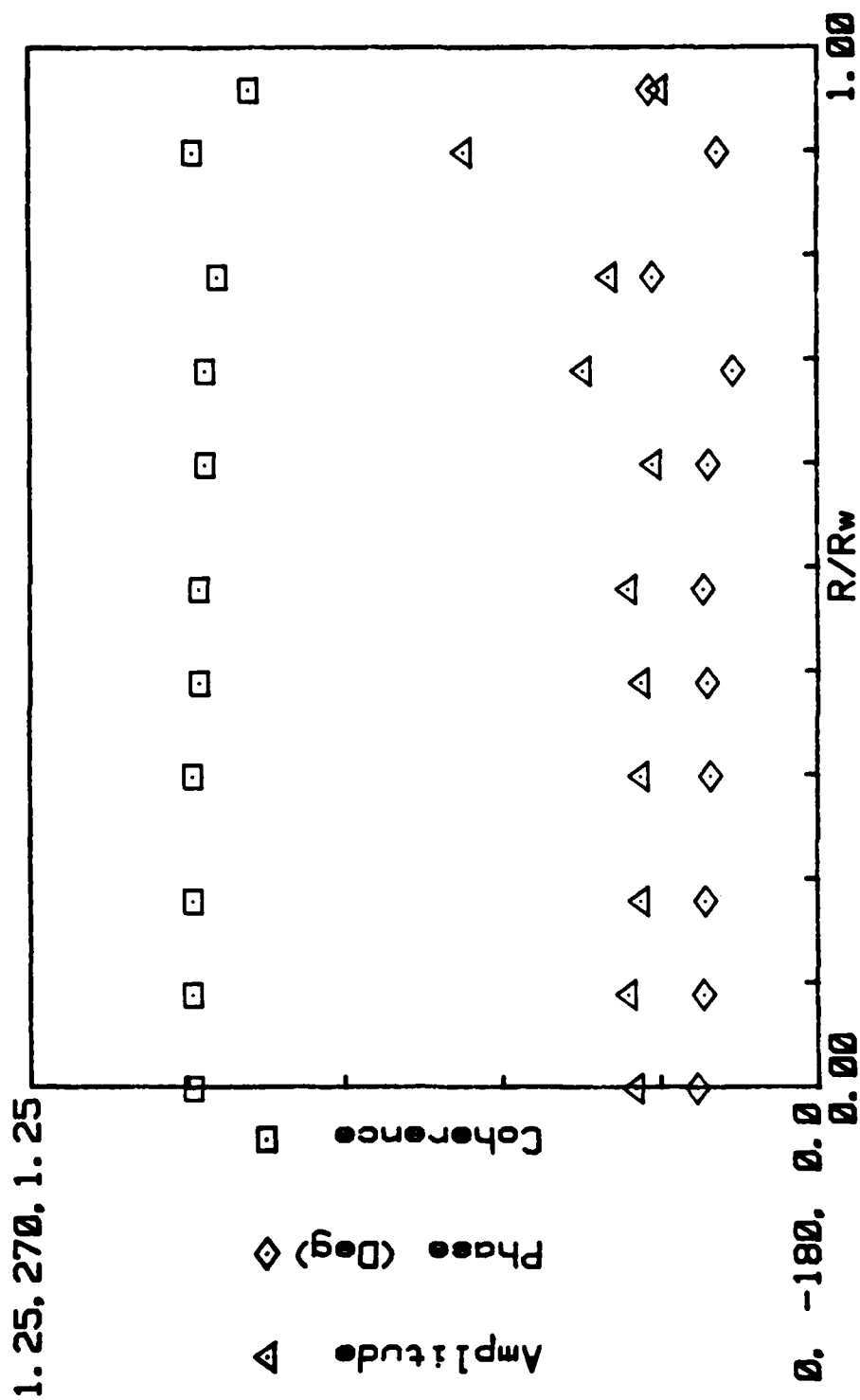


Figure 44.

NORMALIZED ACOUSTIC VELOCITY PROFILE

$Z/D = 1.00$ Freq = 135.00 $\lambda/\lambda_t = 3.30$ X Max1873 = 1.00

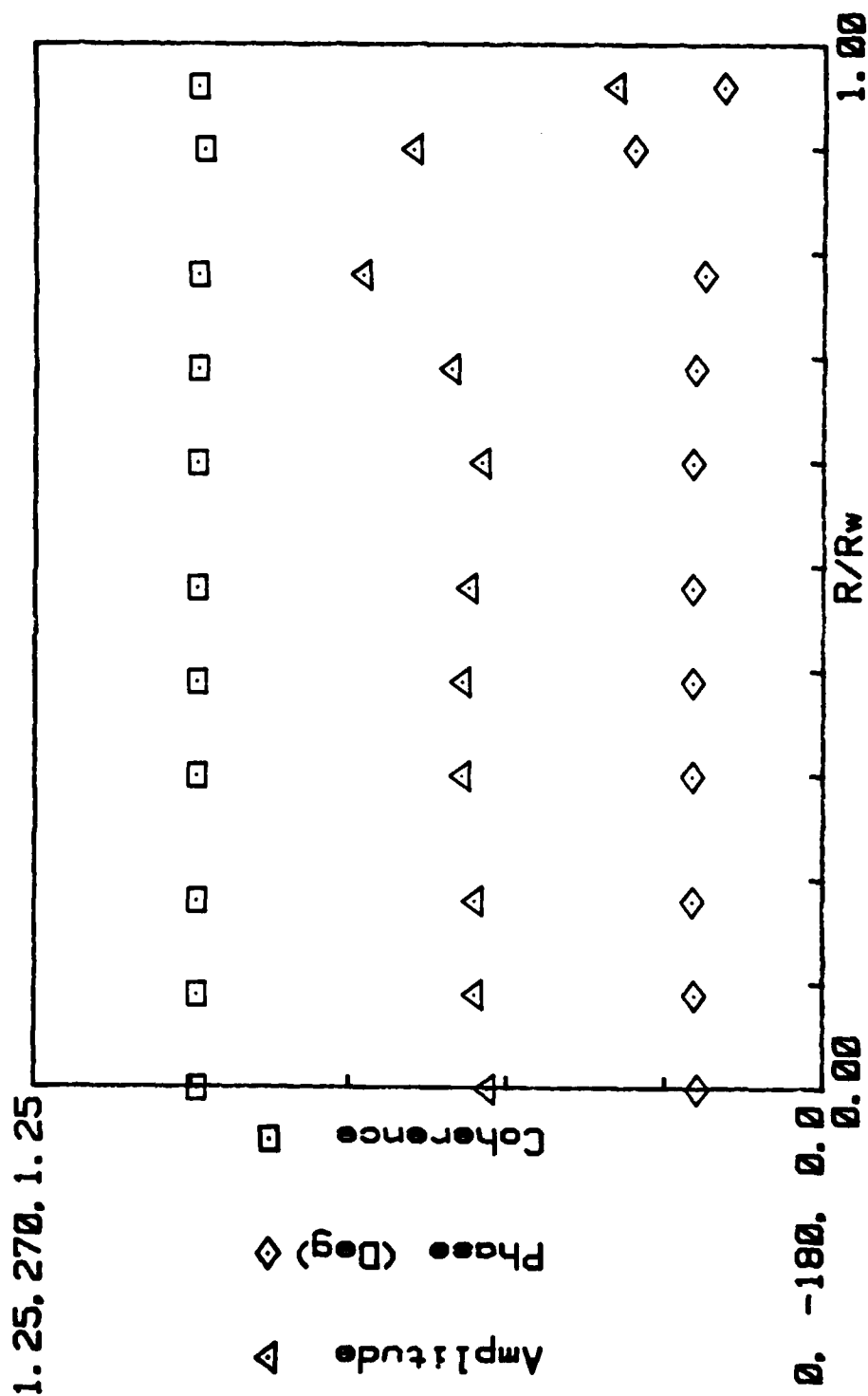


Figure 45.

MEAN VELOCITY PROFILE

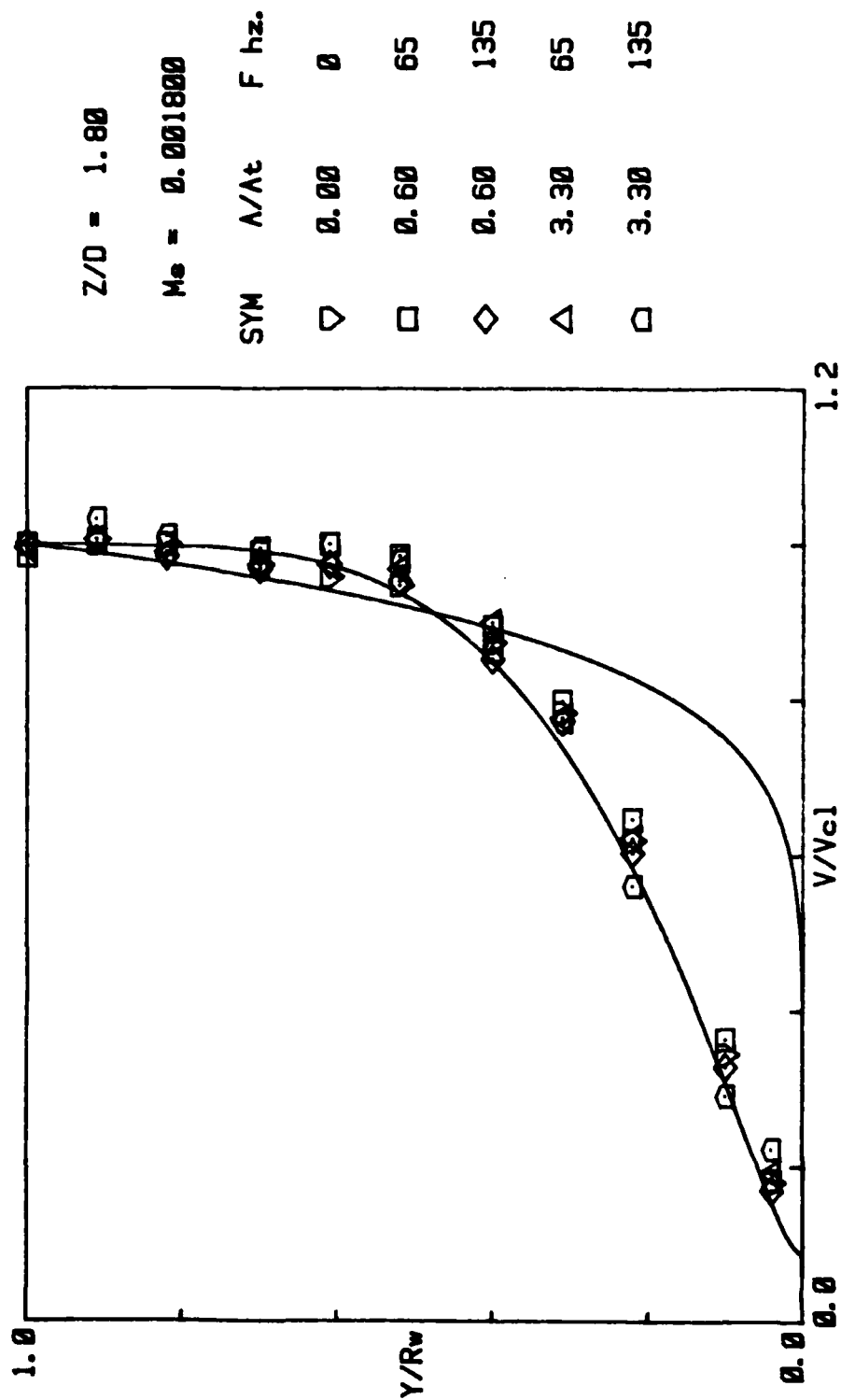


Figure 46.

Moving downstream, figures 47 through 51 show the radial distribution of the turbulence intensity spectra at $Z/D = 4.22$ for the low surface Mach number and the highly damped surface. Note, that the magnitude of the natural turbulence, as shown in Figure 51, increases significantly near the wall compared to the core flow. At the wall, there is also a strong peak in the spectra at the natural turbulence at approximately 70 hz. This suggests the flow has become inherently unstable and is transitioning to a more turbulent flow.

Comparing figures 47 through 50 with figure 51 shows that the frequency of this peak interacts with the acoustic wave. At the lower driving amplitudes, the background turbulence peak moves to a higher frequency. When the driving frequency approximates this frequency (figure 47), the acoustic wave is difficult to separate from the background turbulence. Furthermore, the harmonic content of the velocity oscillations has increased relative to the content at $Z/D = 1.8$. Also, note that the background turbulence is not damped by the presence of the acoustic waves.

At the higher driving amplitudes, the dominant frequencies are associated with the driving frequencies and its harmonics. The spectral peaks in the background turbulence have been reduced substantially and the spectra is more characteristic of fully developed turbulence. It is also apparent that the nonlinear behavior now extends from the wall all the way to the centerline at the higher acoustic pressure. This suggests that either the acoustic wall interactions are larger at this location, or that nonlinear flow structures from upstream locations are mingling with the locally generated nonlinear flow structures.

TURBULENCE INTENSITY PROFILE

Z/D = 4.22 Freq = 84.00 Hz. A/A_t = 1.10 x Max10f3 = 1.00

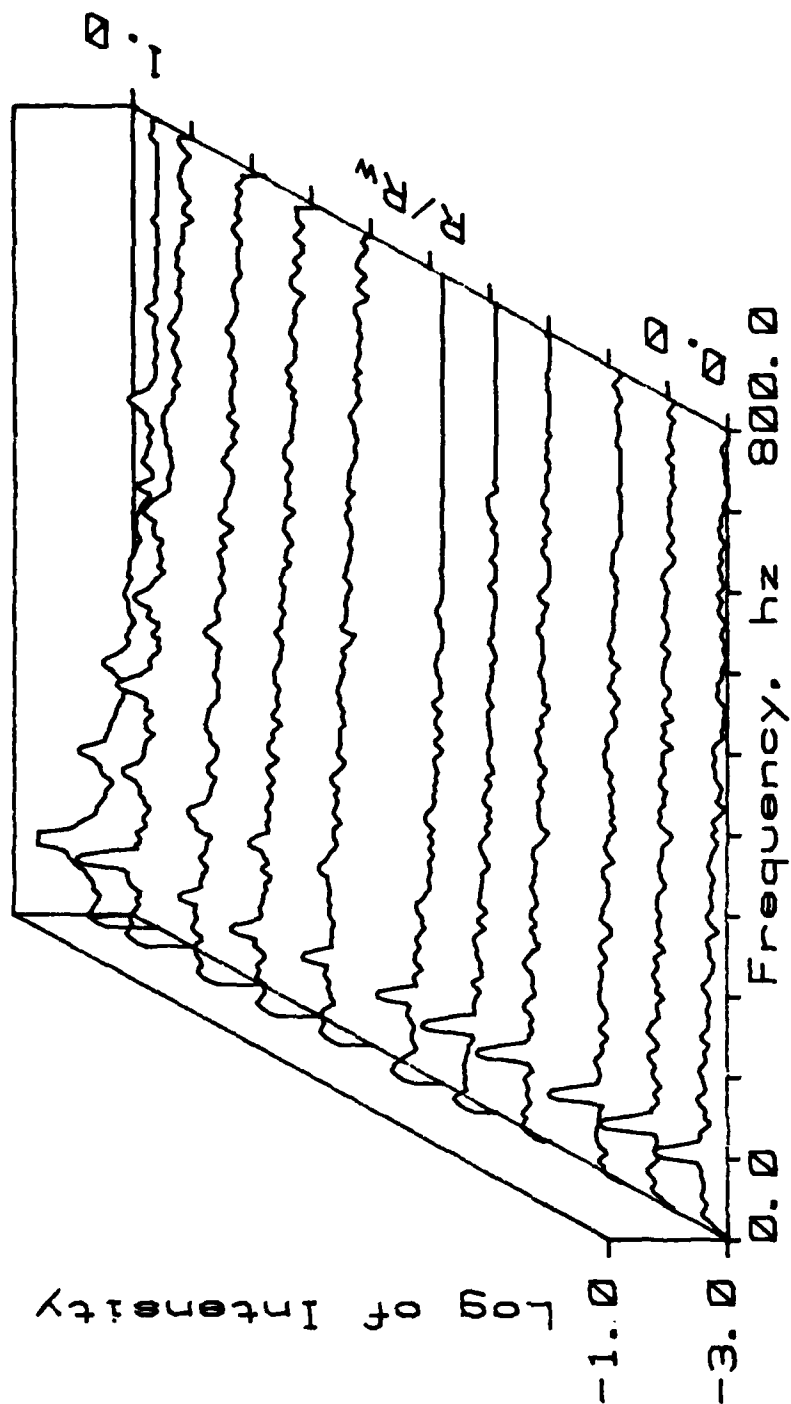


Figure 47.

TURBULENCE INTENSITY PROFILE

Z/D = 4.22 Freq = 170.00 Hz. $\Delta/\Delta t = 1.10 \times 10^{-3}$ Max 1013 = 1.00

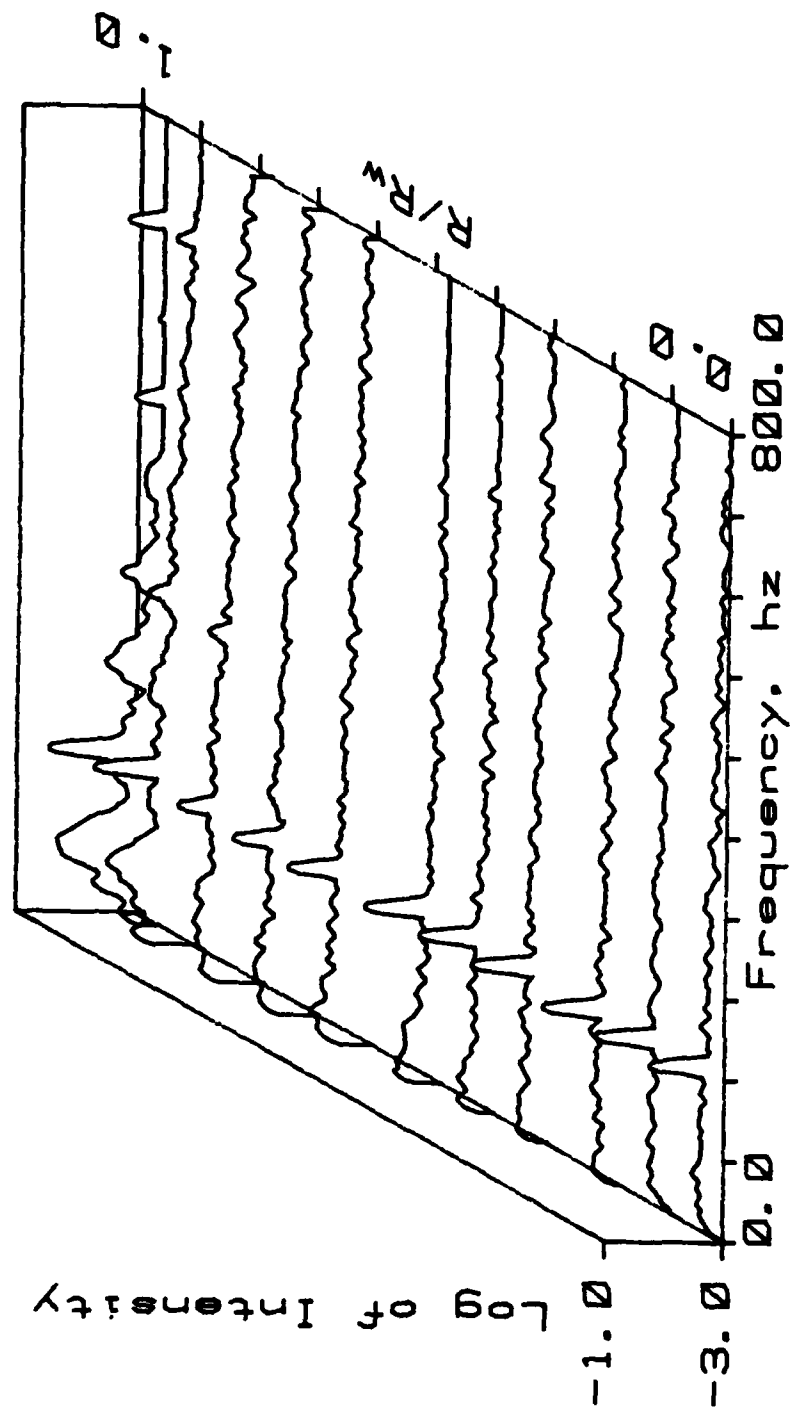


Figure 48.

TURBULENCE INTENSITY PROFILE

Z/D = 4.22 Freq = 84.00 Hz. $\Delta/\Delta t = 5.60 \%$ $\text{Max}10f3 = 1.00$

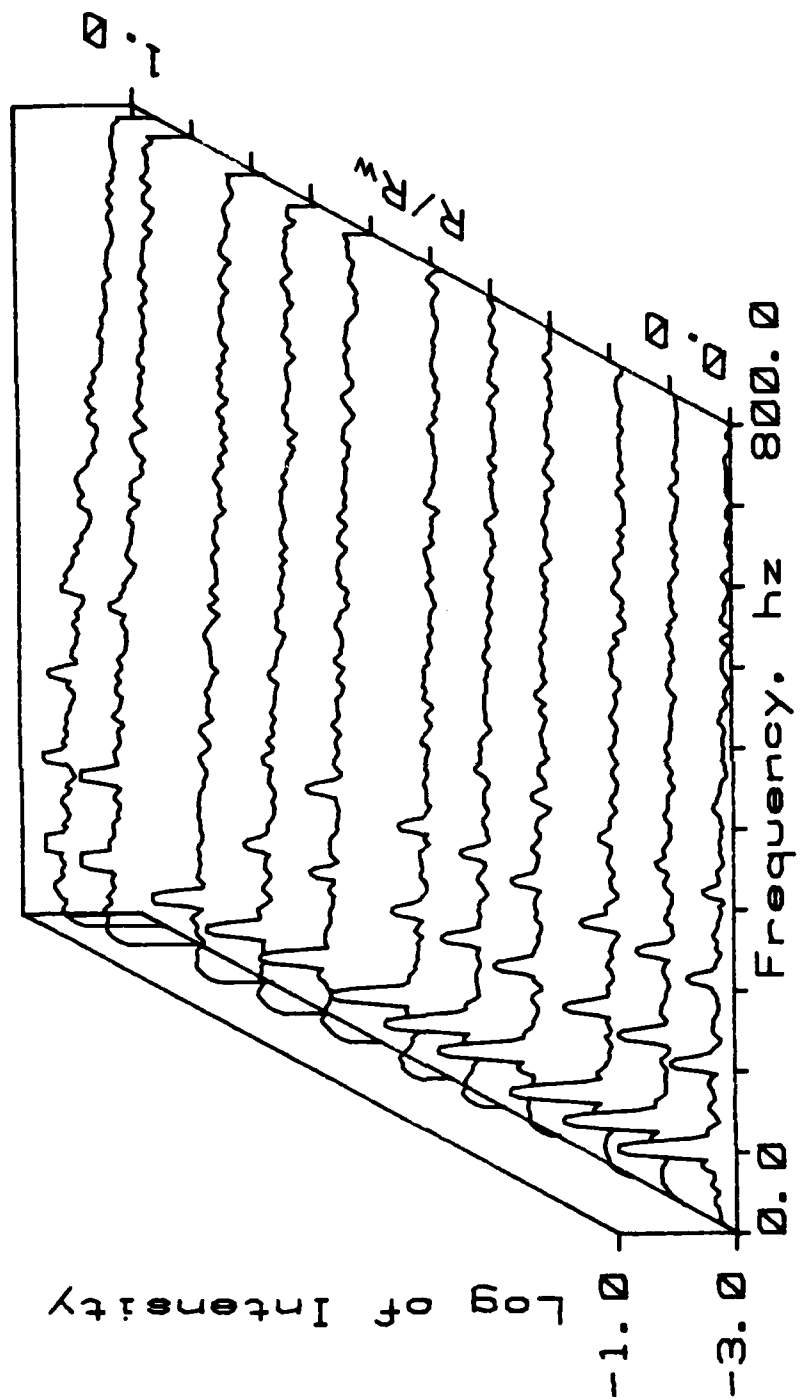


Figure 49.

TURBULENCE INTENSITY PROFILE

Z/D = 4.22 Freq = 170.00 Hz. $\Delta/\Delta t = 5.60 \times$ Max10t3 = 1.00

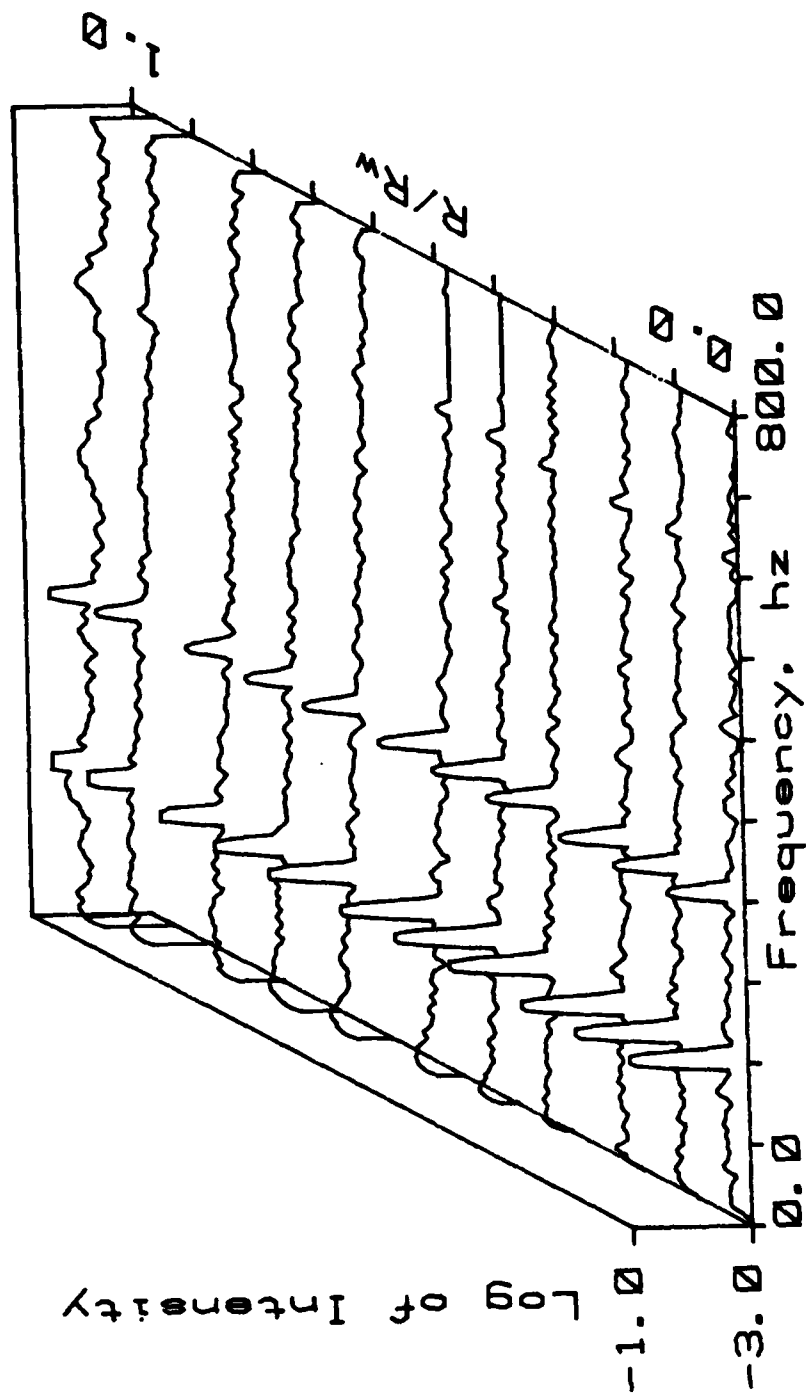


Figure 50.

TURBULENCE INTENSITY PROFILE

Z/D = 4.22 Freq = 0.00 Hz. $\Lambda/\Lambda_c = 0.00 \times$ $M_{\infty} \times 10^3 = 1.00$

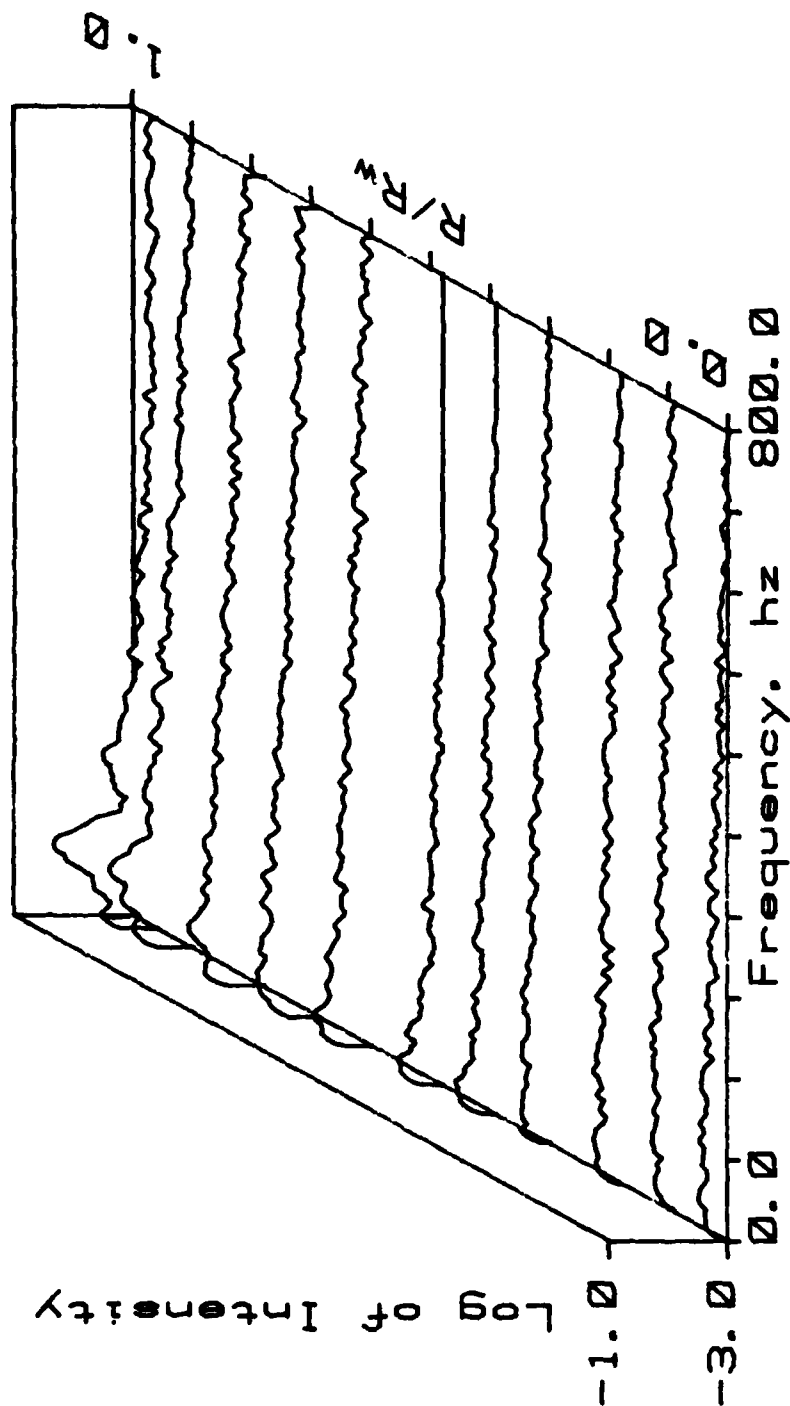


Figure 51.

Acoustic wave analyses of these data are shown in figures 52 to 55. At the lower driving, the acoustic wave is nearly planar in the core; but near the wall, there are significant shifts in the amplitude, phase, and coherence. At higher driving, these shifts from planar behavior are smaller; in fact at the higher frequency, the waves appear planar all the way to the wall.

The mean velocity profiles shown in figure 56 now indicate there is some deviation from the BTC profile near the wall, but reasonable agreement still seems to exist in the core flow. Also the oscillations have no effect on the profile including the near wall region.

Turbulence intensity spectra, acoustic wave behavior, and the mean velocity profiles at the higher surface Mach number for both the surface responses are shown in Appendix B. Qualitatively these data show similar behavior to the lower Mach number data. They confirm the increase in near wall turbulence, a tendency for organized turbulent background oscillations near the wall, and their interactions with the acoustic waves. The characteristics of the acoustic wave across the port are also very similar to the data for the lower Mach number.

Moving down to $Z/D = 11.5$, figures 57 through 61 show the turbulence intensity spectra for the lower surface Mach number tests. Figures 62 through 65 show the corresponding acoustic wave analysis of these same data. At the lower driving amplitude, the driven velocity oscillations are confined to the core flow. It appears that the turbulence in the near wall region has sufficient energy to prevent any significant increase in the oscillatory velocity near the wall at the driving frequency. This explains the corresponding absence of driven heat transfer oscillations at this axial location. At the higher driving amplitude, the nonlinear behavior is confined to the core flow

NORMALIZED ACOUSTIC VELOCITY PROFILE

$Z/D = 4.22$ Freq = 84.00 A/Ac = 1.18 \times Max10t3 = 1.00

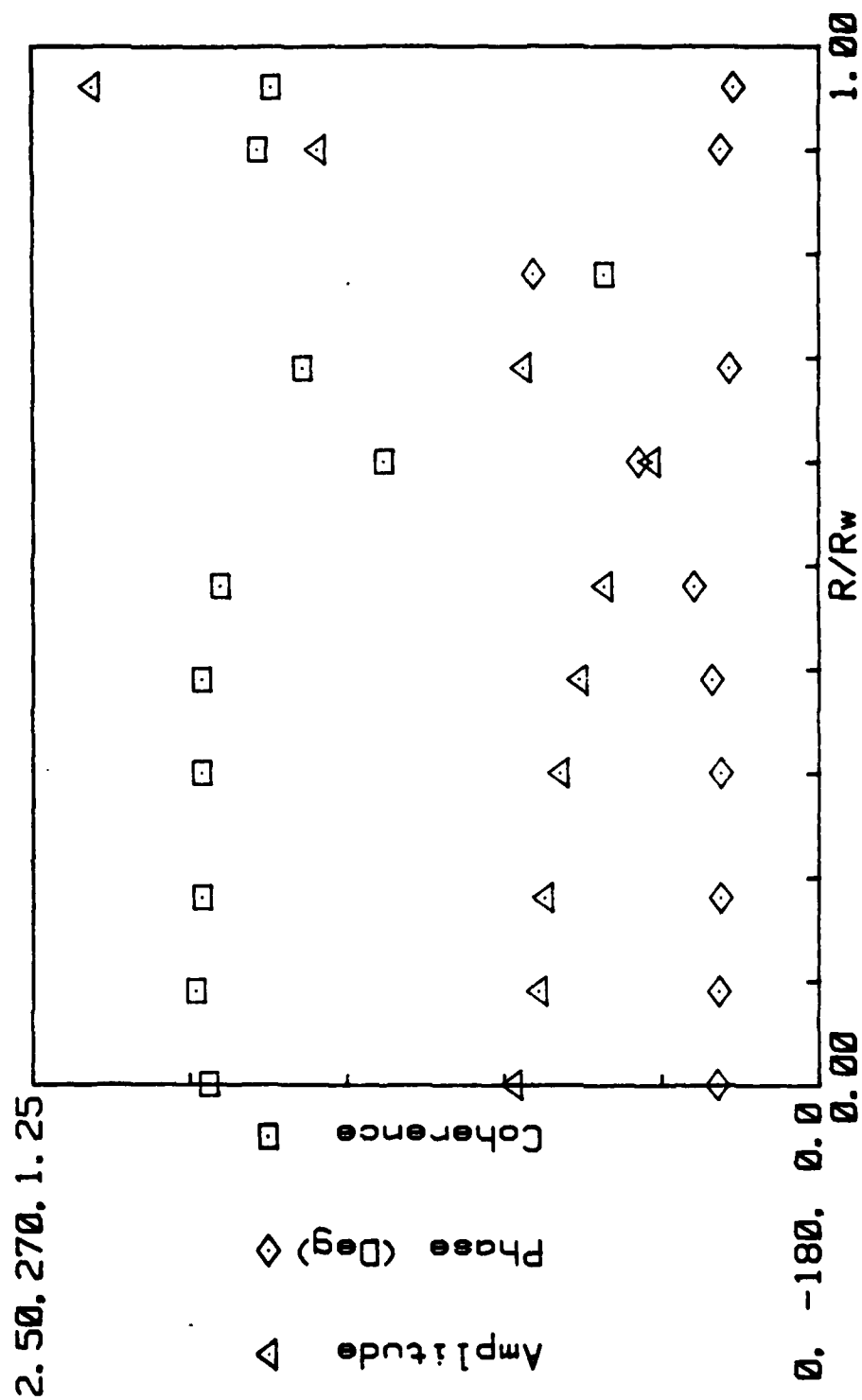


Figure 52.

NORMALIZED ACOUSTIC VELOCITY PROFILE

$Z/D = 4.22$ Freq = $170.00 \text{ A/Ac} = 1.10 \times \text{Max10f3} = 1.00$

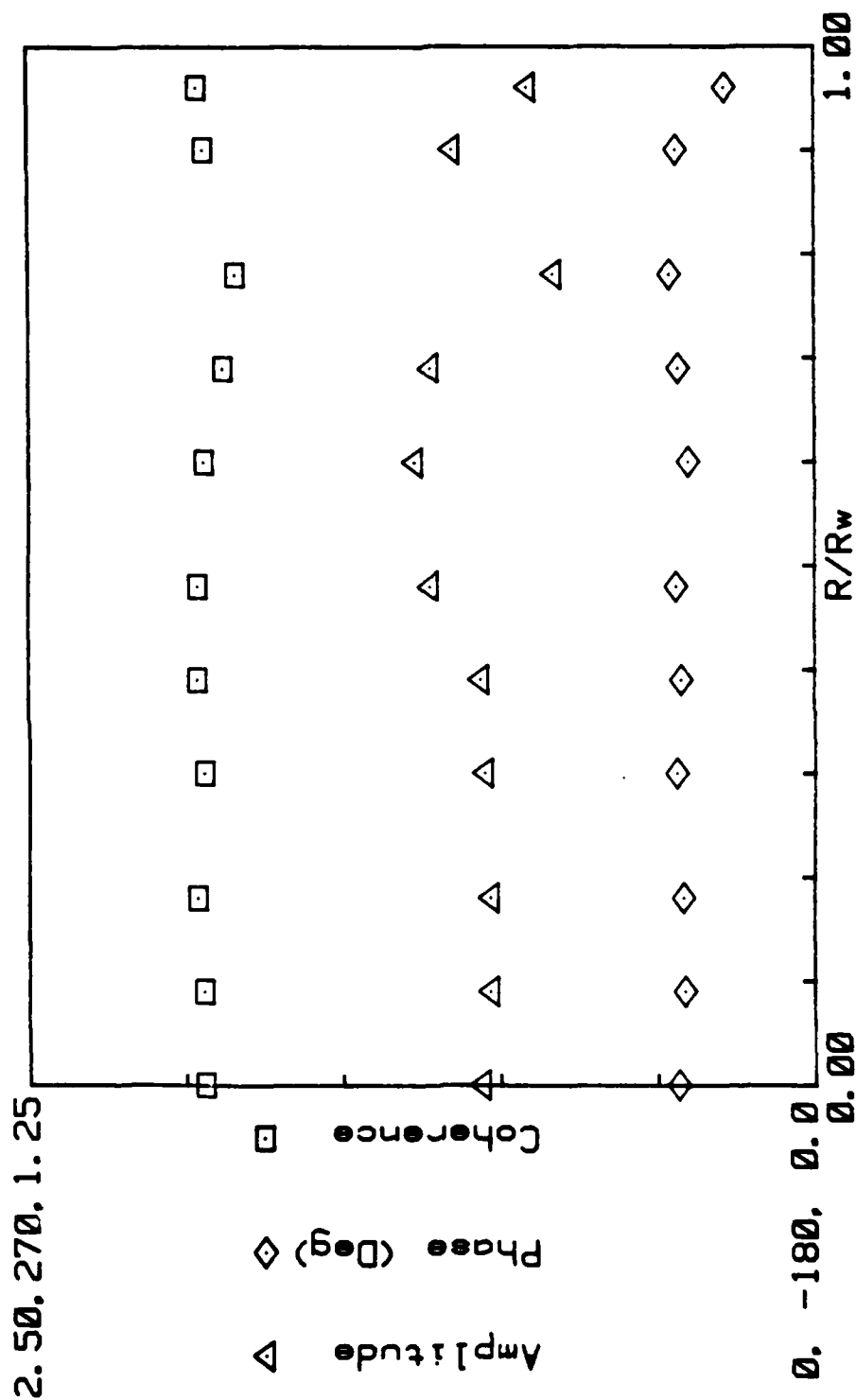


Figure 53.

NORMALIZED ACOUSTIC VELOCITY PROFILE

$Z/D = 4.22$ Freq = $84.00 \text{ A/At} = 5.60 \times 10^3 = 1.00$

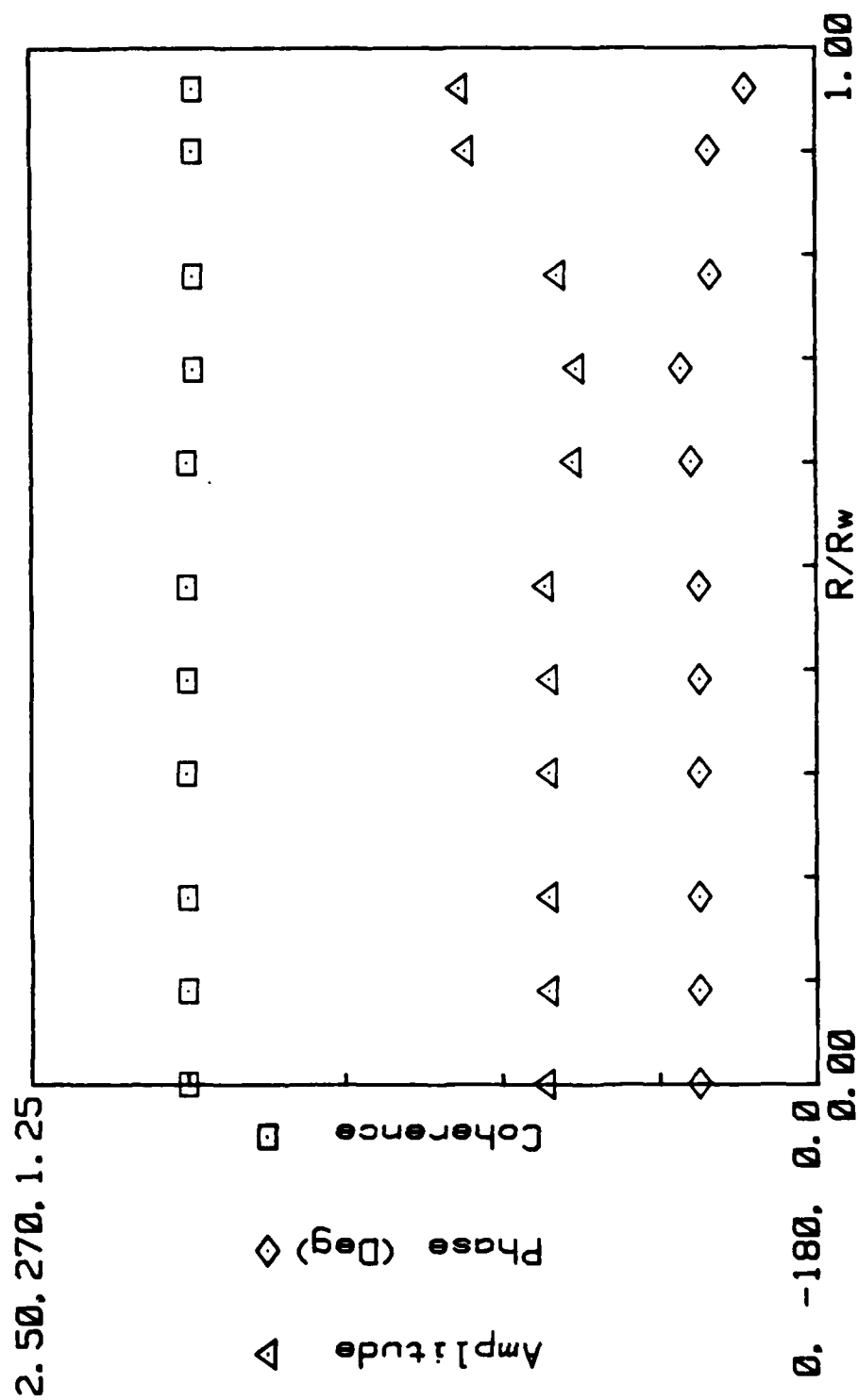


Figure 54.

NORMALIZED ACOUSTIC VELOCITY PROFILE

Z/D = 4.22 Freq = 170.00 A/Lt = 5.60 λ Max1013 = 1.00

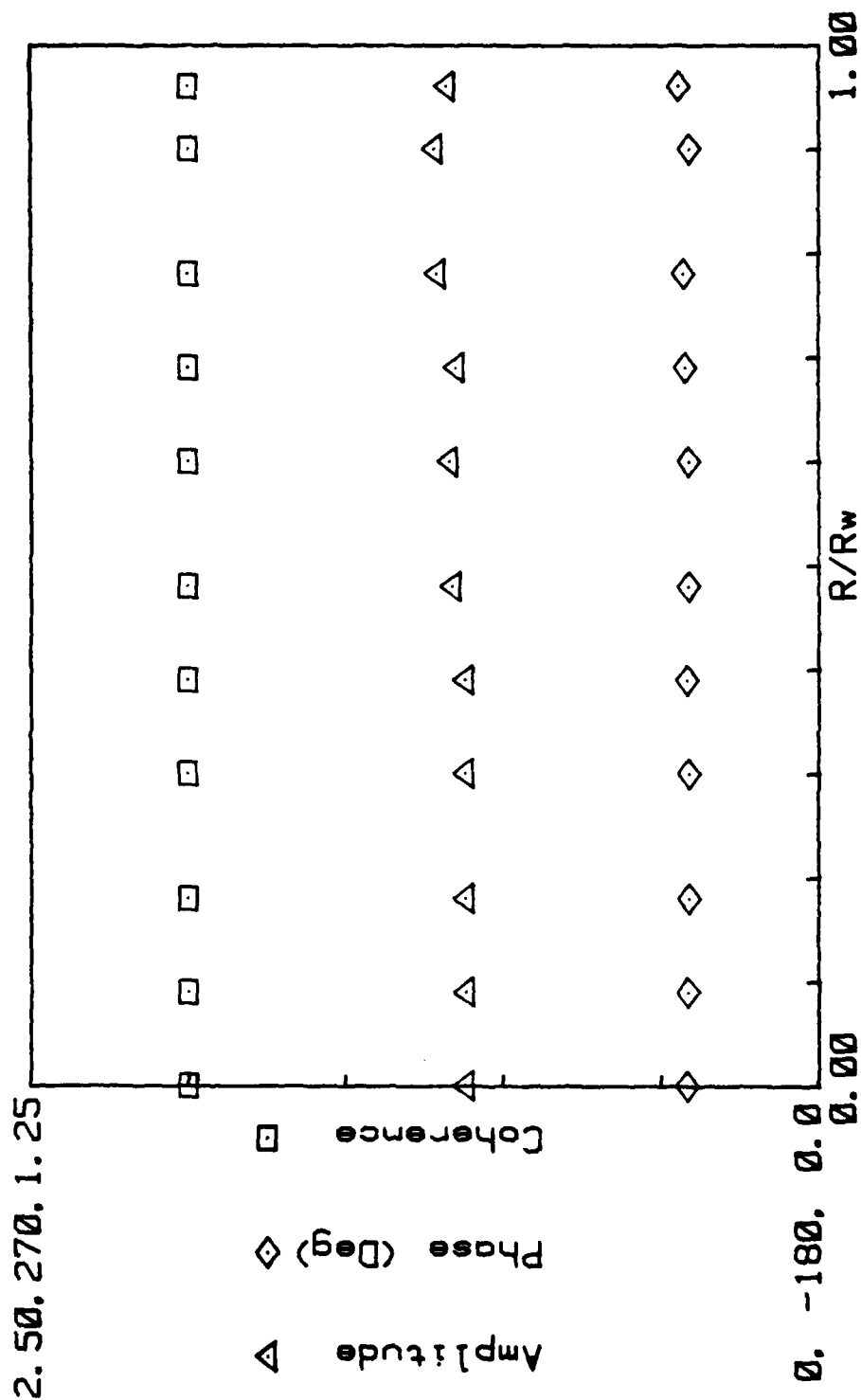
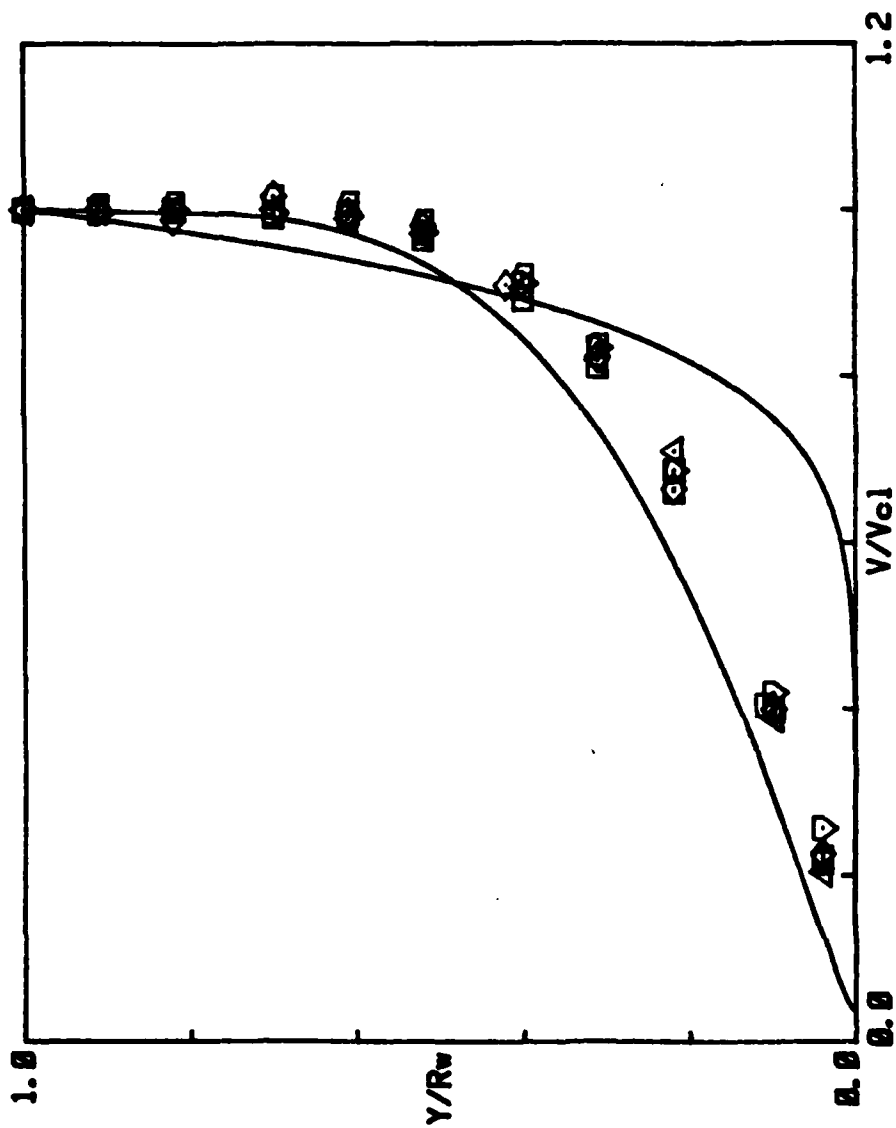


Figure 55.

MEAN VELOCITY PROFILE



$Z/D = 4.22$

$M_0 = 0.000960$

SYM	$A/\Delta t \times$	F Hz.
∇	0.00	0
\square	1.10	84
\diamond	1.10	170
\triangle	5.90	84
\square	5.90	170

Figure 56.

TURBULENCE INTENSITY PROFILE

Z/D = 11.50 Freq = 84.00 Hz. A/A_t = 1.10 x Max10f3 = 1.00

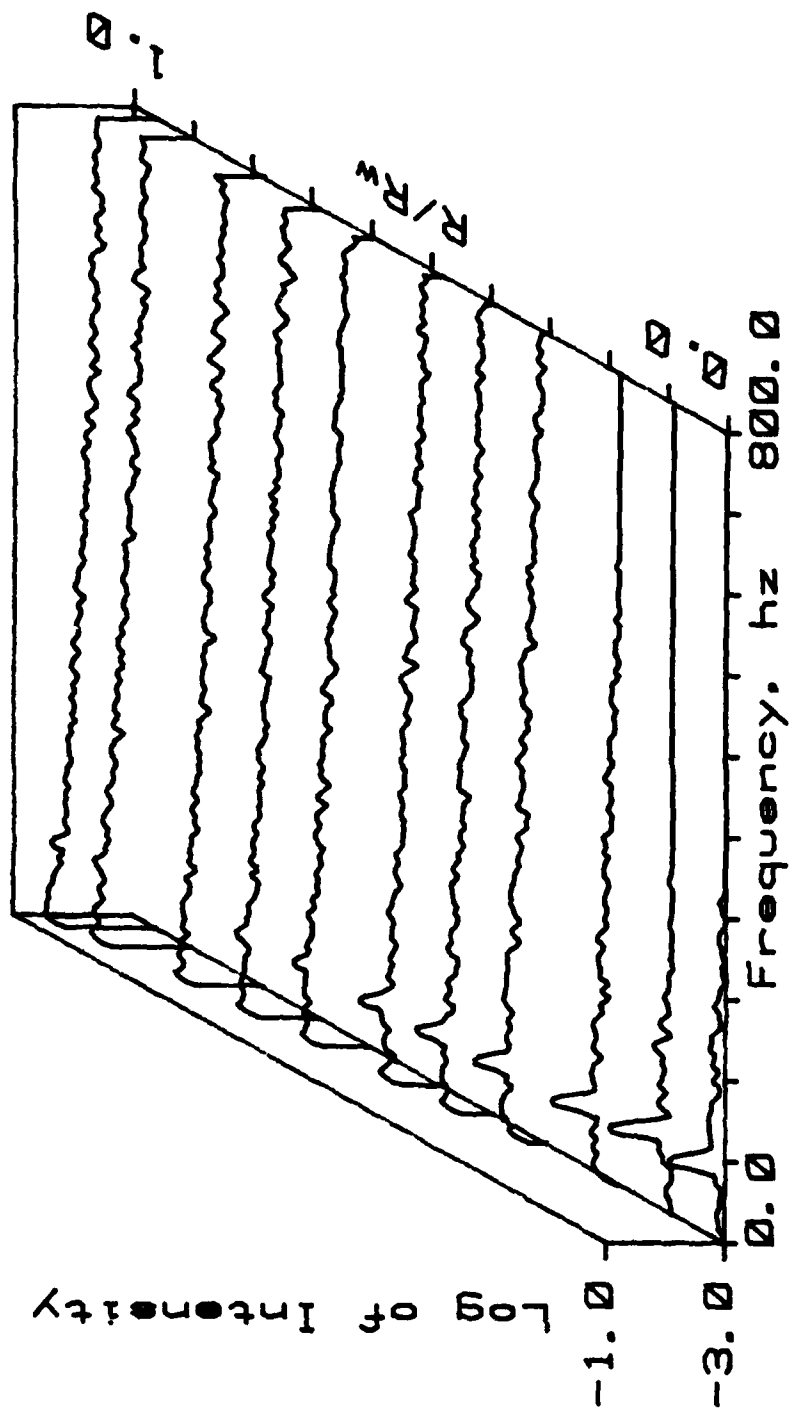


Figure 57.

TURBULENCE INTENSITY PROFILE

Z/D = 11.50 Freq = 170.00 Hz. $\lambda/\lambda_c = 1.10 \times$ $M \times 10^3 = 1.00$

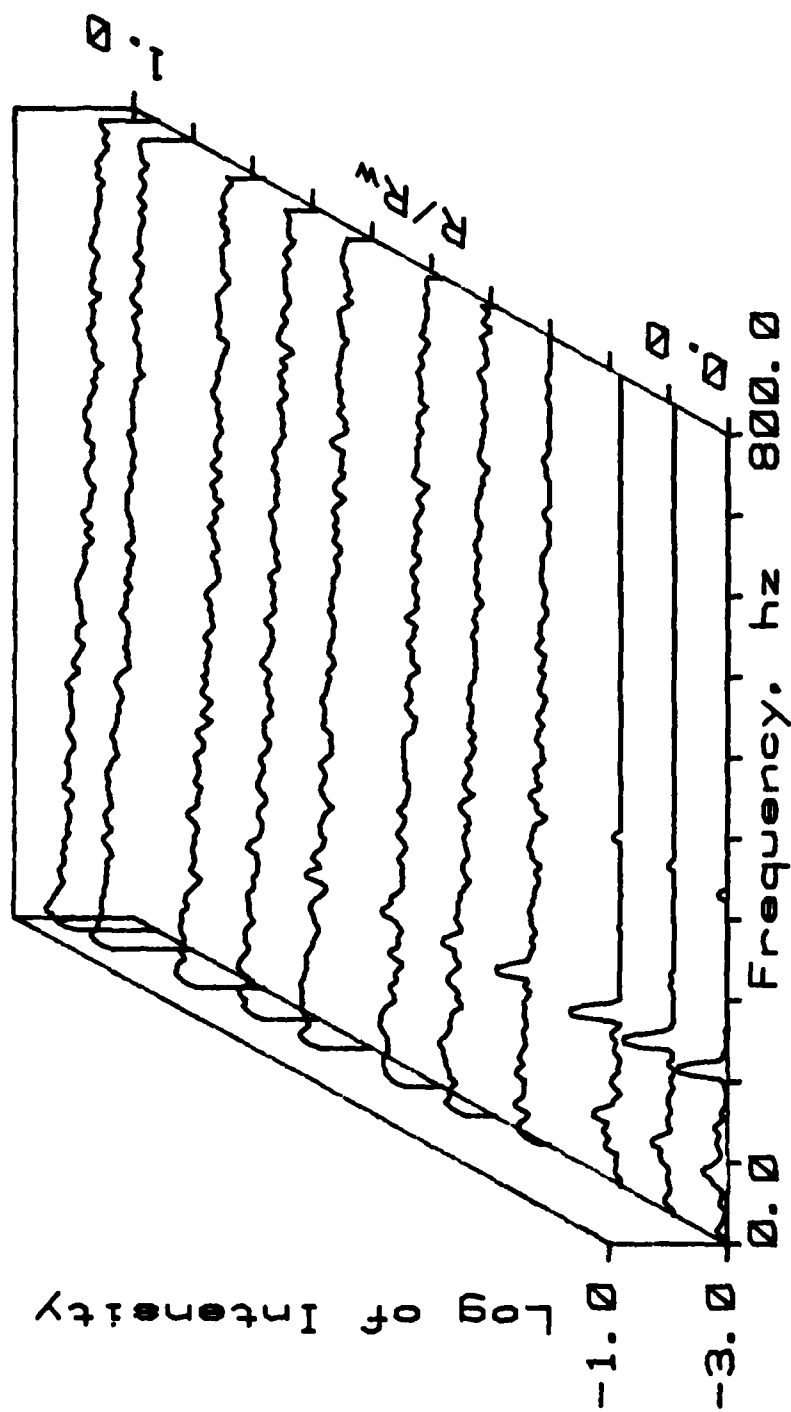


Figure 58.

TURBULENCE INTENSITY PROFILE

Z/D = 11.50 Freq = 84.00 Hz. $\Delta/\Delta t = 5.60 \times 10^{-3}$ Max10t3 = 1.00

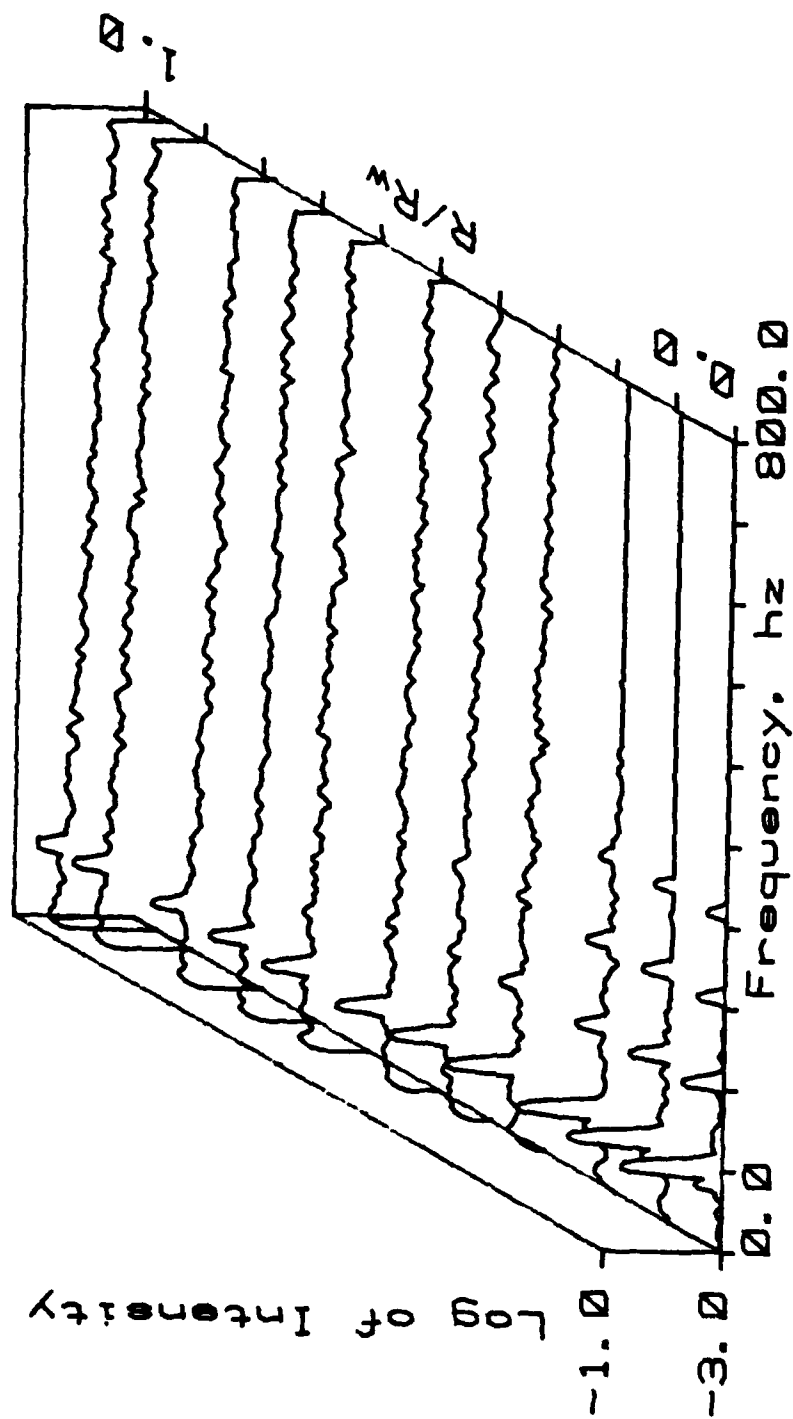


Figure 59.

TURBULENCE INTENSITY PROFILE

Z/D = 11.50 Freq = 170.00 Hz. A/A_t = 5.60 x Max10t3 = 1.00

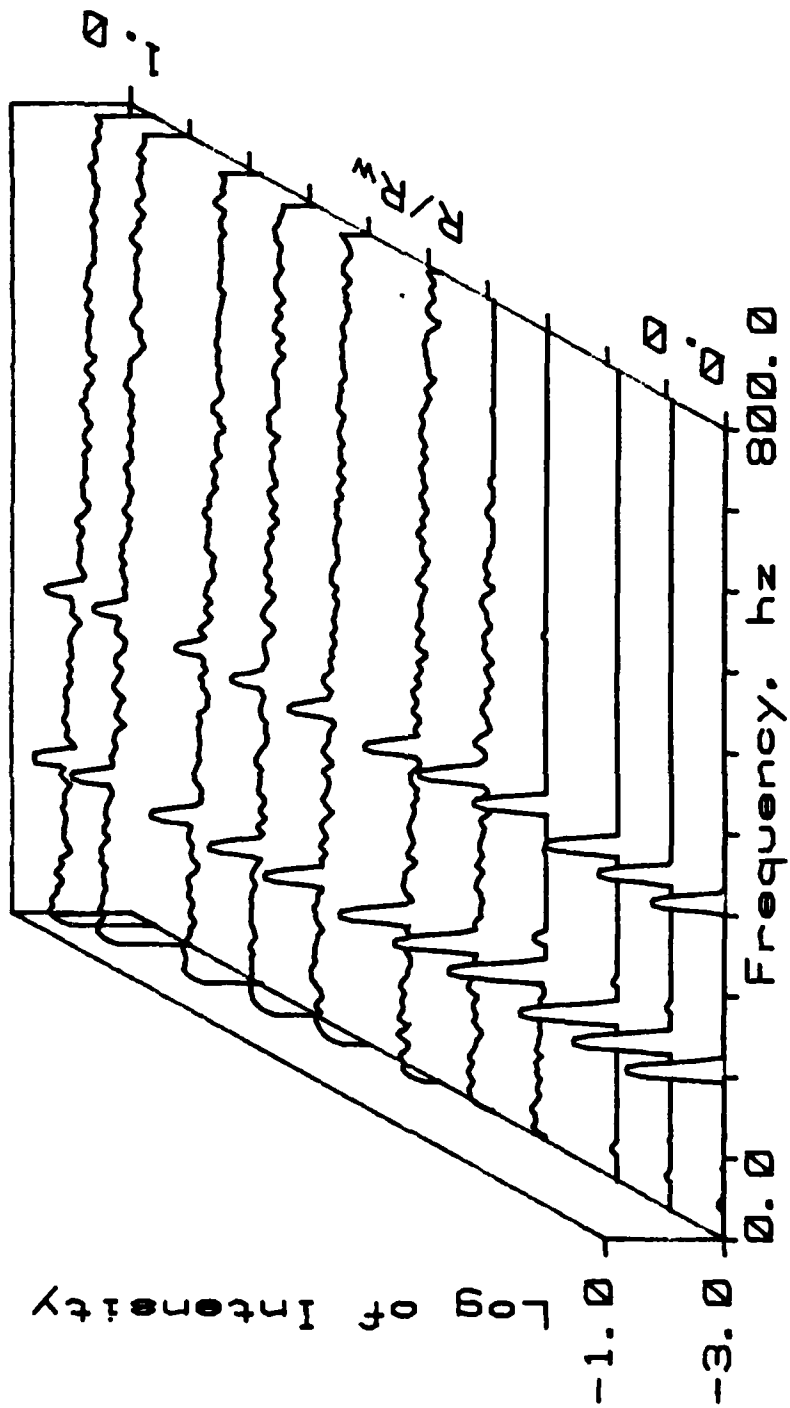


Figure 60.

TURBULENCE INTENSITY PROFILE

Z/D = 11.50 Freq = 0.00 Hz. $\Delta/\Delta t = 0.00 \times$ $\text{Max}10^{13} = 0.96$

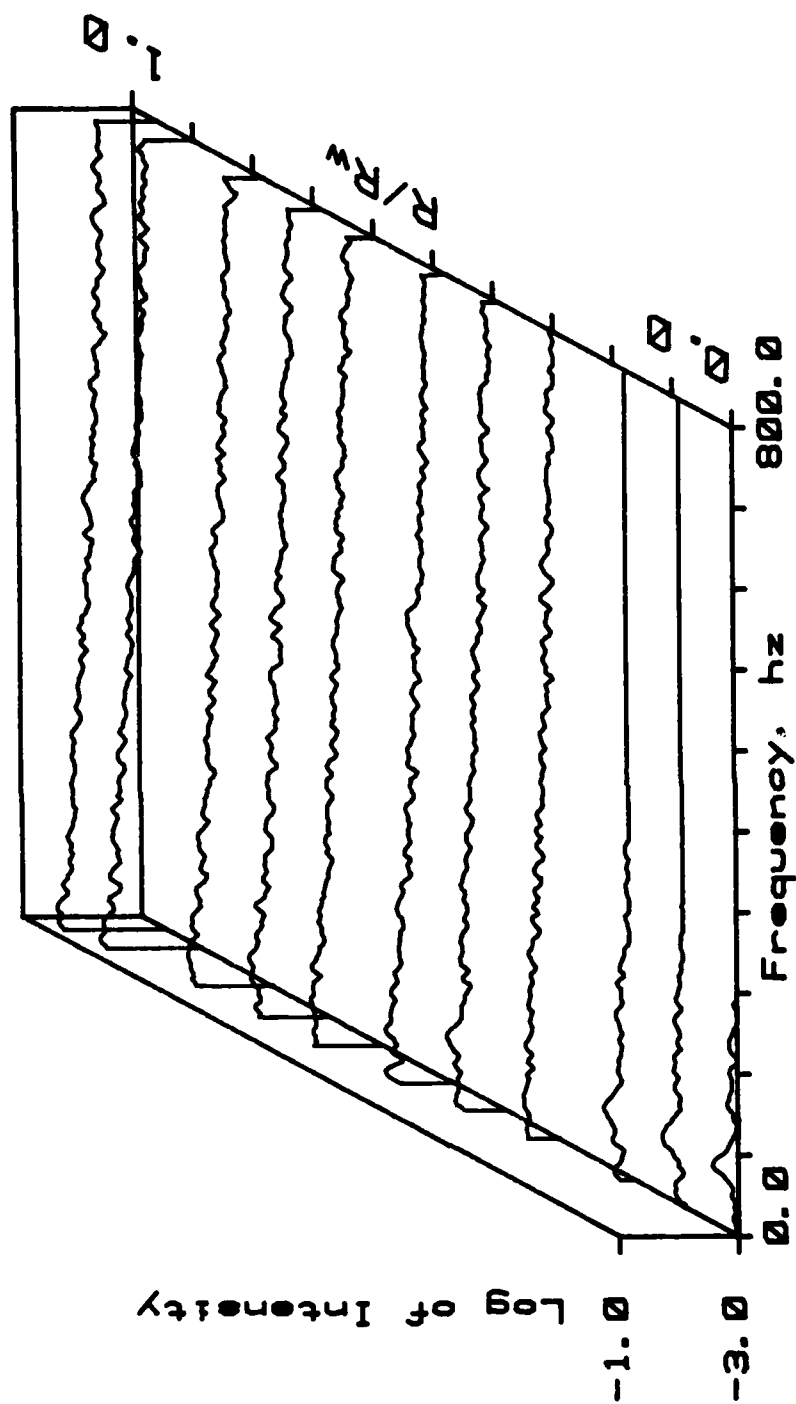


Figure 61.

NORMALIZED ACOUSTIC VELOCITY PROFILE

Z/D = 11.58 Freq = 84.88 A/At = 1.18 X Max18f3 = 1.00

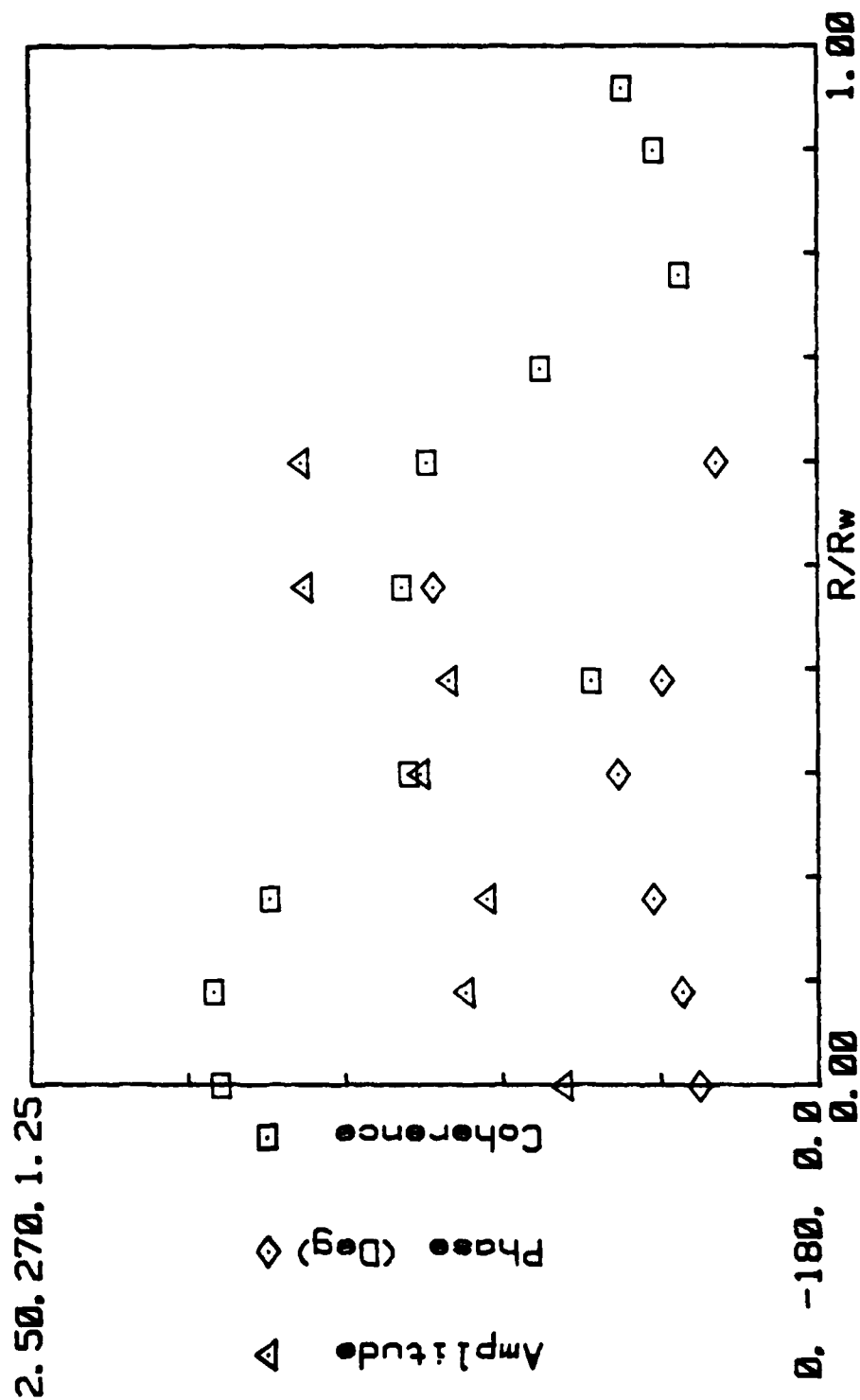


Figure 62.

NORMALIZED ACOUSTIC VELOCITY PROFILE

Z/D = 11.50 Freq = 170.00 A/Ac = 1.10 X Max10f3 = 1.00

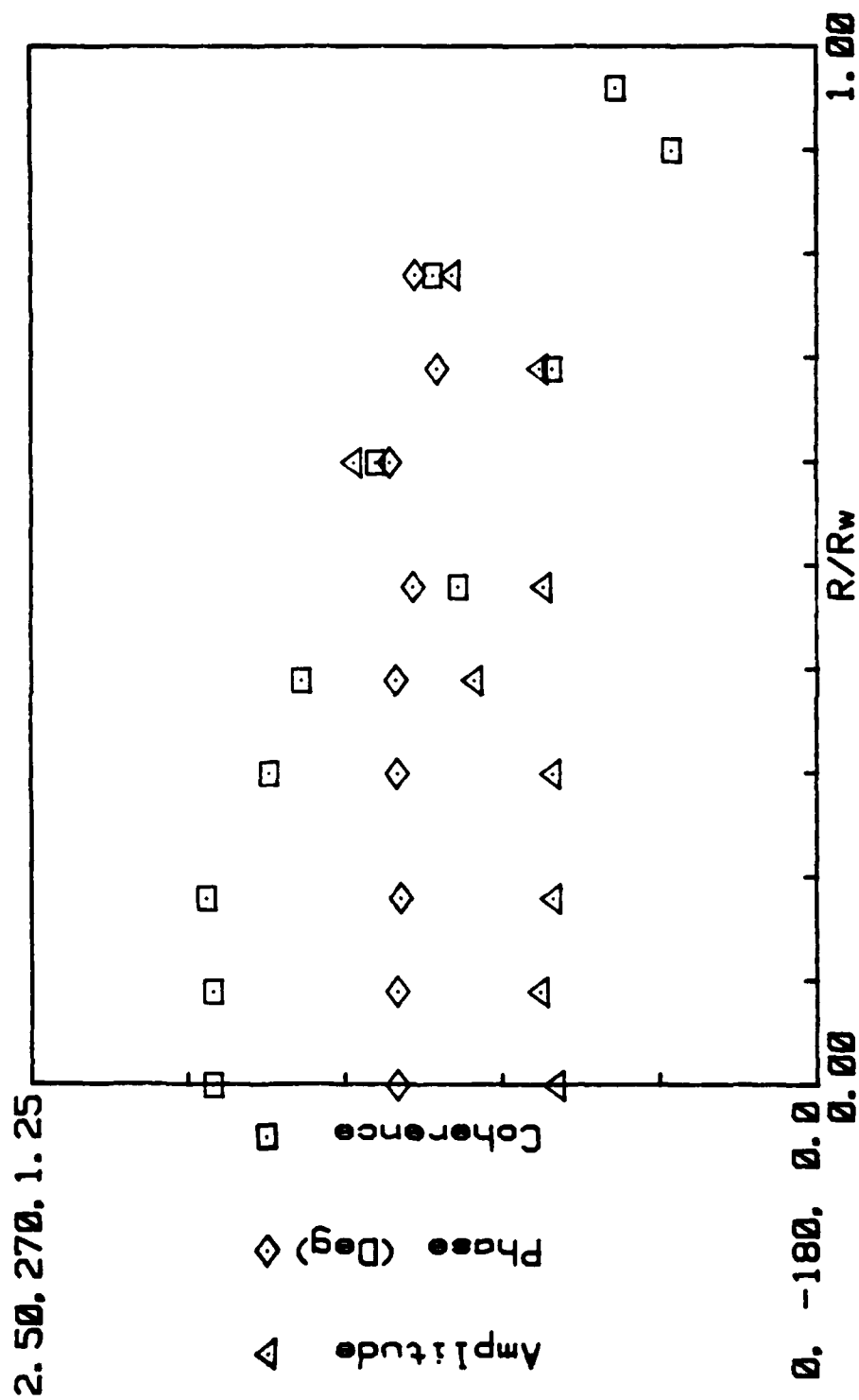


Figure 63.

NORMALIZED ACOUSTIC VELOCITY PROFILE

Z/D = 11.50 Freq = 84.00 $\Delta/\Delta t = 5.60 \times 10^{-3} = 1.00$

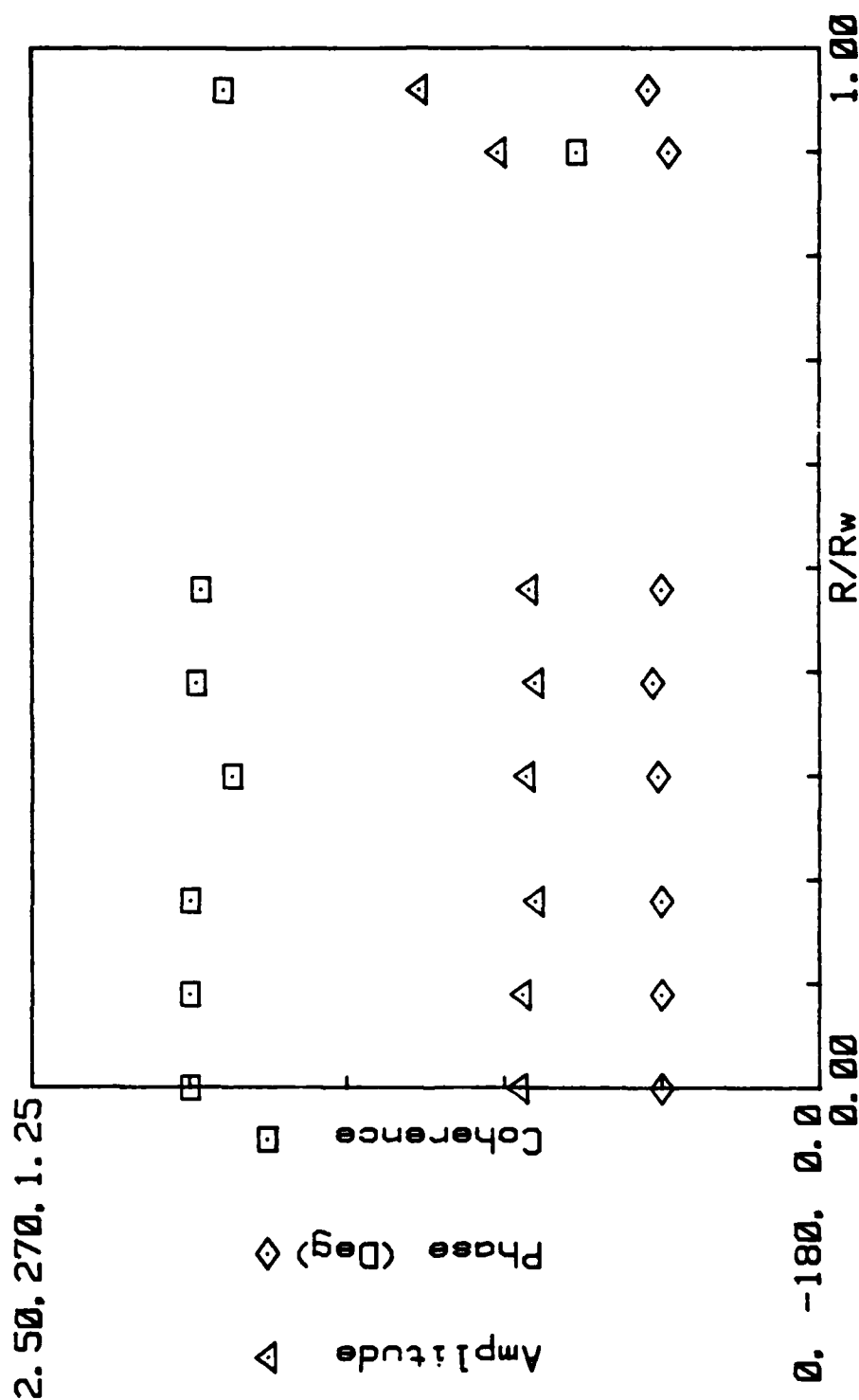


Figure 64.

NORMALIZED ACOUSTIC VELOCITY PROFILE

Z/D = 11.50 Freq = 170.00 A/Ac = 5.60 x Max10t3 = 1.00

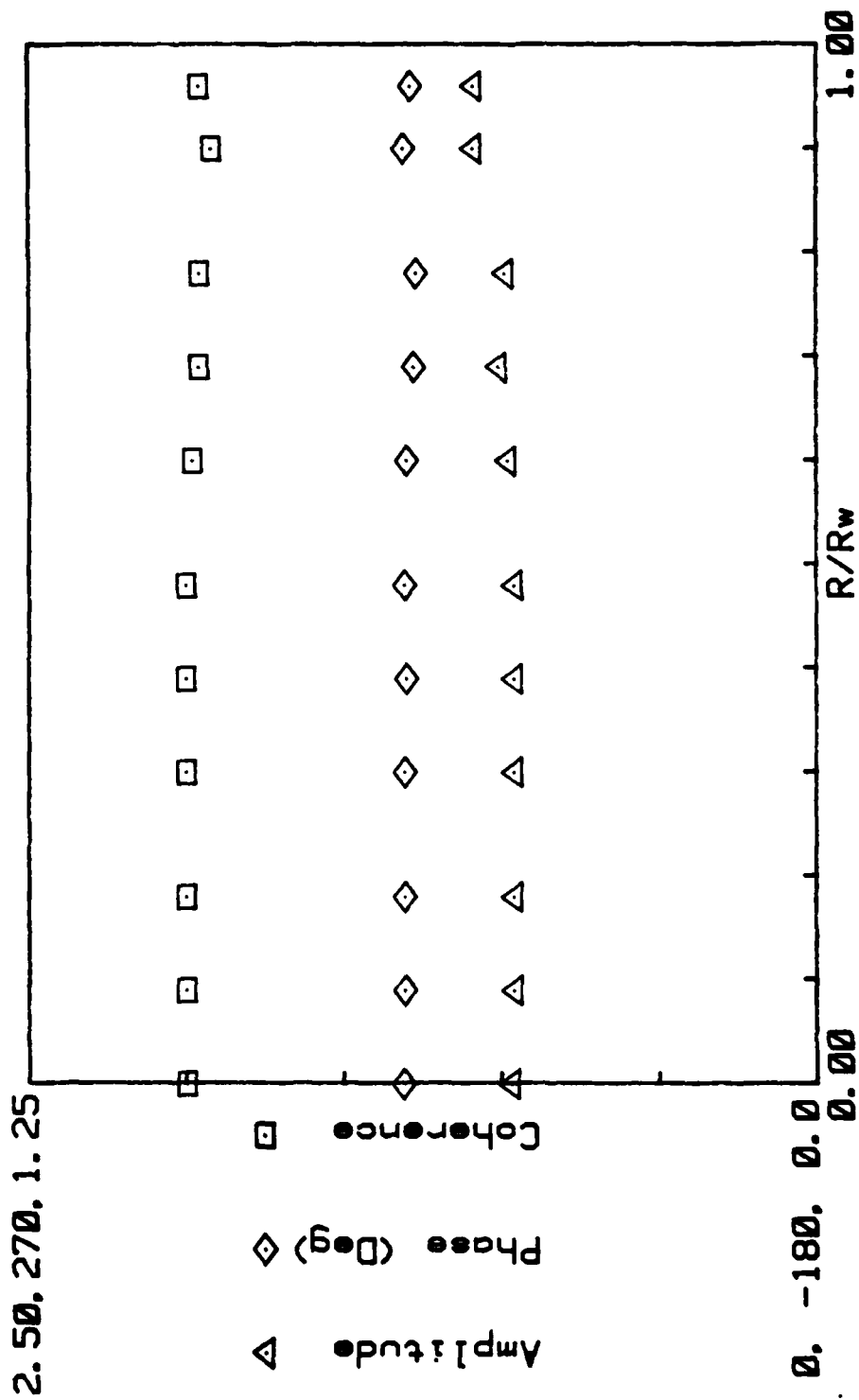


Figure 65.

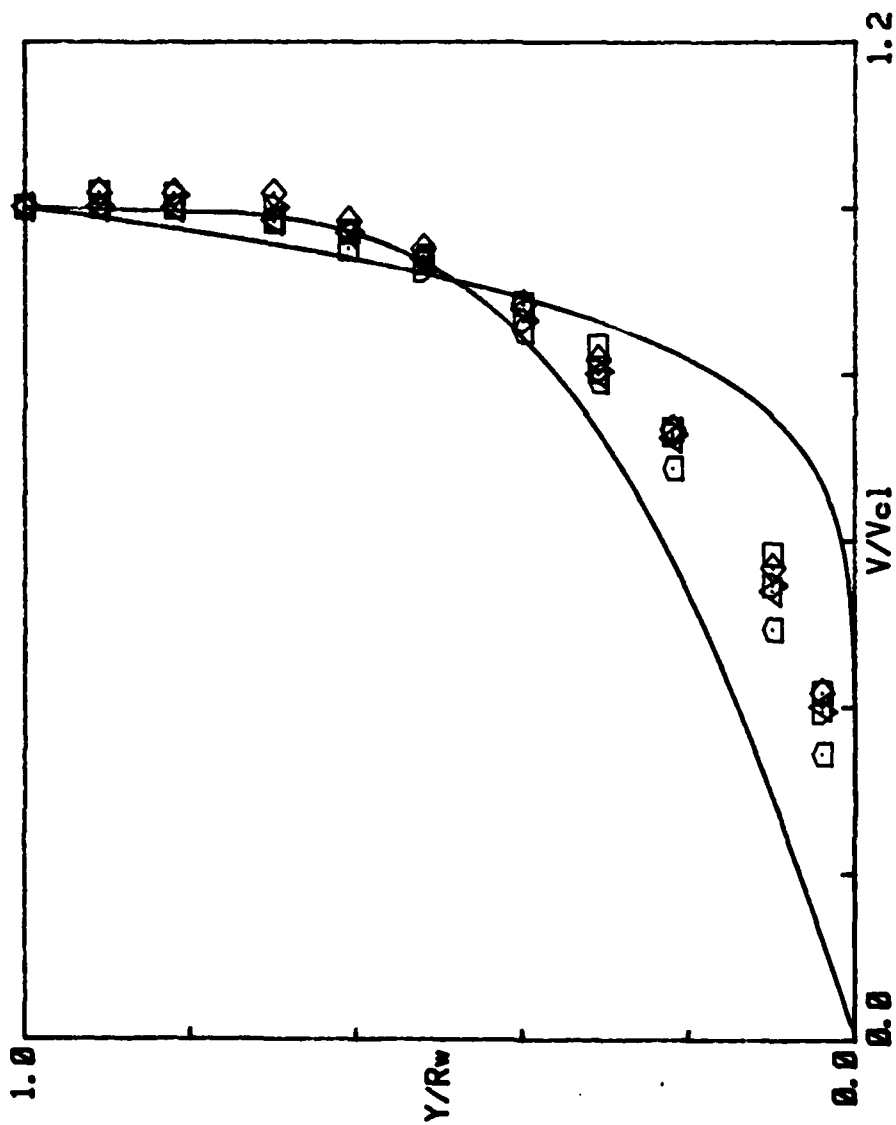
at the lower frequency, but extends to the wall at the higher frequency. The corresponding heat transfer spectra show the same behavior. From the acoustics viewpoint, the core flow region indicates planar wave behavior (i.e. constant amplitude, phase and coherence across the radius) except for the low frequency and low driving amplitude condition.

Figure 66 shows that velocity profile is considerable flatter than the BTC profile. However, the flow has not transitioned to fully developed turbulent flow, and is not influenced by the acoustic wave content of the flow. This indicates that the flow nonlinearities are small compared to the mean flow.

Appendix C contains the data obtained at this axial station at the higher surface Mach number with both the baseline and reduced wall damping. While there are quantitative differences, the overall qualitative behavior is similar to the data shown in figures 57 through 66. Measurements were also made at $Z/D = 6.64$ and $Z/D = 17.5$. Again there are quantitative differences but the overall qualitative pictures of the flow field is consistent with the pictures described above.

The axial distribution of the amplitude and phase of the centerline acoustic velocity (referenced to the head-end acoustic pressure) were then compared to one-dimensional predictions. To account for the significant effect of the wall damping, the predicted amplitude and phase of the acoustic velocity were estimated at each axial location using the Kummer's Function solution to the acoustic equations (18). Tables II through IV compare the predicted and observed acoustic velocities for each of the three basic flow conditions. At the lower surface Mach number, Table II shows reasonable agreement between the predicted and observed amplitudes at both frequencies.

MEAN VELOCITY PROFILE



$Z/D = 11.50$

$M_0 = 0.000960$

SYN $A/\Delta t$ F Hz.

▽	0.00	0
□	1.10	84
◇	1.10	170
△	5.90	84
□	5.90	170

Figure 66.

Table II.

Comparison of Predicted and Observed Acoustic Velocity
(Surface Mach No. = 0.001, Baseline Damping)

Axial Station (Z/D)	Frequency, 84 Hz				Frequency, 170 Hz							
	Amplitude		Phase, deg.		Amplitude		Phase, deg.					
	Pred. 1.1%	Observed 5.9%	Pred. 1.1%	Observed 5.9%	Pred. 1.1%	Observed 5.9%	Pred. 1.1%	Observed 5.9%				
1.8	0.42	0.47	0.41	-101	-118	-120	0.73	0.58	0.69	-102	-108	-112
4.22	0.91	0.97	0.86	-99	-122	-113	1.16	1.06	1.12	-95	-102	-105
6.64	1.20	-	1.09	-95	-	-116	0.75	0.89	0.95	-69	-91	-90
11.5	0.95	0.81	0.95	-77	-112	-77	1.31	0.83	0.97	80	60	56
17.6	0.79	0.83	0.79	50	-16	-1	1.25	-	1.24	-140	-	151

Table III.

Comparison of Predicted and Observed Acoustic Velocity
(Surface Mach No. = 0.0018, Baseline Damping)

Axial Station (Z/D)	Frequency, 84 Hz				Frequency, 180 Hz							
	Amplitude		Phase, deg.		Amplitude		Phase, deg.					
	Pred. 1.1%	Observed 5.9%	Pred. 1.1%	Observed 5.9%	Pred. 1.1%	Observed 5.9%	Pred. 1.1%	Observed 5.9%				
1.8	0.46	0.42	0.37	-110	-123	-118	0.72	0.64	0.59	-107	-111	-114
4.22	0.99	0.99	1.19	-106	-156	-118	1.17	1.07	1.02	-97	-111	-104
6.64	1.30	-	0.75	-100	-	-62	0.88	0.82	0.97	-65	-68	-81
11.5	1.13	1.72	1.02	-66	143	-90	1.50	0.65	0.86	75	82	63
17.6	1.33	-	0.77	+43	-	0	1.98	-	1.06	-145	-	155

Table IV.

Comparison of Predicted and Observed Acoustic Velocity
(Surface Mach No. = 0.0018, Baseline Damping)

Axial Station (Z/D)	Frequency, 65 Hz				Frequency, 135 Hz							
	Amplitude		Phase, deg.		Amplitude		Phase, deg.					
	Pred.	Observed 0.6% 3.3%	Pred.	Observed 0.6% 3.3%	Pred.	Observed 0.6% 3.3%	Pred.	Observed 0.6% 3.3%				
1.8	0.30	0.32	0.29	-97	-106	-111	0.58	0.54	0.53	-97	-116	-109
4.22	0.67	0.29	0.49	-95	-105	-130	1.08	0.90	0.91	-94	-110	-102
6.64	0.96	0.7	0.52	-93	-67	-106	1.05	0.31	0.88	-85	-141	-93
11.5	1.17	1.21	0.94	-85	-83	-103	0.53	0.97	0.47	53	-86	31

The phase angle comparisons also show reasonable agreement; the one significant disagreement being at $Z/D = 17.6$. In addition, the magnitude of the acoustic driving also has little effect as expected in a linear system.

Table III shows a similar comparison for the higher surface Mach number and baseline damping. Here, both amplitude and phase comparisons show reasonable agreement at the first two axial stations for all flow conditions. For the two downstream locations, however, significant differences appear at all flow conditions. At $Z/D = 6.64$, the data at the higher frequency agree with the predictions reasonably well, but significant differences are observed at the lower frequency. Thus, surface Mach numbers appears to influence the acoustics at higher Z/D by some mechanism which is not properly incorporated in the acoustic model.

Table IV shows the comparisons for the higher surface Mach number flow with the reduced surface damping. Only the data at $Z/D = 1.8$ show good agreement with the predicted behavior at all flow conditions. At $Z/D = 4.22$, the higher frequency results compare favorably, but significant differences are observed at the lower frequency. Significant deviations are observed at $X/D = 6.44$ for all flow conditions. At $Z/D = 11.5$, reasonable agreement is then observed, except at the higher frequency and lower driving amplitude.

Stepping back and examining all three sets of data together, one dimensional acoustics seem to model the head-end behavior reasonably well for all flow conditions. For conditions near and downstream of the flow transition, these appear to be interactions between surface Mach number, frequency, and wall damping which produce significant deviations from one-dimensional behavior. Obviously, the model is deficient. One possible deficiency is the one

dimensional nature of in the model. It is also possible that all the operative mechanisms are not included in the model. For example, neither the effects of turbulence or wave refraction, as suggested by Hersh (22), are included. These two additional mechanisms also should be investigated in future analytical studies.

3.0 CONCLUSIONS

A number of significant conclusions can be drawn from the experimental results. First, and perhaps most important, the velocity coupling models used in combustion stability predictions are incorrect. In fact, stability predictions based on these models could lead to substantial errors in estimating motor stability behavior. Furthermore, these data suggest how these models can be corrected, as well as providing a basis for interpreting motor stability information.

Second, the hot wire anemometer measurements show the general properties of the flowfield are consistent with Beddini's flowfield model. Mean velocity and turbulence intensity profiles show reasonable agreement with the inviscid rotational solutions of the turbulent Navier-Stokes equations. Furthermore, imposing acoustic velocity oscillations on the flowfield has little effect on the mean velocity profile. However, there is an interaction between acoustic waves and the characteristic frequency of the initial breakdown of the inviscid flow. Also, turbulence intensities near the wall increase significantly at approximately the same axial station as transition in the mean velocity profile.

Third, there is a strong interaction between the acoustic velocity oscillations and the flowfield downstream of the transition of the mean flow. Specifically, the wall heat transfer does not respond to low amplitude (i.e., $< 0.1\%$) acoustic oscillations. It appears that the increased turbulence intensities damp out the acoustic velocity oscillations or the increased gradients in the mean velocity gradient refracts the acoustic wave away from the surface. The net effect is to confine the effect of the acoustic waves to the core region downstream of the flow transition. At higher acoustic

amplitudes however (i.e. $> 0.2\%$) the acoustic waves penetrate to the wall and influence the wall heat transfer.

Fourth, nonlinear effects in both the wall heat transfer and the flowfield first appear in the head end region, i.e. upstream of the flow transition. These nonlinearities are first observed in the flow near the wall but can penetrate to the centerline under some flow conditions. The detailed structure of these nonlinear flows require further study which will necessitate testing with multiple element anemometer.

AD-A151 081

COUPLING BETWEEN VELOCITY OSCILLATIONS AND SOLID
PROPELLANT COMBUSTION. (U) UNITED TECHNOLOGIES CORP
SUNNYVALE CA CHEMICAL SYSTEMS DIV R S BROWN ET AL.

2/2

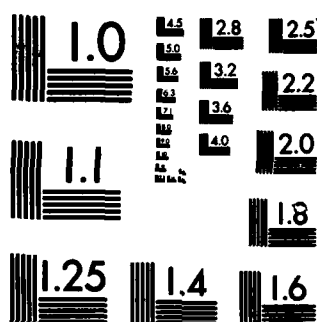
UNCLASSIFIED

AUG 84 CSD-2749-AR-3 AFOSR-TR-85-0100

F/G 21/8.2

NL

									END				
									FILED				
									DEC				



MICROCOPY RESOLUTION TEST CHART
NATIONAL BUREAU OF STANDARDS-1963-A

REFERENCES

1. Hart, R. W., J. F. Bird, R. H. Cantrell, and F. T. McClure, "Nonlinear Effects in Instability of Solid Propellant Rocket Motors," AIAA J., 2, 1964, pp. 1720-1273.
2. Price, E.W., "Axial Mode, Intermediate Frequency Combustion Instability in Solid Propellant Rocket Motors," AIAA Preprint 64-146, January 1964.
3. Crump, J.E., and E. W. Price, "Effects of Acoustic Environment on the Burning Rate of Solid Propellants," AIAA J., 7, 1964, pp. 1274-1278.
4. Nadaud, L., and M. Gicquel, "Effect of Sound Waves on the Burning Rate of Solid Propellants," La Recherche Aeronautique, No. 88, 1962, pp. 59-63.
5. Price, E.W., and G. L. Dehority, "Velocity Coupled Axial Mode Combustion Instability in Solid Propellant Rocket Motors," paper presented at ICRPG/Second AIAA Solid Propulsion Conference, Anaheim, CA, June 1967.
6. Dehority, G. L., and E. W. Price, "Axial Mode Intermediate Frequency Combustion Instability in Solid Propellant Rockets", NWC TP 5654, Naval Weapons Center, October 1974.
7. Culick, F. E. C., "Stability of Longitudinal Oscillation with Pressure and Velocity Coupling in a Solid Propellant Rocket," Comb. Sci. and Technology, 2, 1971, pp. 179-201.
8. Price, E.W., "Velocity Coupling in Oscillatory Combustion of Solid Propellants," AIAA J., 17, 1979, pp. 799-800.
9. Beddini, R. A., "Effects of Grain Port on Solid Propellant Erosive Burning", AIAA Preprint 78-977, 1978.
10. Dunlap, R., P. G. Willoughby, and R. W. Hermsen, "Flowfield in the Combustion Chamber of Solid Propellant Rocket Motor," AIAA J., 12, 1974, pp. 1440-1442.
11. Beddini, R.A., "Analysis of Injection-Induced Flows in Porous Ducts," Ph.D Thesis, Rutgers University, October 1981.
12. Berman, A.S., "Laminar Flow in Channels with Porous Walls," J. Applied Physics, 24, 1953, pp. 1232-1235.
13. Culick, F.E.C., "Rotational Axisymmetric Mean Flow and Damping of Acoustic Waves in Solid Propellant Motors," AIAA Journal, 4, 1966 pp. 1462-1464.
14. Dunlap, R., P. G. Willoughby and S. W. Young, "Cold Flow Studies Test Report," CSD 4901-79-135, United Technologies, Chemical Systems Division, March 1980.

15. Brown, R.S., et al., "Vortex Shedding Studies," AFRPL-TR-80-13, Contract No. FO4611-77-C-0060, United Technologies, Chemical Systems Division, April 1980.
16. Brown, R.S., P. G. Willoughby, and R. Dunlap, "Coupling Between Velocity Oscillations and Solid Propellant Combustion," CSD Report 2749-AR-2, Chemical Systems Division, June 1983. See also AIAA Report 84-0288, 1984.
17. Brown, R.S. and R. C. Waugh, "Coupling Between Velocity Oscillations and Solid Propellant Combustion," CSD Report 2749-AR-1, Chemical Systems Division, April 1982.
18. Brown, R.S., R. C. Waugh, and V. L. Kelly, "Rotating Valve for Velocity Coupled Combustion Response Measurements," J. Spacecrafts and Rockets, 19, No. 5, 1982, pp. 437-444.
19. Flandro, G.A., "Nonlinear Time-Dependent Combustion of a Solid Propellant Rocket," paper presented at 19th JANNAF Combustion Meeting, Greenbelt, MD, 4-7 October 1982.
20. Ben Reuven, M., and M. Summerfield, "Analysis of Combustion Oscillations in Heterogeneous Systems," PCRL Report FR 82-004, June 1982, Princeton Combustion Research Labs.
21. Dunlap, R. and R. S. Brown, "Internal Flowfields Investigation," Report RDSR #4, Contract FO4611-83-C-0003, United Technologies/Chemical Systems Division, 1983.
22. Hersh, A.S., and B. Walker, "Experimental Investigation of Rocket Motor Flow-Turning Acoustic Losses," AFRPL-TR-84-009. Hersh Acoustical Engineering Inc., May 1984.

Appendix A

ACOUSTIC ADMITTANCE OF POROUS TUBING

The acoustic admittance of the solid propellant is an extremely important factor in determining the acoustic stability of the combustor. Likewise, the admittance of the porous tubing is important in interpreting acoustic measurements in the cold flow models. Therefore, independent research and development (IR&D) studies were conducted to evaluate the acoustic admittance (or, more precisely, the acoustic mass response function) of the porous tubes used in these models.

In the course of designing the Titan cold flow models (14,15), Dunlap developed a correlation between the pressure drop across and flow through the walls of porous tubes. This correlation has the form:

$$P_A^2 - P_W^2 = K (\dot{M})^{2-n} \quad (A-1)$$

where

P_A = the upstream pressure

P_W = the downstream pressure

K = the constant that depends on tubing wall thickness and porosity

\dot{M} = mass flow rate per unit area

n = a constant that depends on the type of flow in the porous tubing.

Figure A-1 shows excellent agreement between equation (A-1) for one set of experimental data, the correlation coefficient being 99.8%.

Under acoustic conditions, the pressure on both sides of the tubing oscillates. Assuming quasi-steady flow through the tubes, the mass response function can be derived from equation (A-1) to be:

$$R = \left(\frac{2}{2-n} \right) \left\{ \left(\frac{\bar{P}_A}{\bar{P}_W} \right) \left(\frac{\hat{P}_A}{\bar{P}_W} \right) - 1 \right\} \sqrt{ \left(\frac{\bar{P}_A}{\bar{P}_W} \right)^2 - 1 } \quad (A-2)$$

where

R = the mass response function

$(-)$ = represents time average values

\wedge = represents oscillating components.

Thus, the response depends on the relative magnitude and phase between the oscillatory pressures on each side of the tube wall, as well as the mean pressure drop across the tube wall.

To check equation (A-2), experiments were run in the rotating valve with the setup shown schematically in figure A-2.

Excellent agreement between the observed and predicted values is shown in figures A-3. Equation (A-2) thus appears to be valid for estimating the acoustic response of the porous tubing.

One limitation, however, is that the oscillatory pressure on the high pressure side of the tubing is also required in addition to the downstream pressure which is usually measured. To obtain this pressure requires an additional measurement. Alternatively, one can assume that the cavity upstream of the tubing is fed through a sonic choke and behaves in the bulk mode.

This assumption provides another relation between the mass flow oscillation and the upstream pressure oscillation, namely,

$$V \frac{dp}{dt} = \frac{\dot{m}}{n} - \frac{P_A^2 - P_W^2}{K}^{1/(2-n)} \quad (A-3)$$

where V is the cavity volume.

Assuming sinusoidal oscillations, equation (A-3) can be linearized and combined with equation (A-2) to yield

$$R = \left(\frac{-2i\lambda}{(2-n)} \right) \left\{ \left(\frac{2}{2-n} \right) \left(\frac{\bar{P}_A}{\bar{P}_W} \right)^2 + i\lambda \left[\left(\frac{\bar{P}_A}{\bar{P}_W} \right)^2 - 1 \right] \right\}^{-1} \quad (A-4)$$

Note that the segmented design used in CSD's cold flow models prevents axial mode oscillations in the upstream cavities, and therefore the bulk mode assumption is appropriate to use for these models. The final step in applying this approach to the cold flow experiment is to measure the pressure drop as a function of mass flow for the actual porous tubes used in this apparatus used in the cold flow velocity coupling studies. Figure A-4 shows the data from this apparatus which further substantiates the use of equation A-1 to correlate the results.

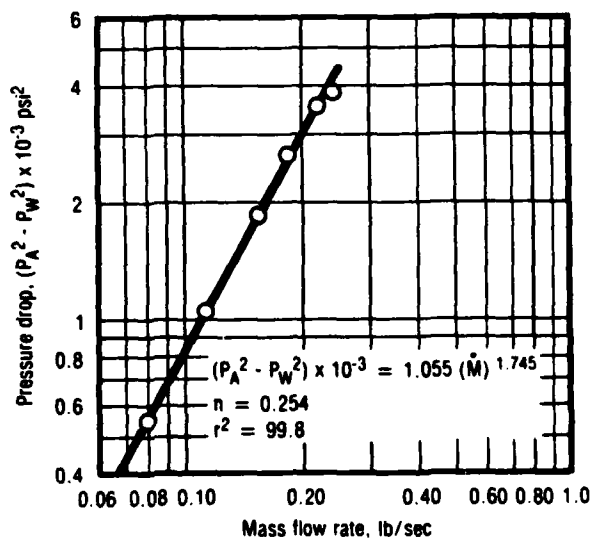


Figure A-1. Pressure Drop Correlation

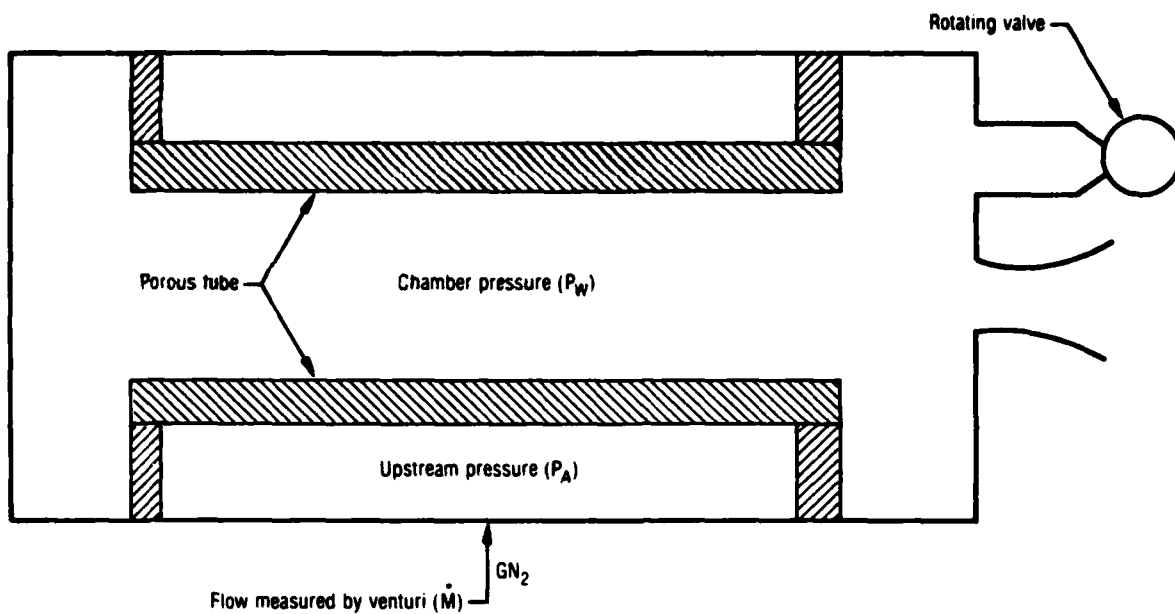


Figure A-2. Apparatus for Porous Tube Experiment

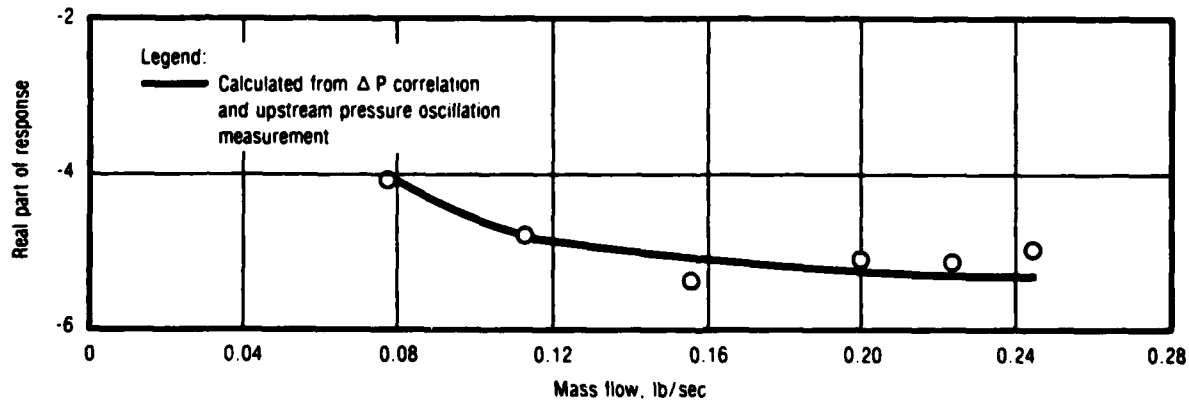


Figure A-3. Response Function of Porous Tubing

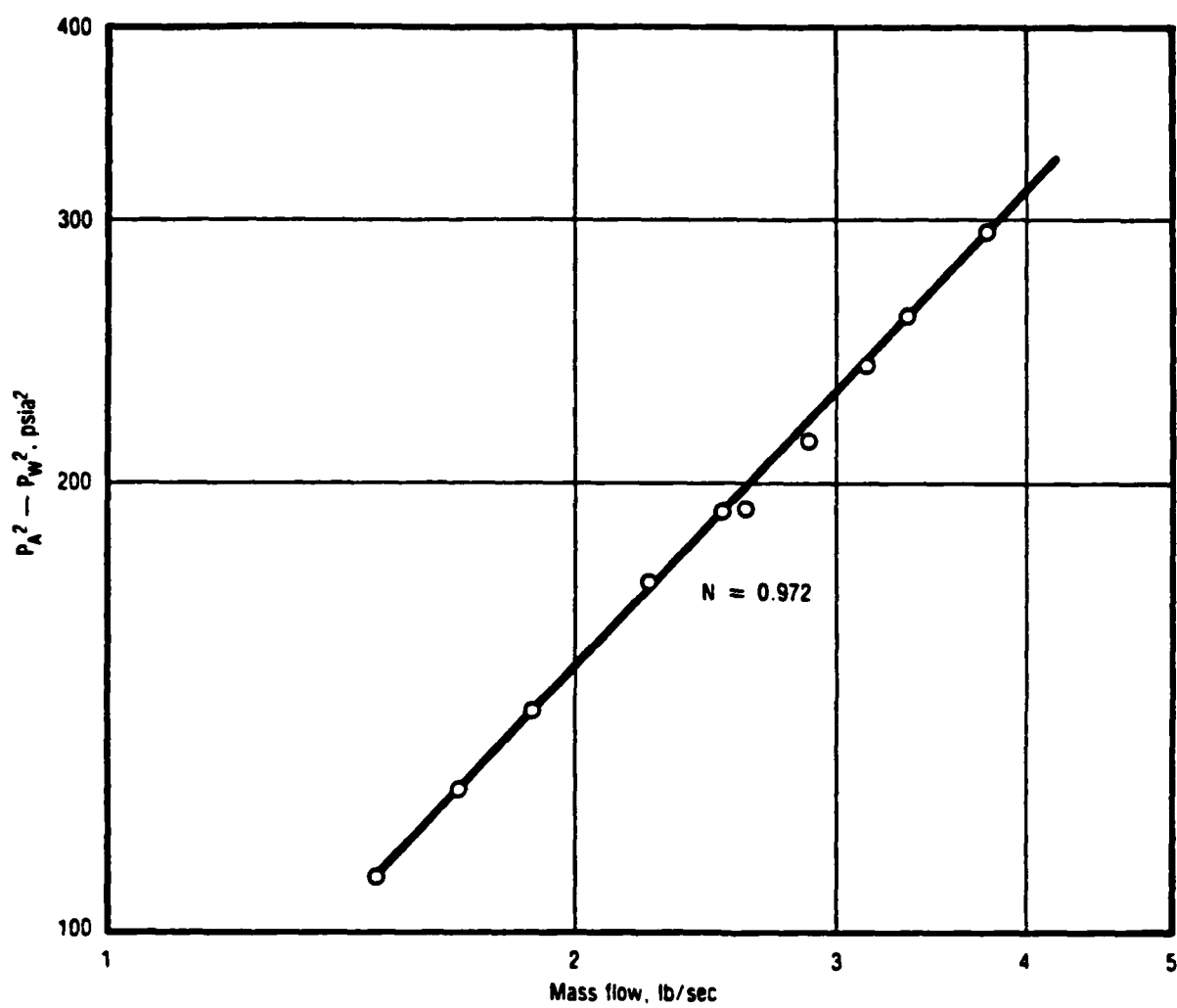


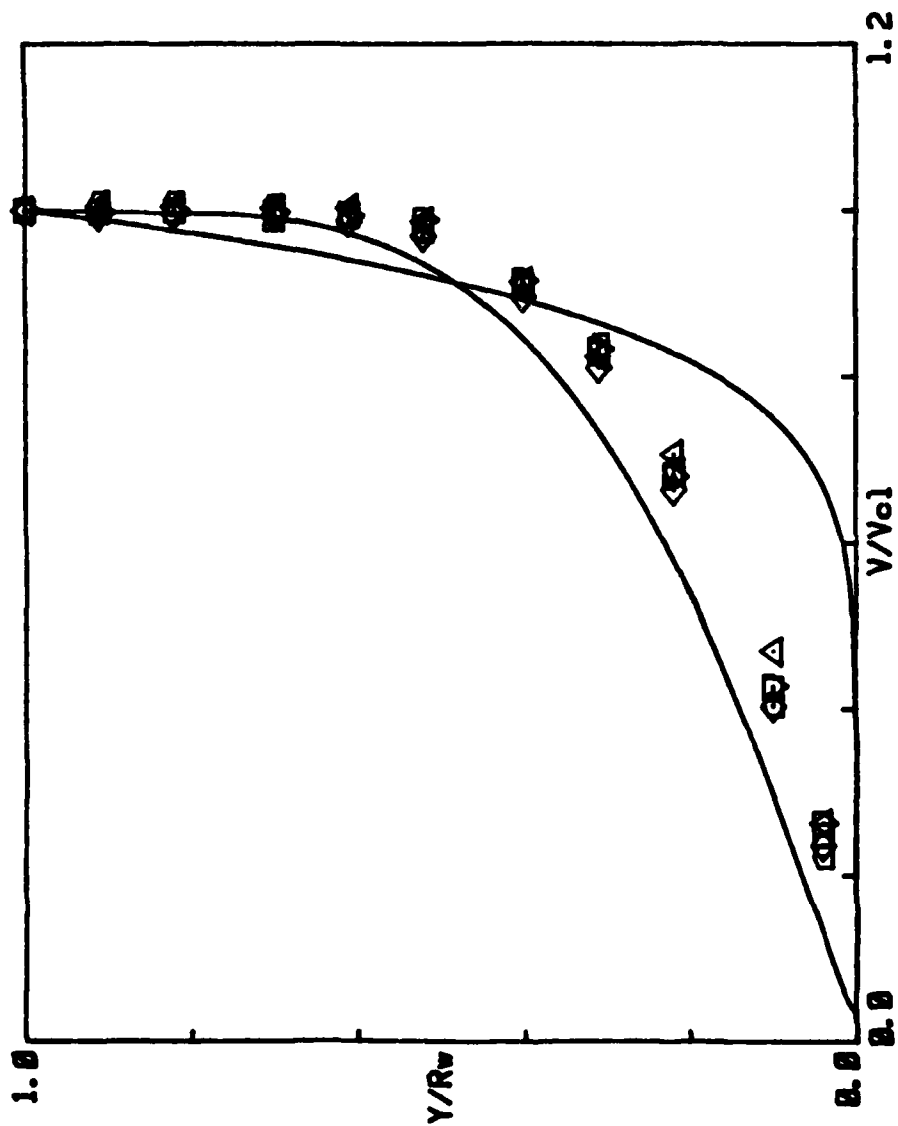
Figure A-4. Pressure Drop for Porous Tubes
31759

APPENDIX B

Additional Flowfield Data

at $Z/D = 4.22$

MEAN VELOCITY PROFILE



$Z/D = 4.22$

$Me = 0.001750$

SYM	A/Atz	F Hz.
▽	0.00	0
□	0.06	84
◇	0.60	170
△	3.30	84
□	3.30	170

Figure B-1.

TURBULENCE INTENSITY PROFILE

Z/D = 4.22 Freq = 0.00 Hz. A/A_t = 0.00 x Max10f3 = 1.00

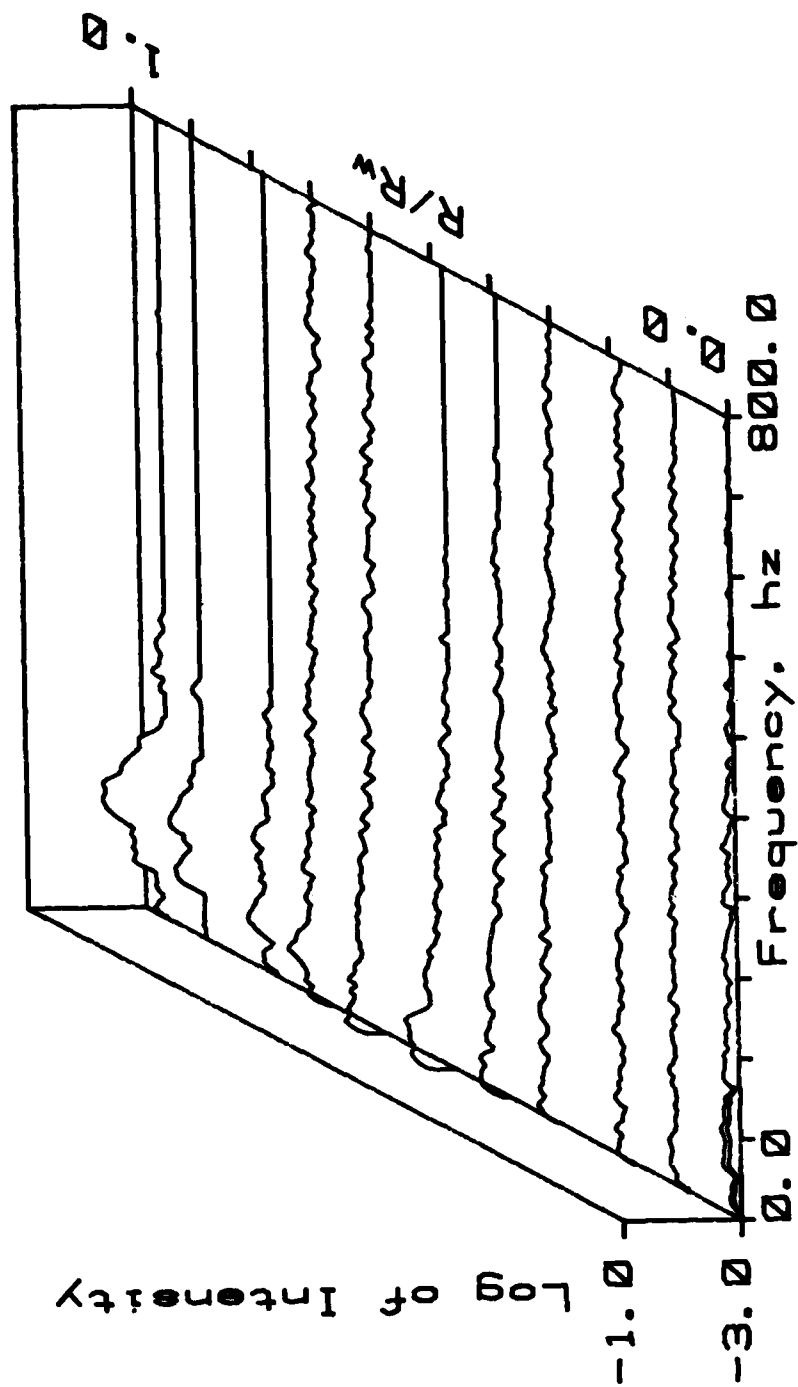


Figure B-2.

TURBULENCE INTENSITY PROFILE

Z/D = 4.22 Freq = 84.00 Hz. $\Delta/\Delta t = 0.60 \times 10^{-3}$ Max10t3 = 1.80

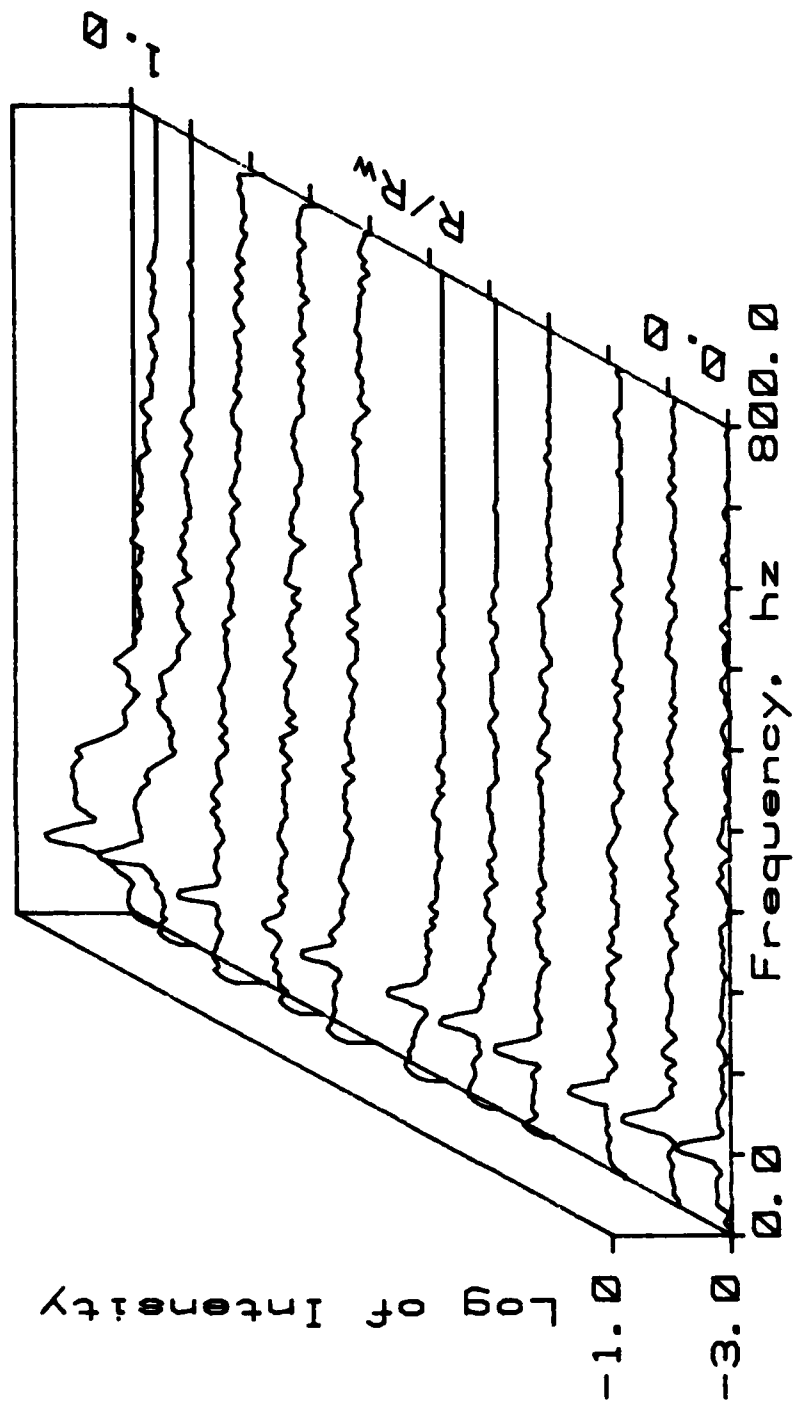


Figure B-3.

TURBULENCE INTENSITY PROFILE

Z/D = 4.22 Freq = 170.00 Hz. $\Delta/\Delta t = 0.60 \times 10^{-3}$ $M \times 10^{-3} = 1.80$

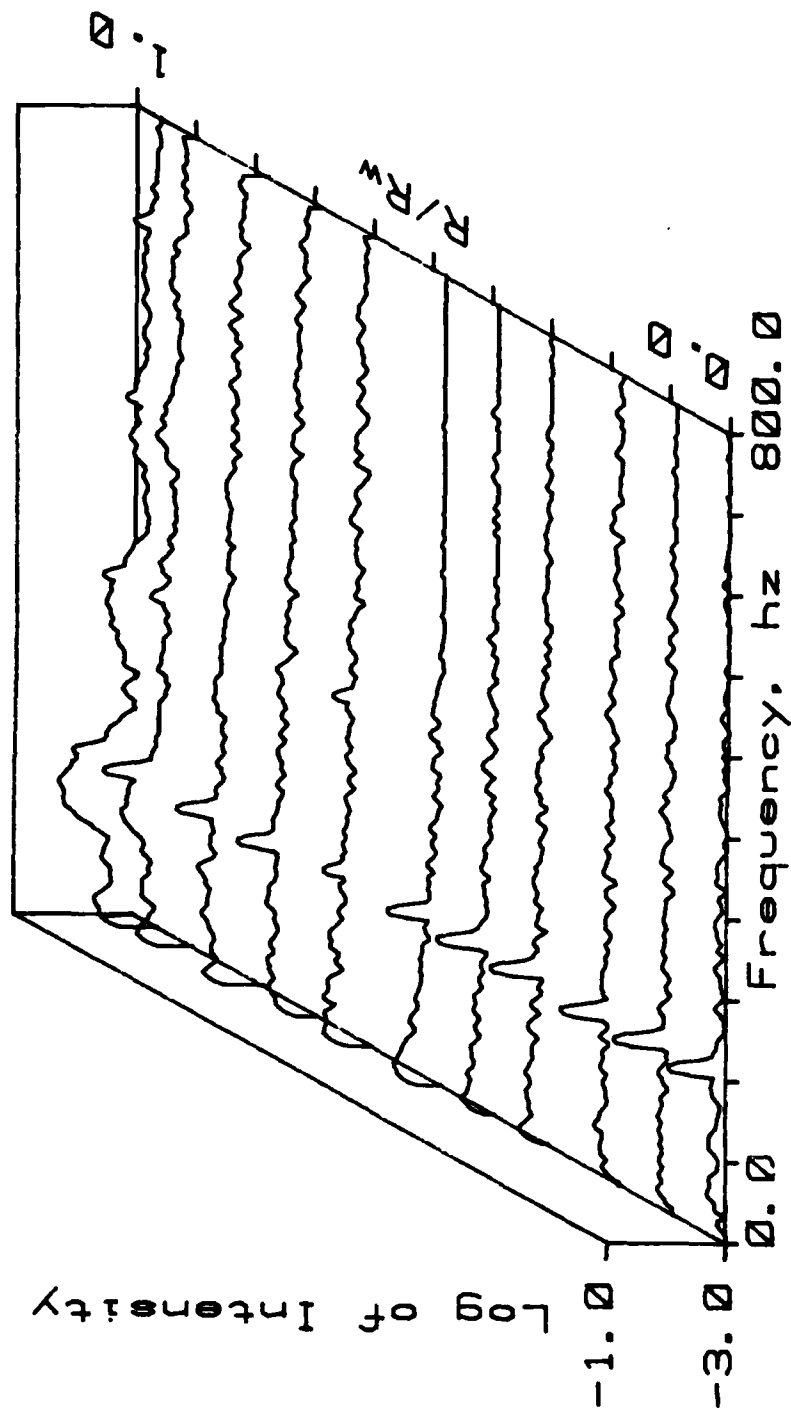


Figure B-4.

TURBULENCE INTENSITY PROFILE

Z/D = 4.22 Freq = 84.00 Hz. $\Delta/\Delta t = 3.30 \times 10^{-3}$ Max1013 = 1.00

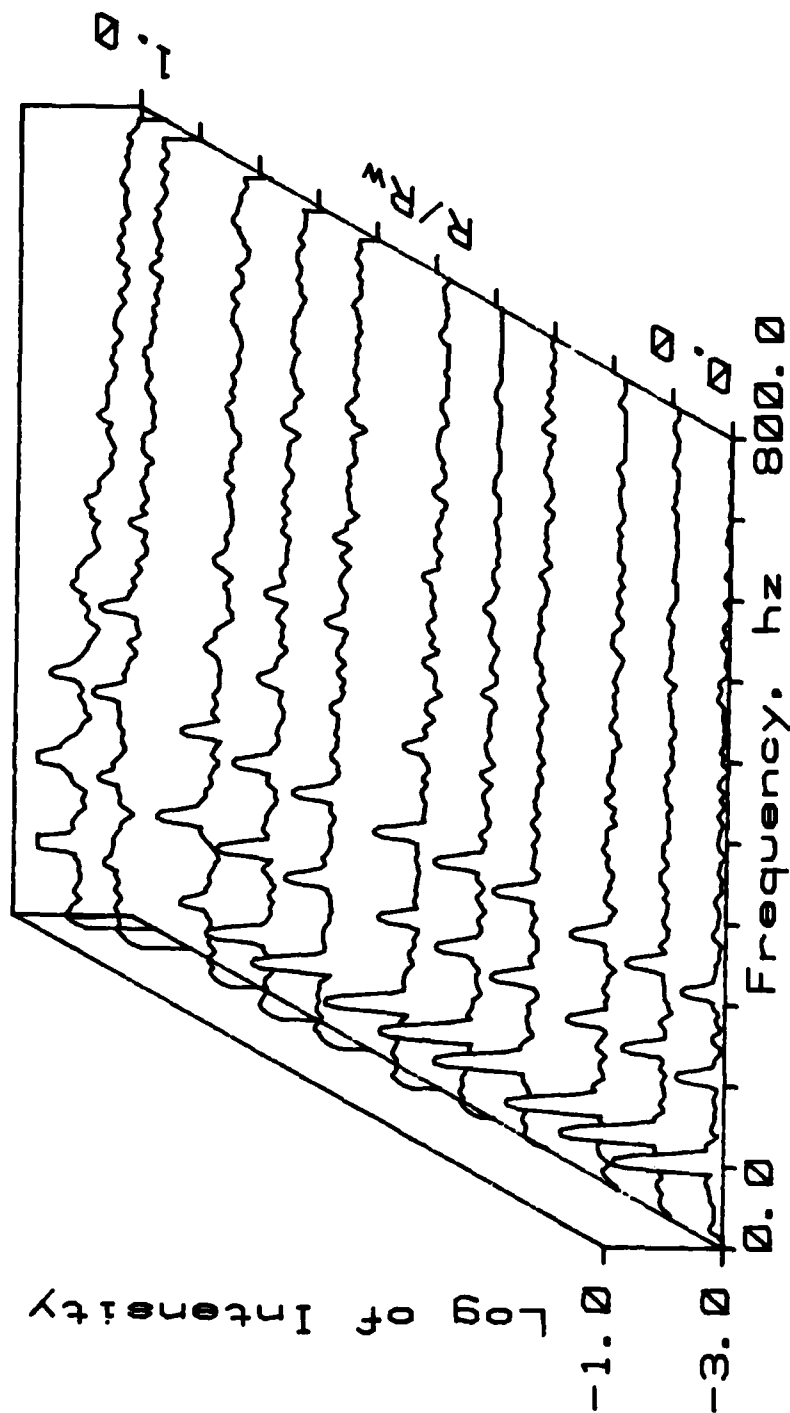


Figure B-5.

TURBULENCE INTENSITY PROFILE

Z/D = 4.22 Freq = 170.00 Hz. $\Delta/\Delta t = 3.30 \times 10^{-3}$ Max10T3 = 1.80

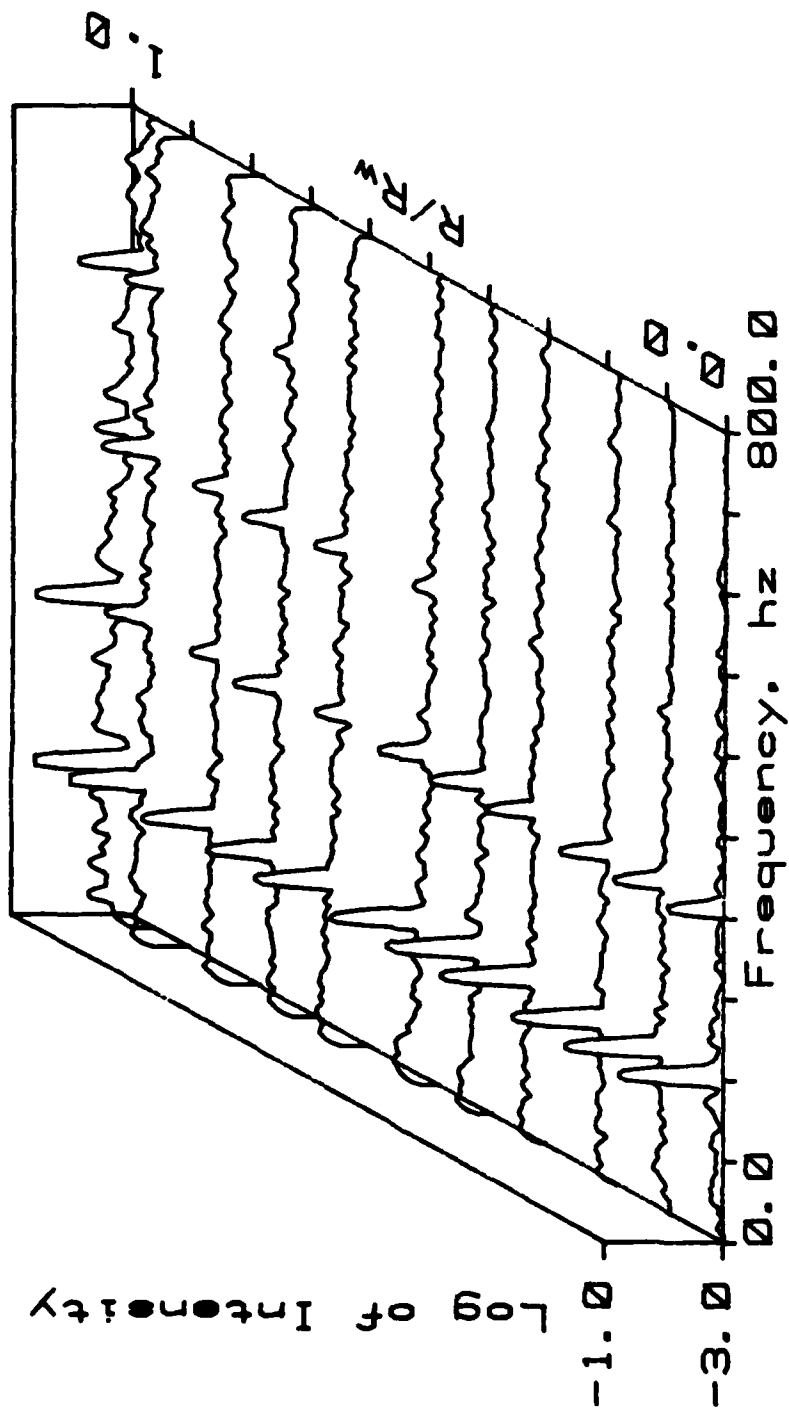


Figure B-6.

NORMALIZED ACOUSTIC VELOCITY PROFILE

$Z/D = 4.22$ Freq = 84.00 A/Ac = 0.60 % Max10t3 = 1.80

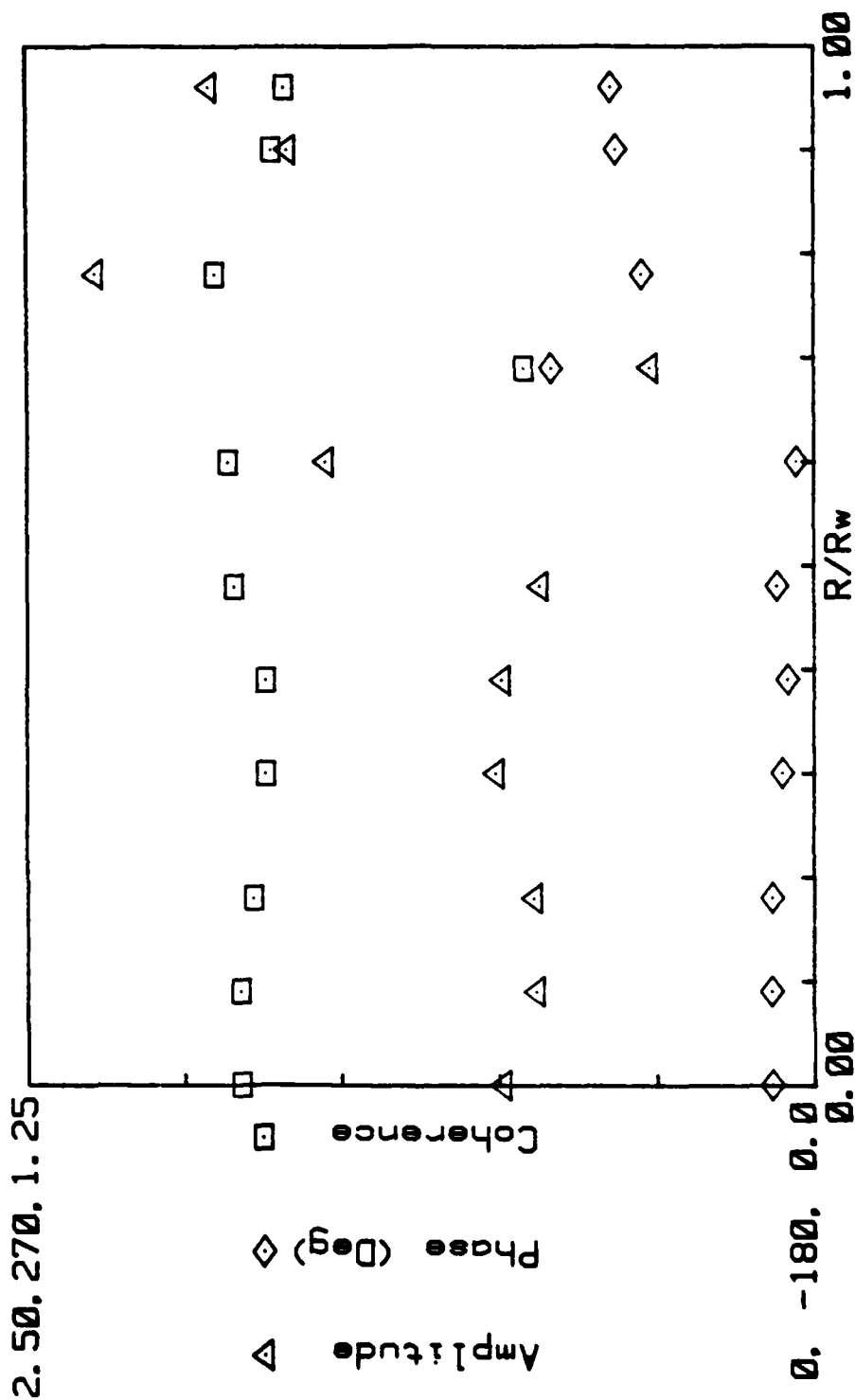


Figure B-7.

NORMALIZED ACOUSTIC VELOCITY PROFILE

Z/D = 4.22 Freq = 170.00 A/Ac = 0.60 % Max10f3 = 1.80

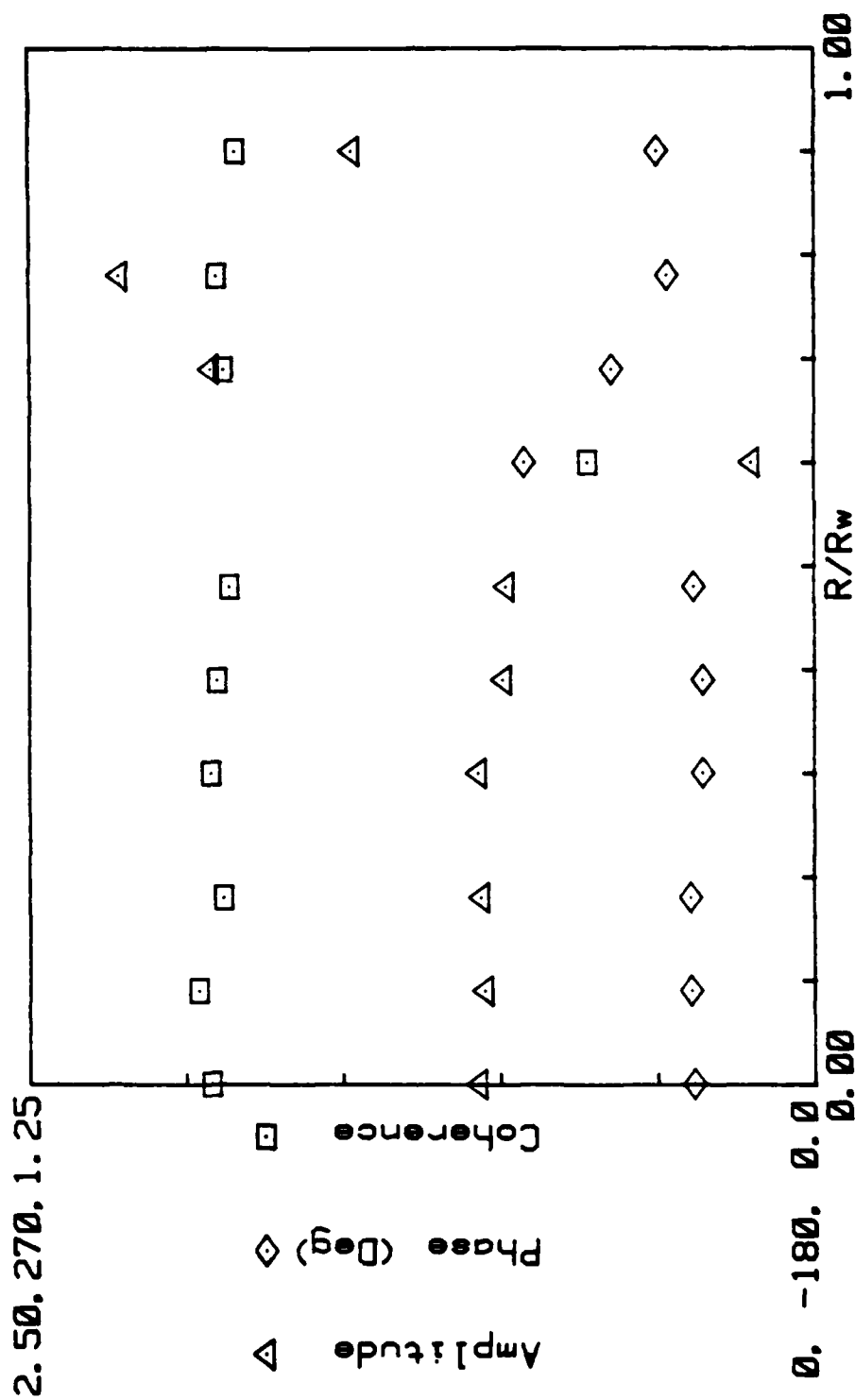


Figure B-8.

NORMALIZED ACOUSTIC VELOCITY PROFILE

Z/D = 4.22 Freq = 84.00 A/Lt = 3.30 % Max10f3 = 1.80

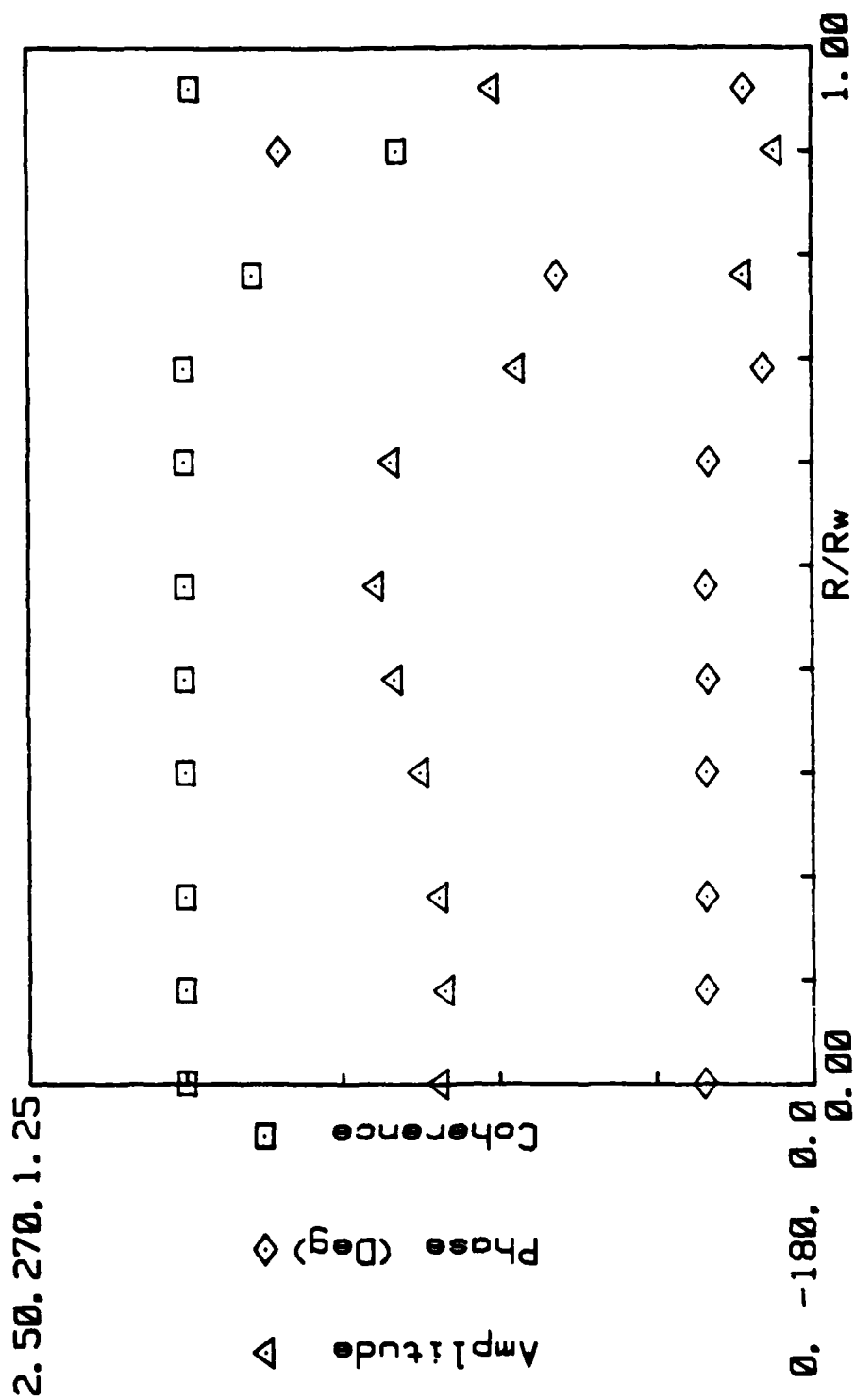


Figure B-9.

NORMALIZED ACOUSTIC VELOCITY PROFILE

$Z/D = 4.22$ $\text{Freq} = 170.00$ $A/\Delta t = 3.30 \times 10^{13} = 1.00$

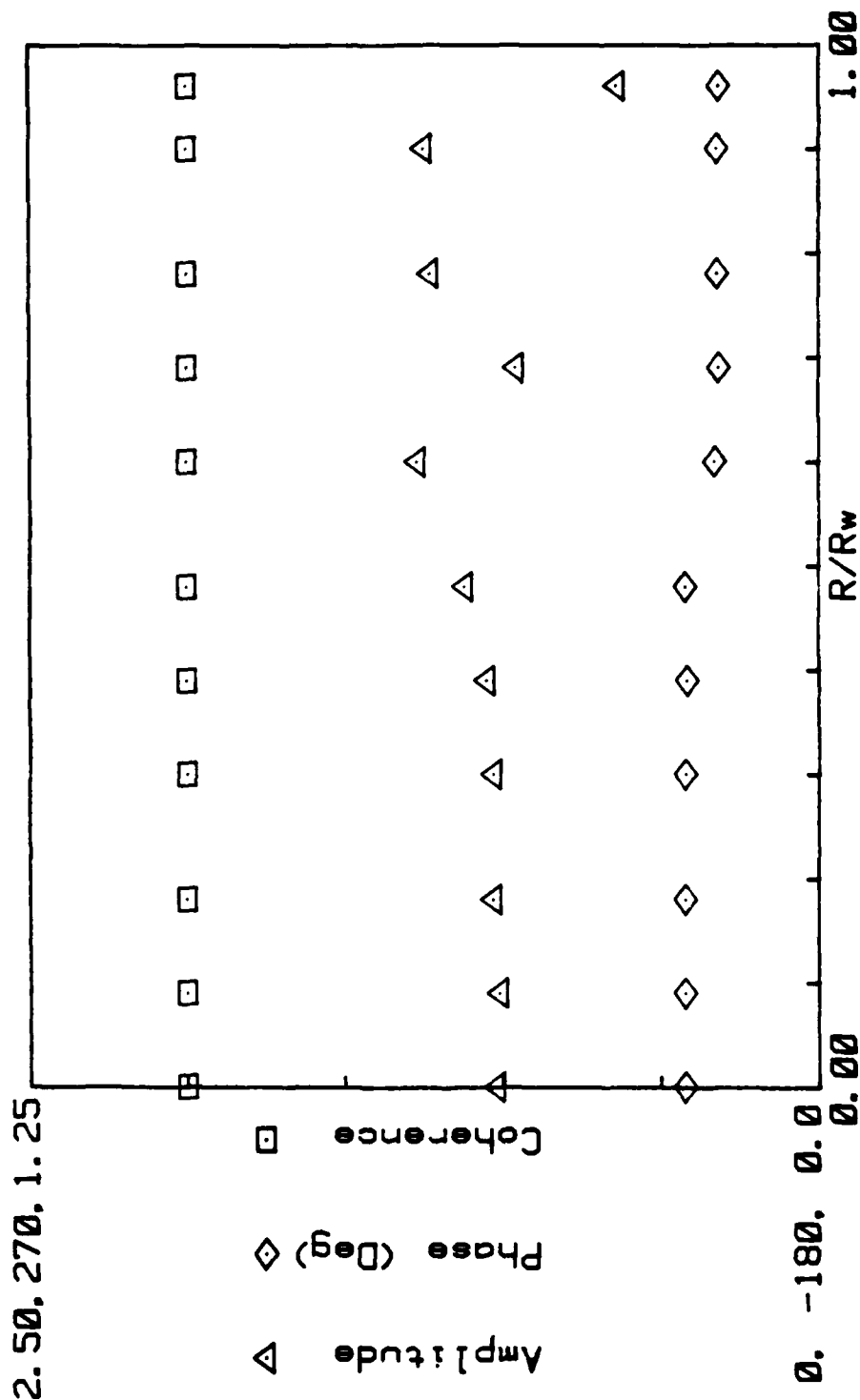
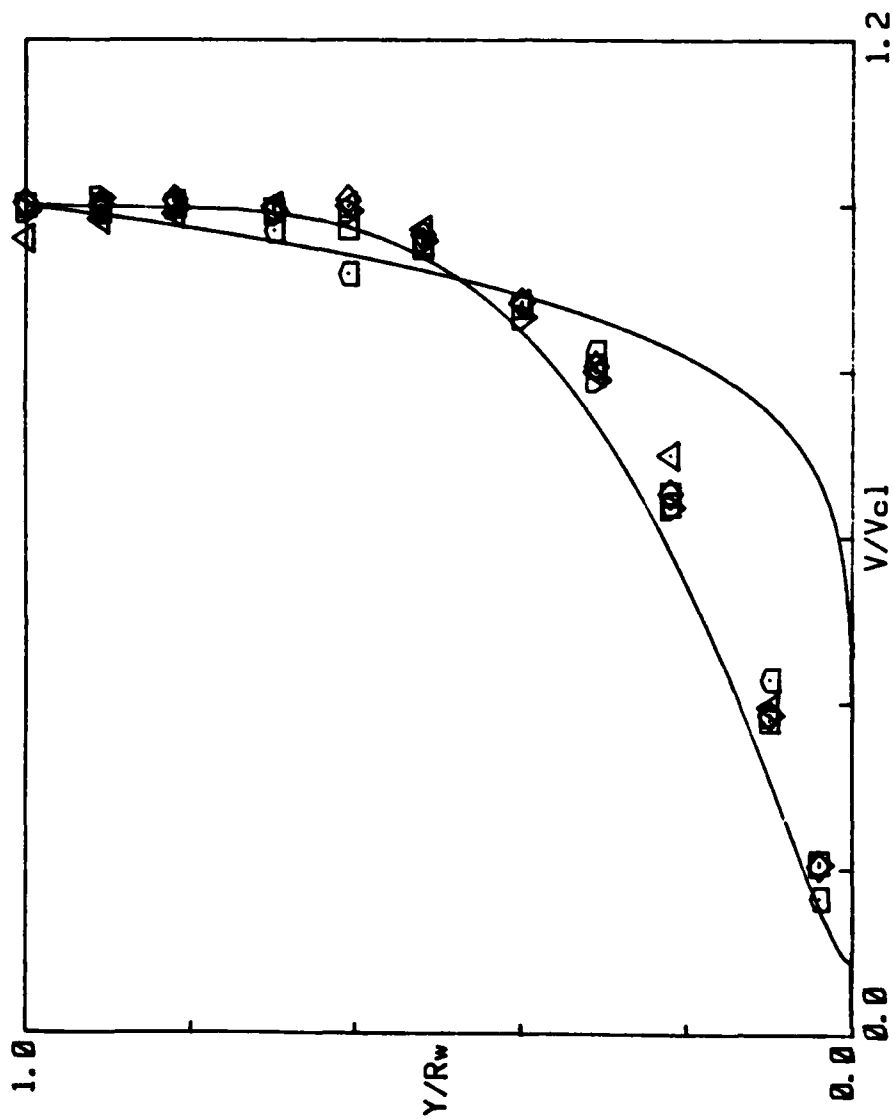


Figure B-10.

MEAN VELOCITY PROFILE



$Z/D = 1.80$

$Ms = 0.001800$

Figure B-11.

TURBULENCE INTENSITY PROFILE

Z/D = 4.22 Freq = 0.000 Hz $\Delta/\Delta t = 0.00 \times$ Max10f3 = 1.00

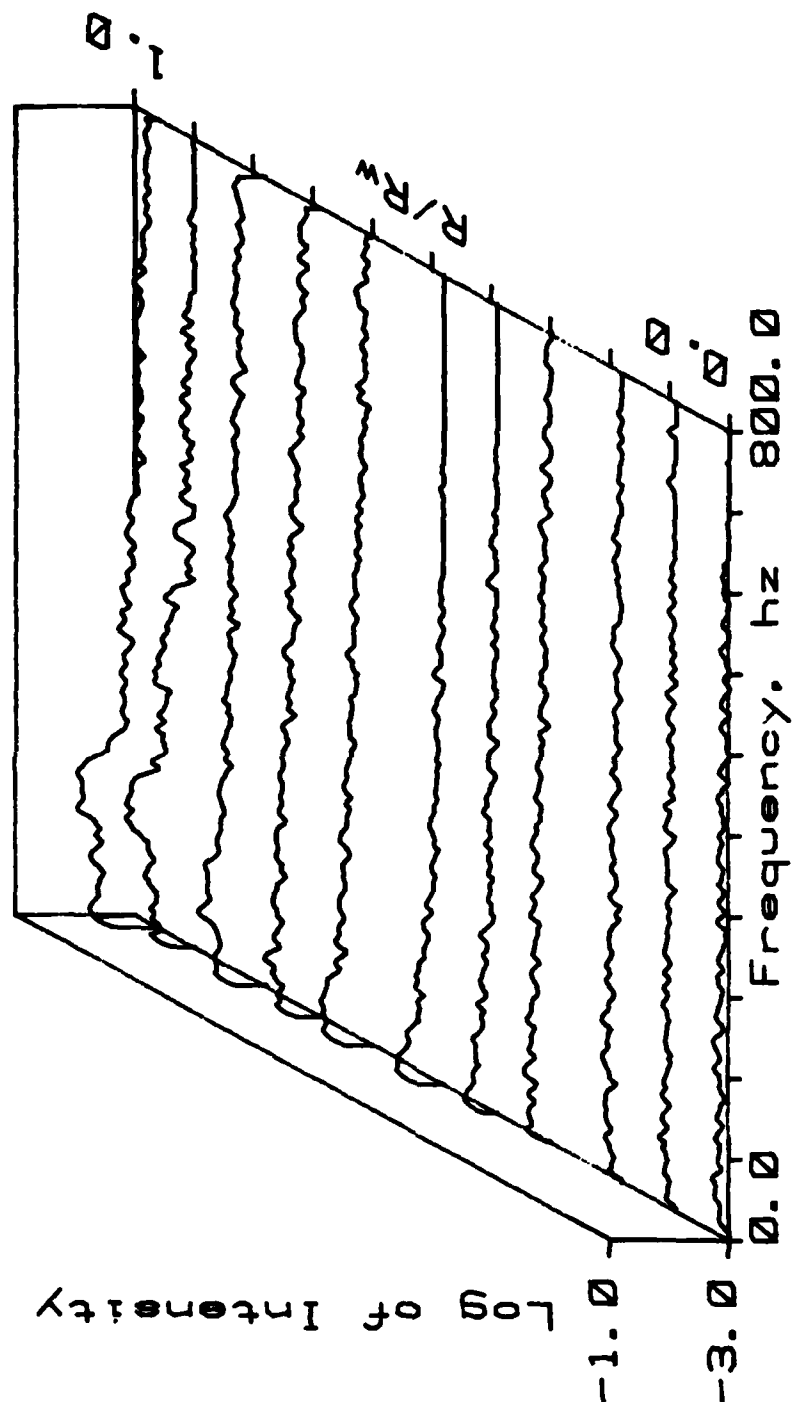


Figure B-12.

TURBULENCE INTENSITY PROFILE

Z/D = 4.22 Freq = 65.00 Hz. A/A_t = 0.60 x Max10f3 = 1.80

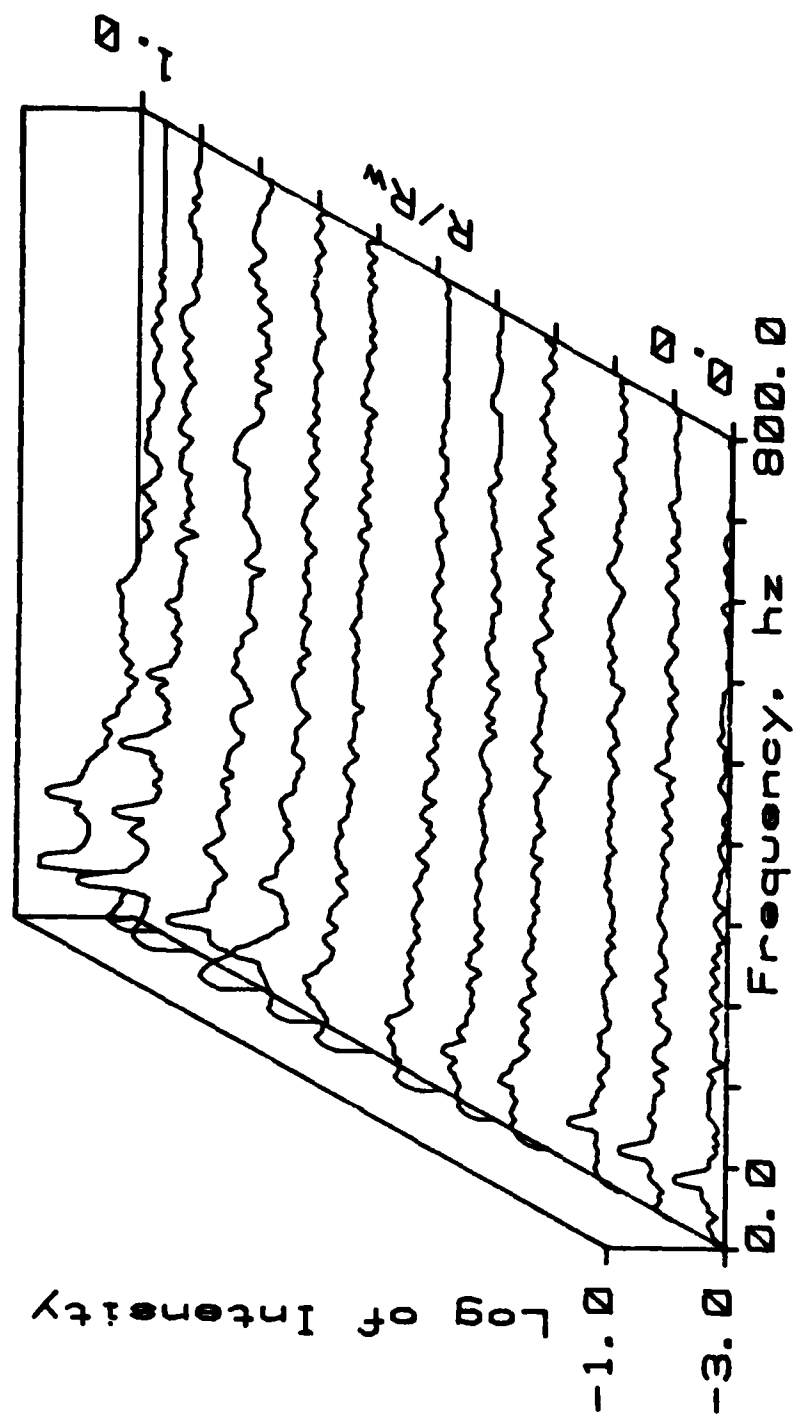


Figure B-13.

TURBULENCE INTENSITY PROFILE

Z/D = 4.22 Freq = 135.00 Hz. A/A_c = 0.60 x Max1013 = 1.00

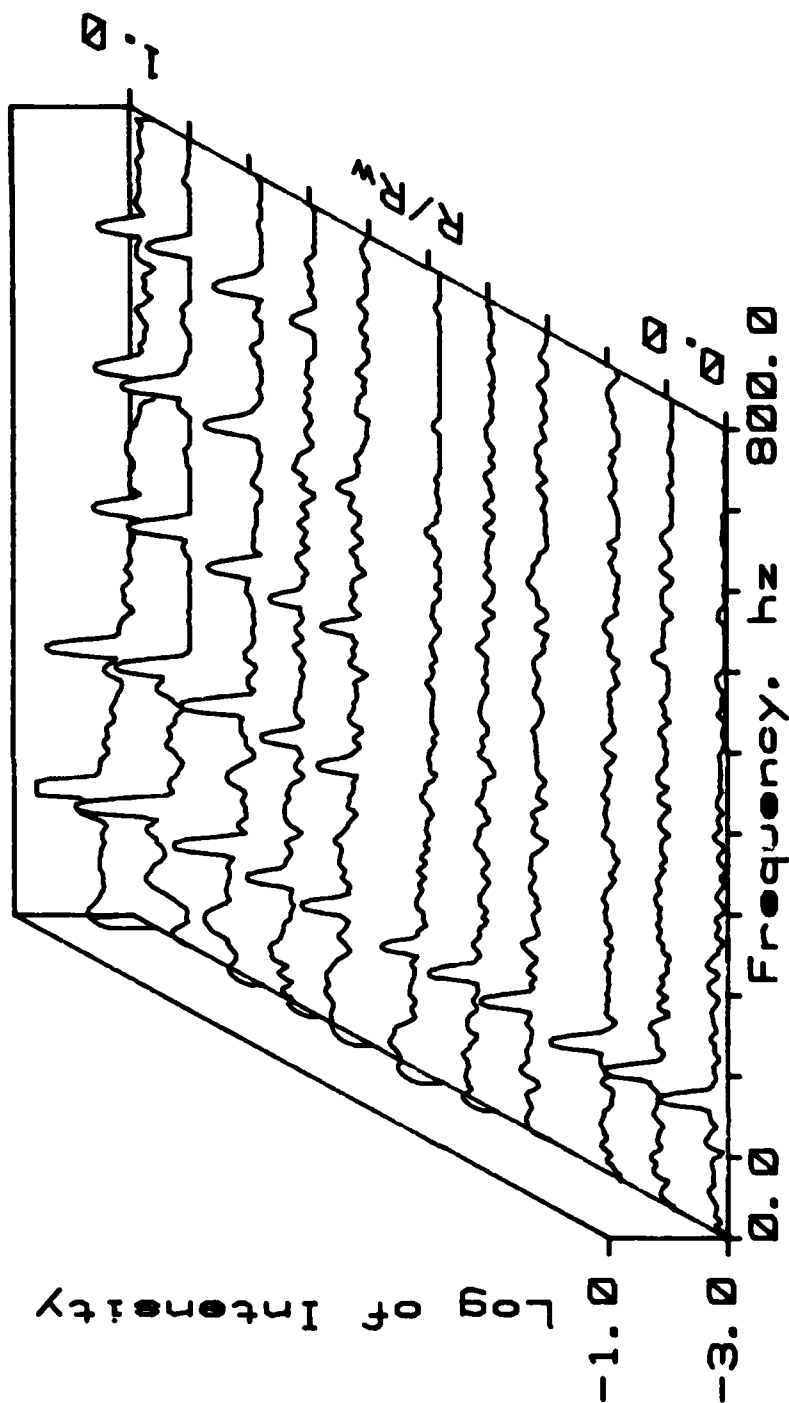


Figure B-14.

TURBULENCE INTENSITY PROFILE

Z/D = 4.22 Freq = 65.00 Hz. $\Delta/\Delta t = 3.30 \times 10^{-3}$ Max10f3 = 1.00

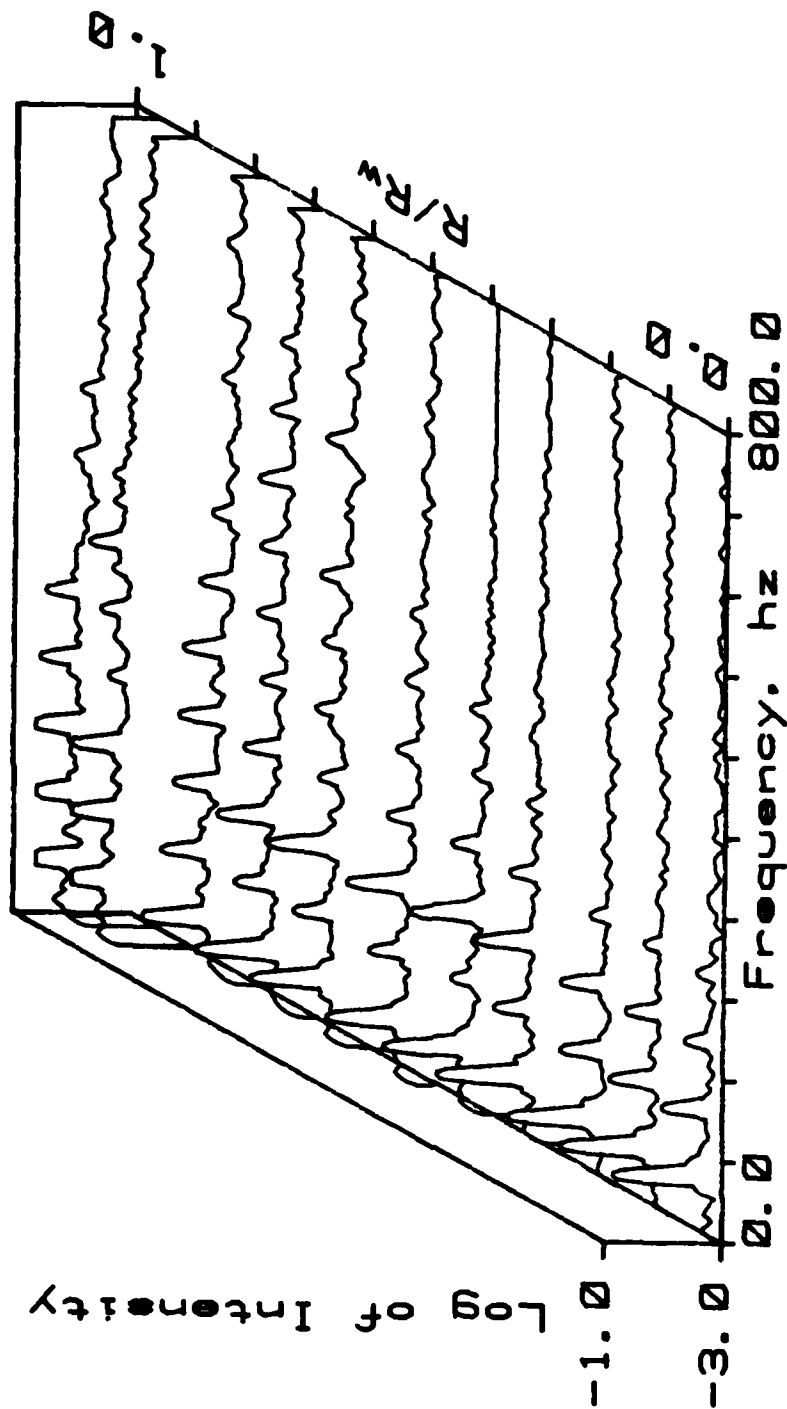


Figure B-15.

TURBULENCE INTENSITY PROFILE

Z/D = 4.22 Freq = 140.00 Hz. $\Delta/\Delta t = 3.30 \times 10^{-3}$ Max1013 = 1.00

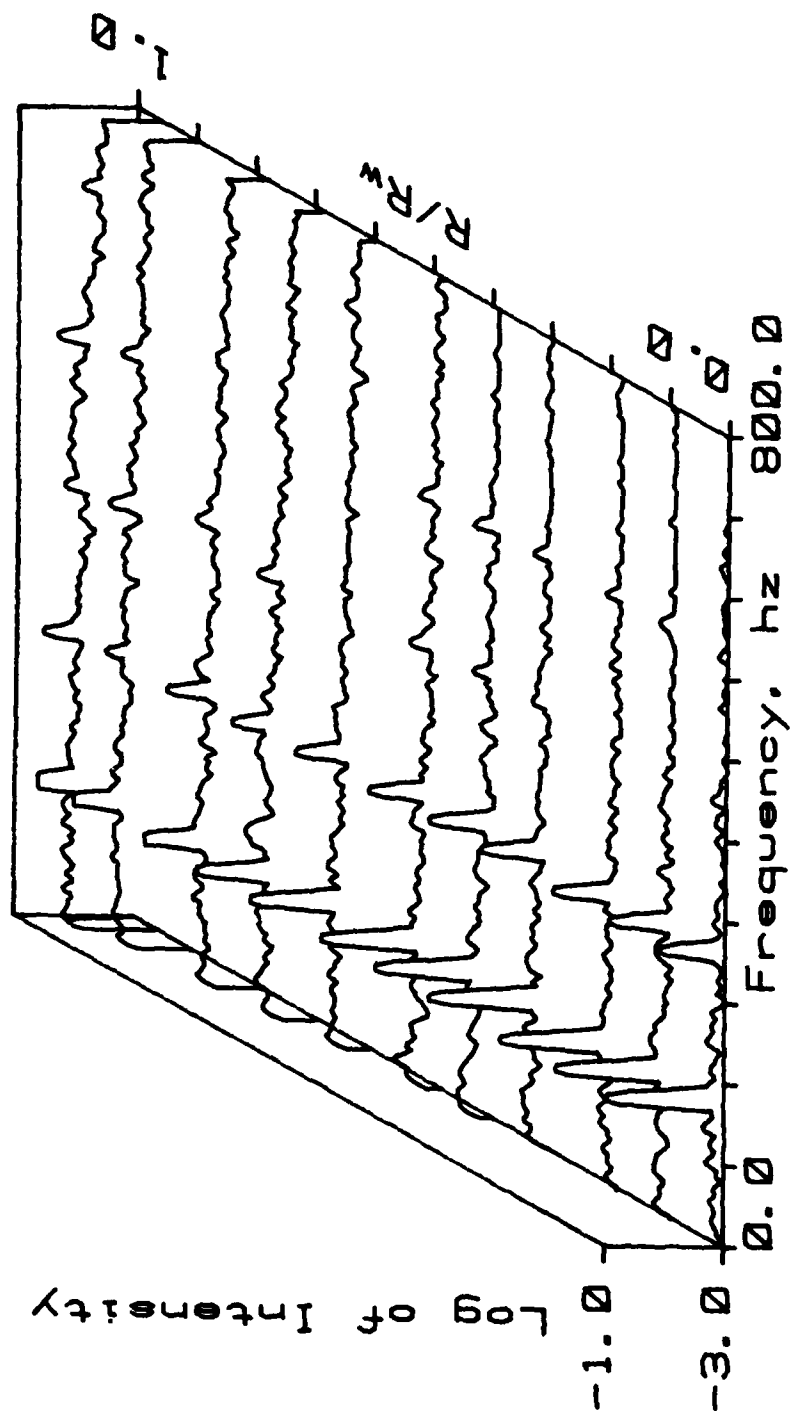


Figure B-16.

NORMALIZED ACOUSTIC VELOCITY PROFILE

$Z/D = 4.22$ $\text{Freq} = 65.00$ $A/\lambda t = 0.60$ $\lambda \times 10^3 = 1.80$

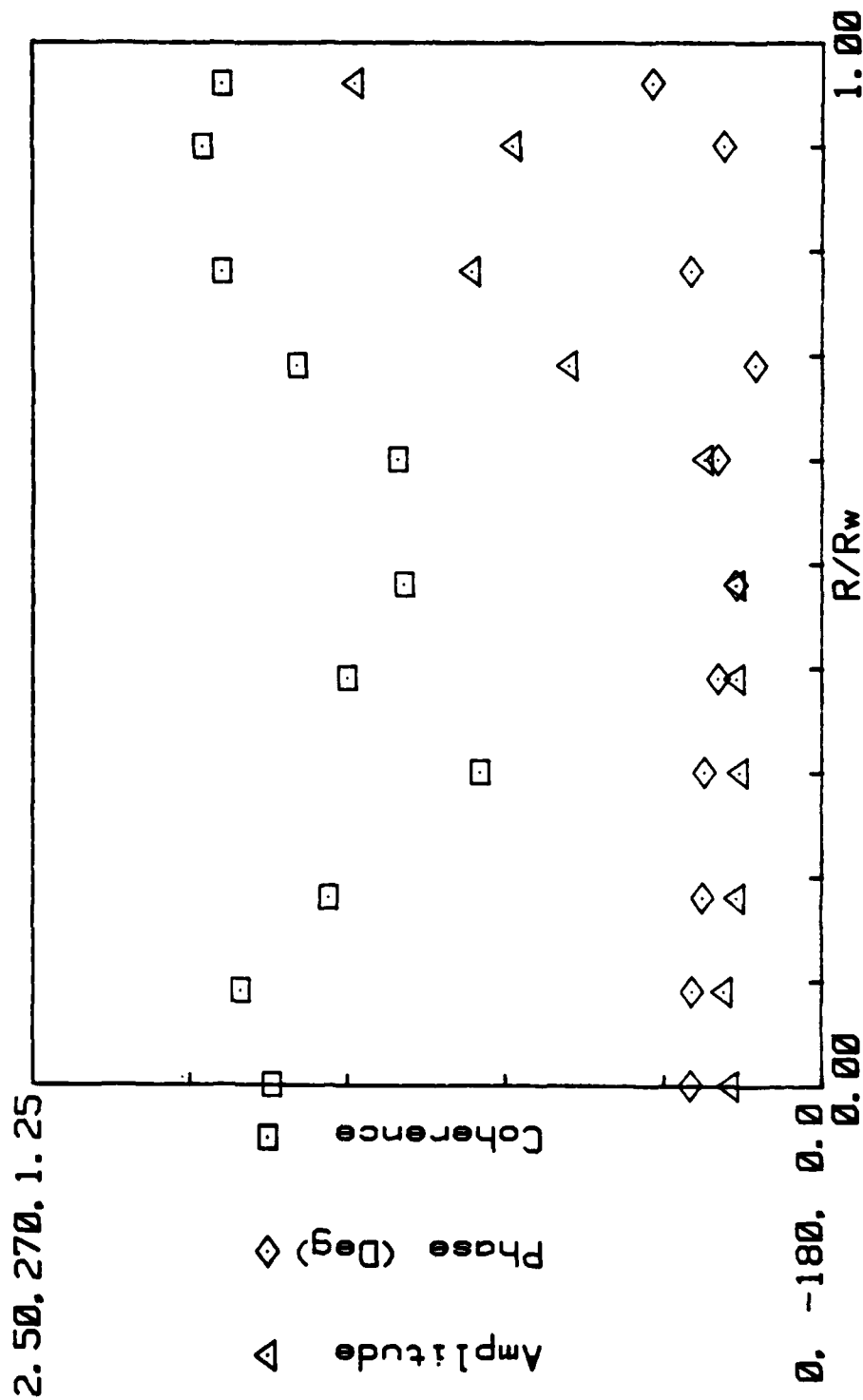


Figure B-17.

NORMALIZED ACOUSTIC VELOCITY PROFILE

Z/D = 4.22 Freq = 135.00 A/Ac = 0.60 X Max10t3 = 1.80

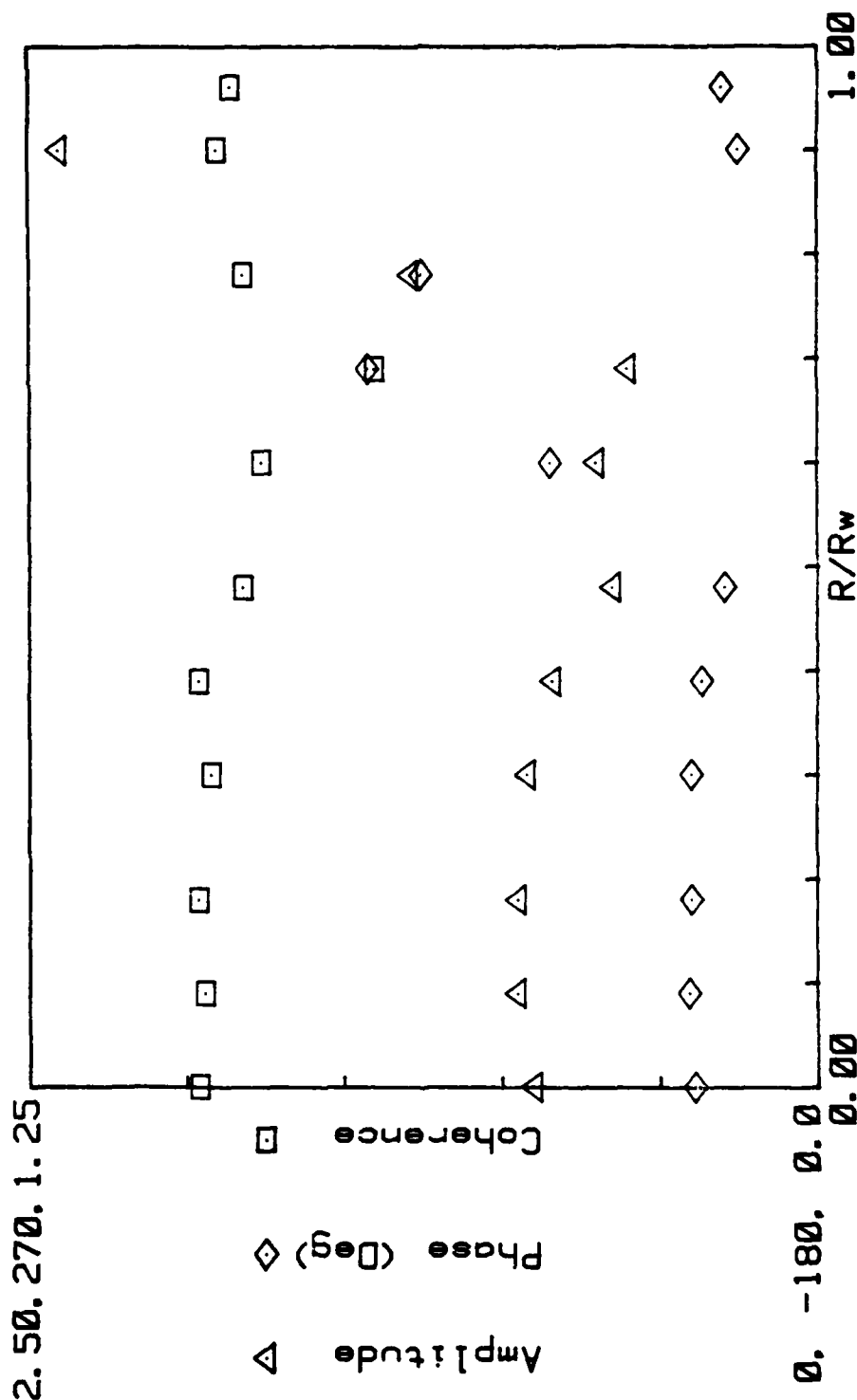


Figure B-18.

NORMALIZED ACOUSTIC VELOCITY PROFILE

$Z/O = 4.22$ $\text{Freq} = 65.00$ $A/A_t = 3.30$ \times $N_{\text{ex}} 10^{13} = 1.80$

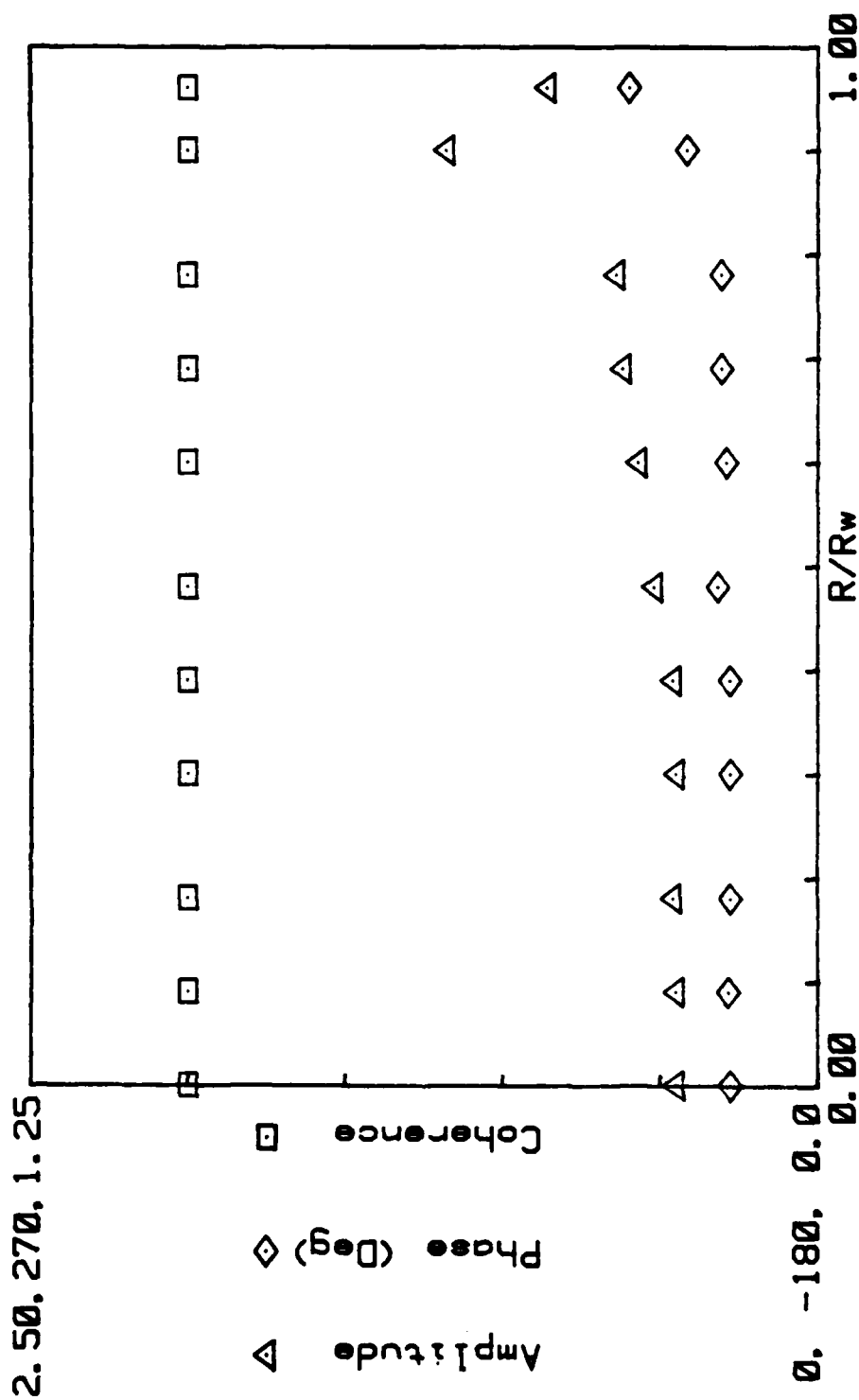


Figure B-19.

NORMALIZED ACOUSTIC VELOCITY PROFILE

$Z/D = 4.22$ Freq = 135.00 N/Ac = 3.30 λ Mex10f3 = 1.80

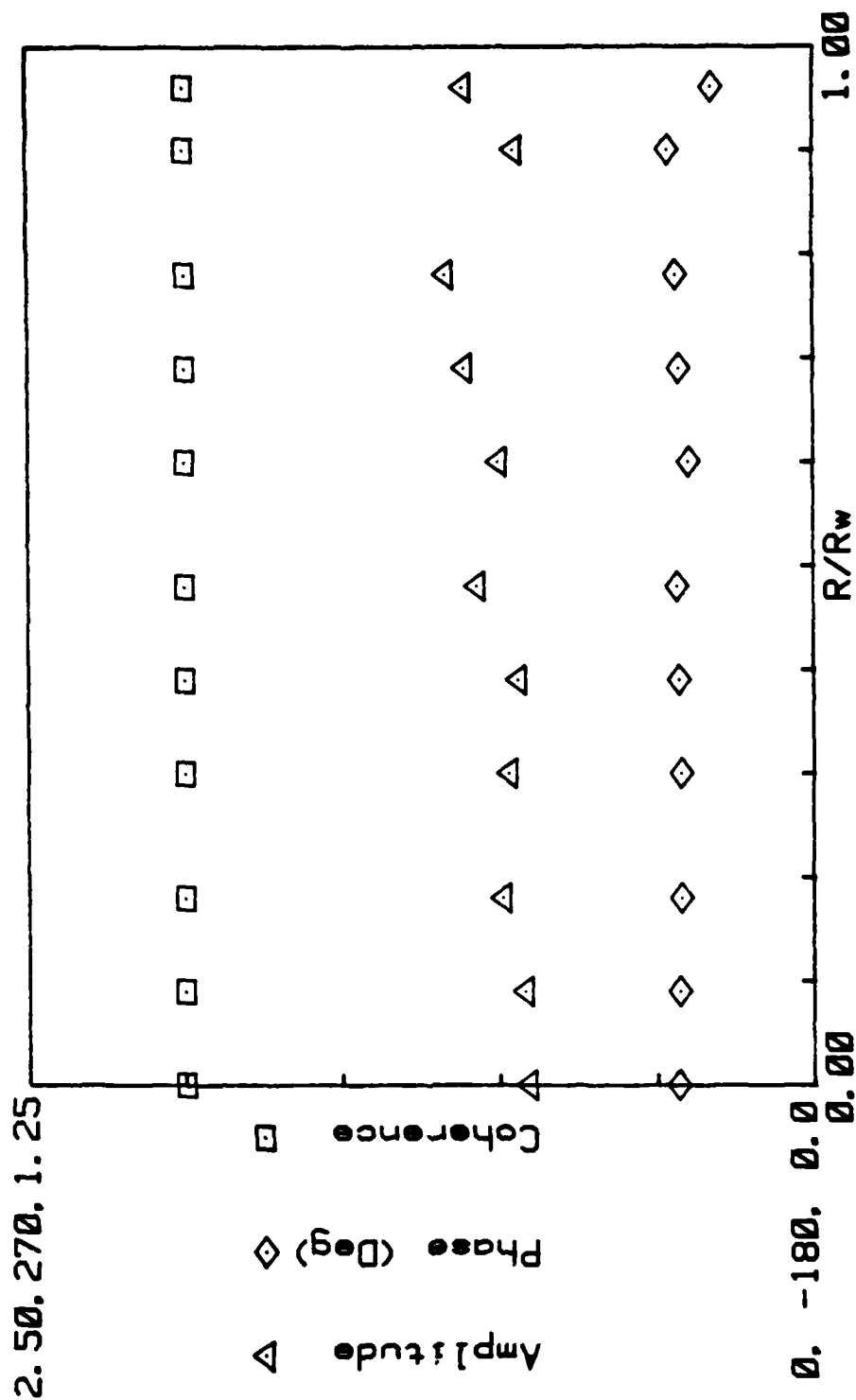


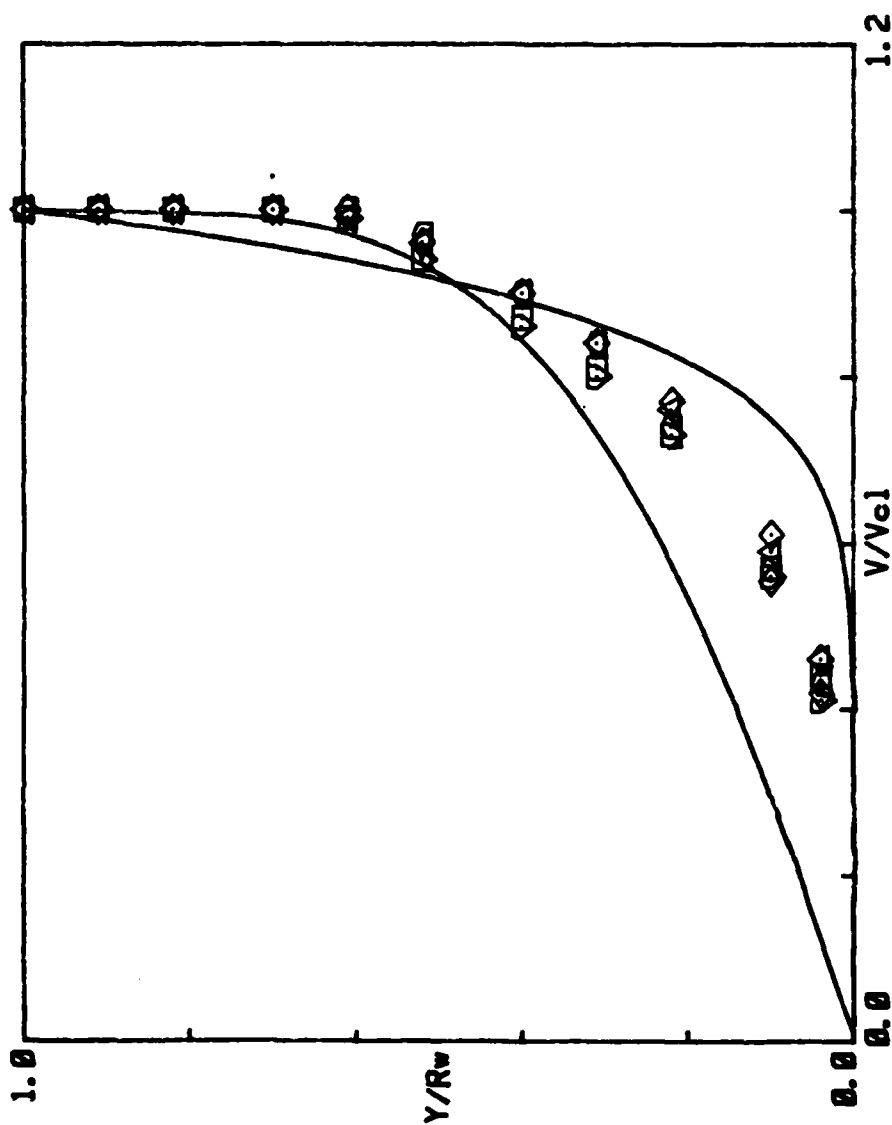
Figure B-20.

APPENDIX C

Additional Flowfield Data

at $Z/D = 11.5$

MEAN VELOCITY PROFILE



$Z/D = 11.50$			
$Ma = 0.001750$			
SYM	Λ/Λ_t	F Hz.	
∇	0.00	0	
\square	0.60	84	
\diamond	0.60	170	
\triangle	3.30	84	
\square	3.30	170	

Figure C-1.

TURBULENCE INTENSITY PROFILE

Z/D = 11.50 Freq = 0.00 Hz. $\Delta/\Delta t = 0.00 \times$ Max10f3 = 1.75

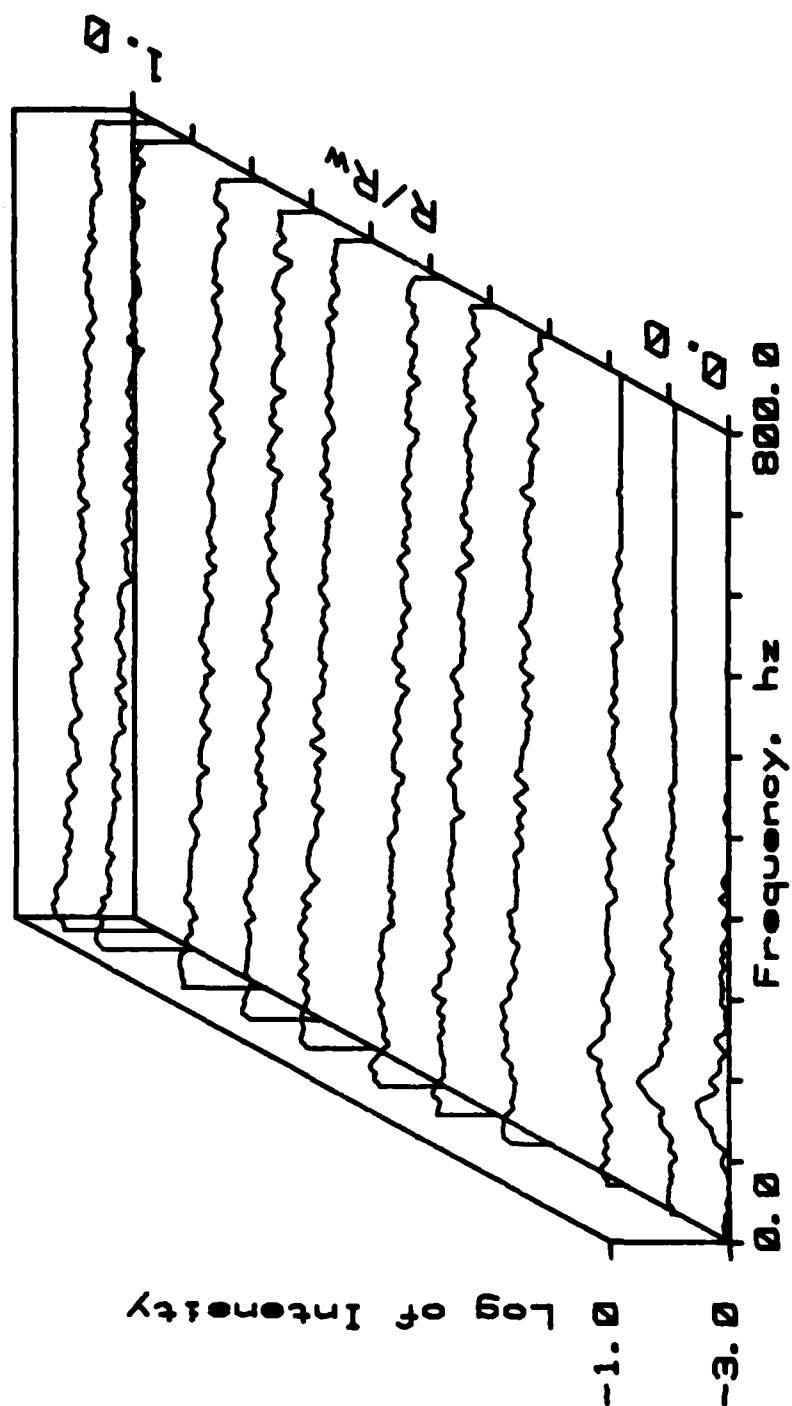


Figure C-2.

TURBULENCE INTENSITY PROFILE

Z/D = 11.50 Freq = 84.00 Hz. A/At = 0.60 x Max1013 = 1.80

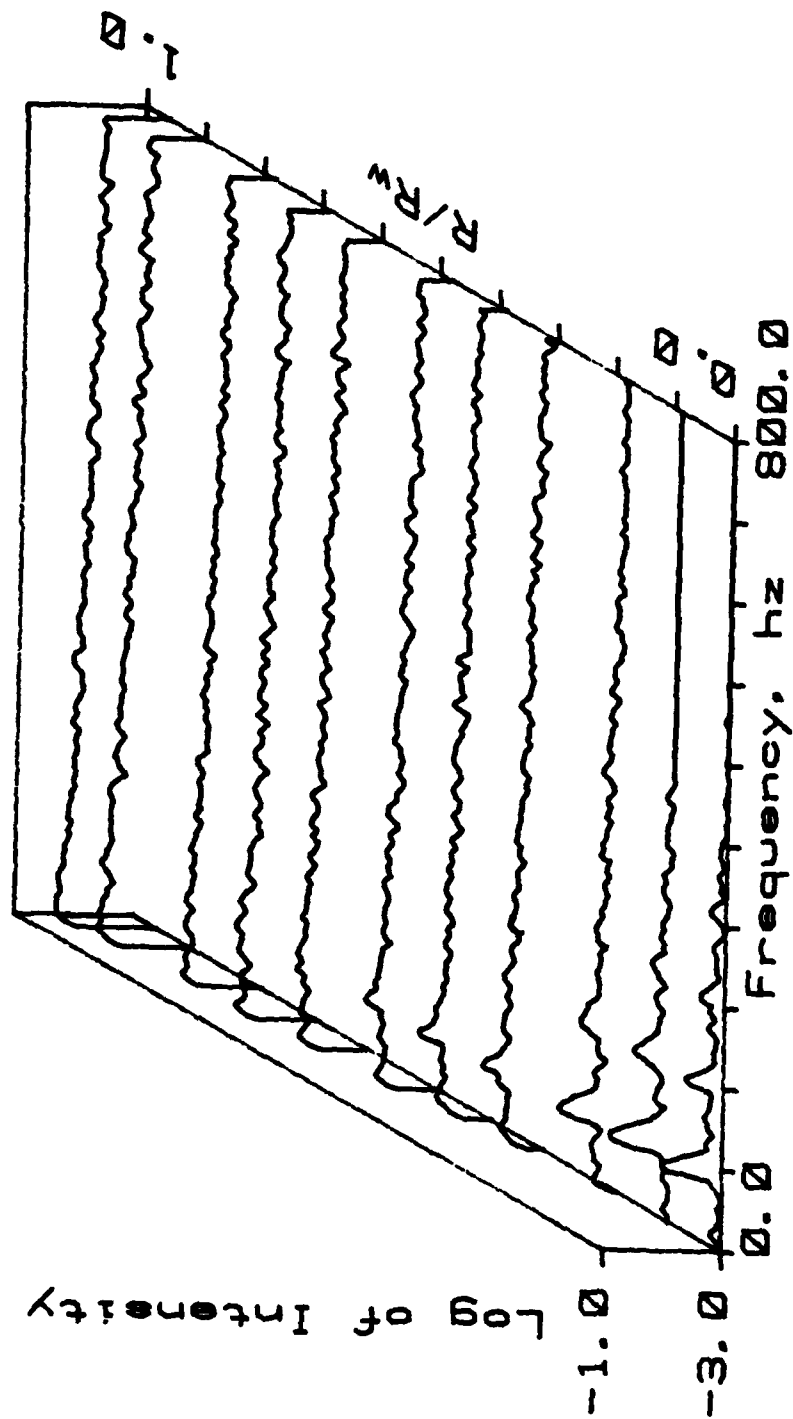


Figure C-3.

TURBULENCE INTENSITY PROFILE

Z/D = 11.50 Freq = 170.00 Hz. $\Lambda/\Lambda_c = 3.30 \times 10^{-3}$ $M \times 10^3 = 1.80$

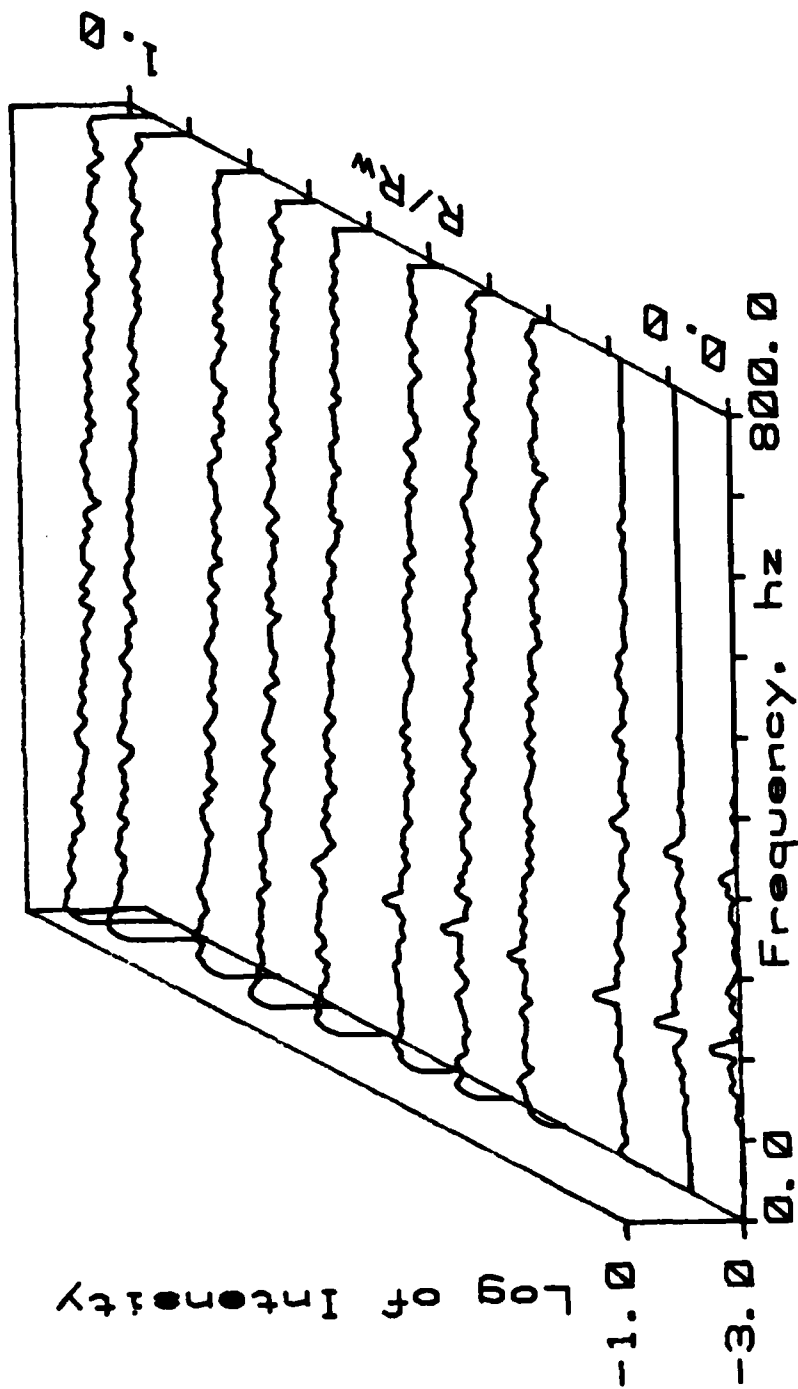


Figure C-4.

TURBULENCE INTENSITY PROFILE

Z/D = 11.50 Freq = 84.00 Hz. $\lambda/\lambda_t = 3.30 \times$ Mex10f3 = 1.00

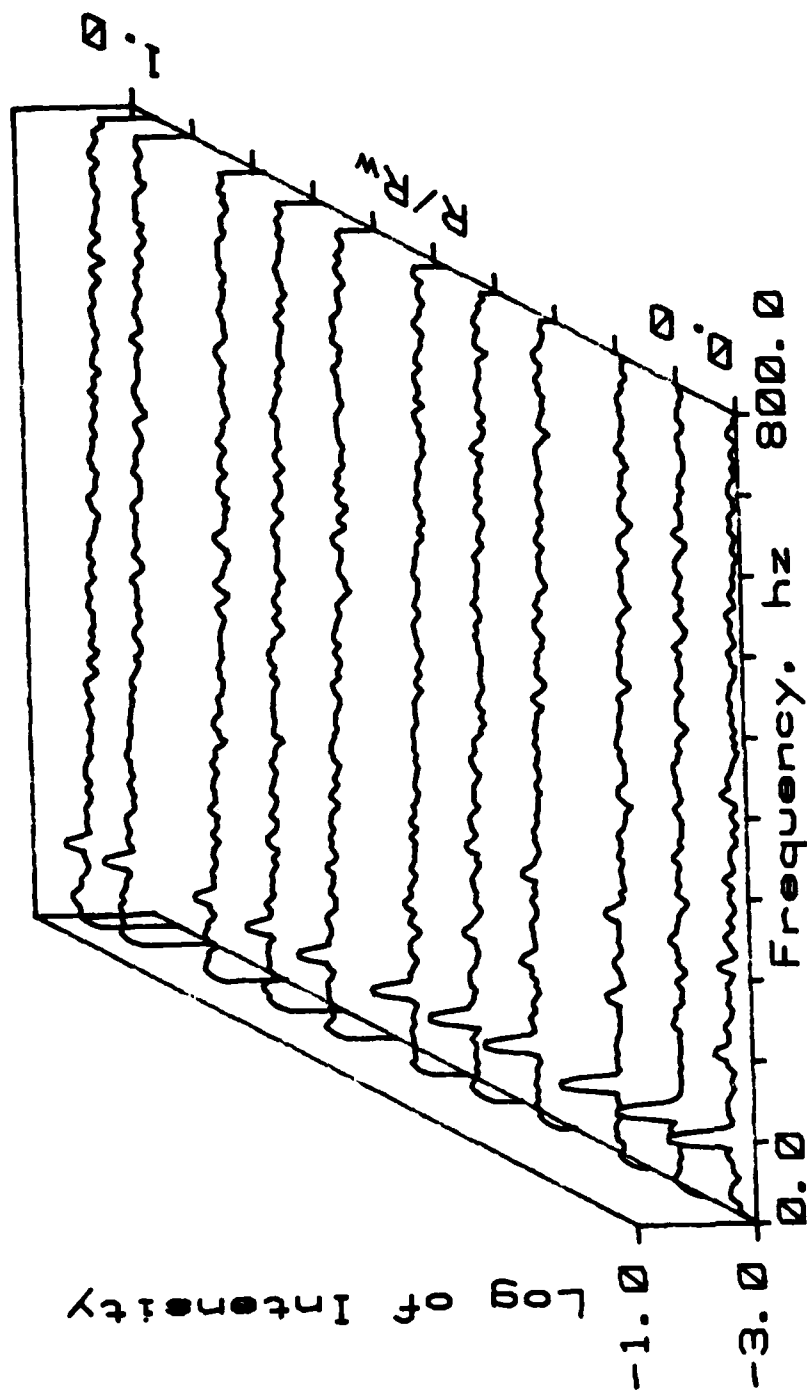


Figure C-5.

TURBULENCE INTENSITY PROFILE

Z/D = 11.50 Freq = 170.00 Hz. $\Delta/\Delta t = 3.30 \times 10^{-3}$ Max10t3 = 1.00

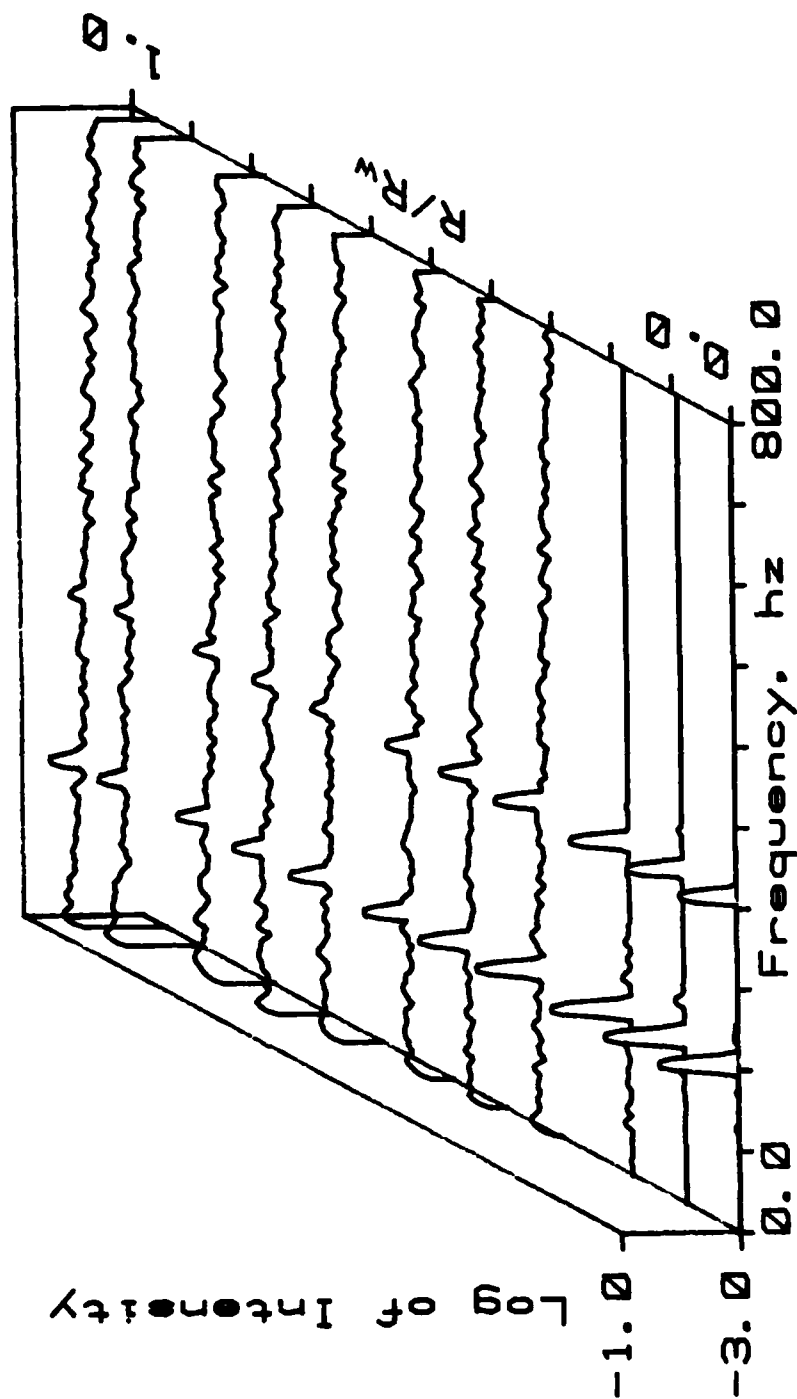


Figure C-6.

NORMALIZED ACOUSTIC VELOCITY PROFILE

Z/D = 11.50 Freq = 84.00 A/Ac = 0.00 X Max1013 = 1.00

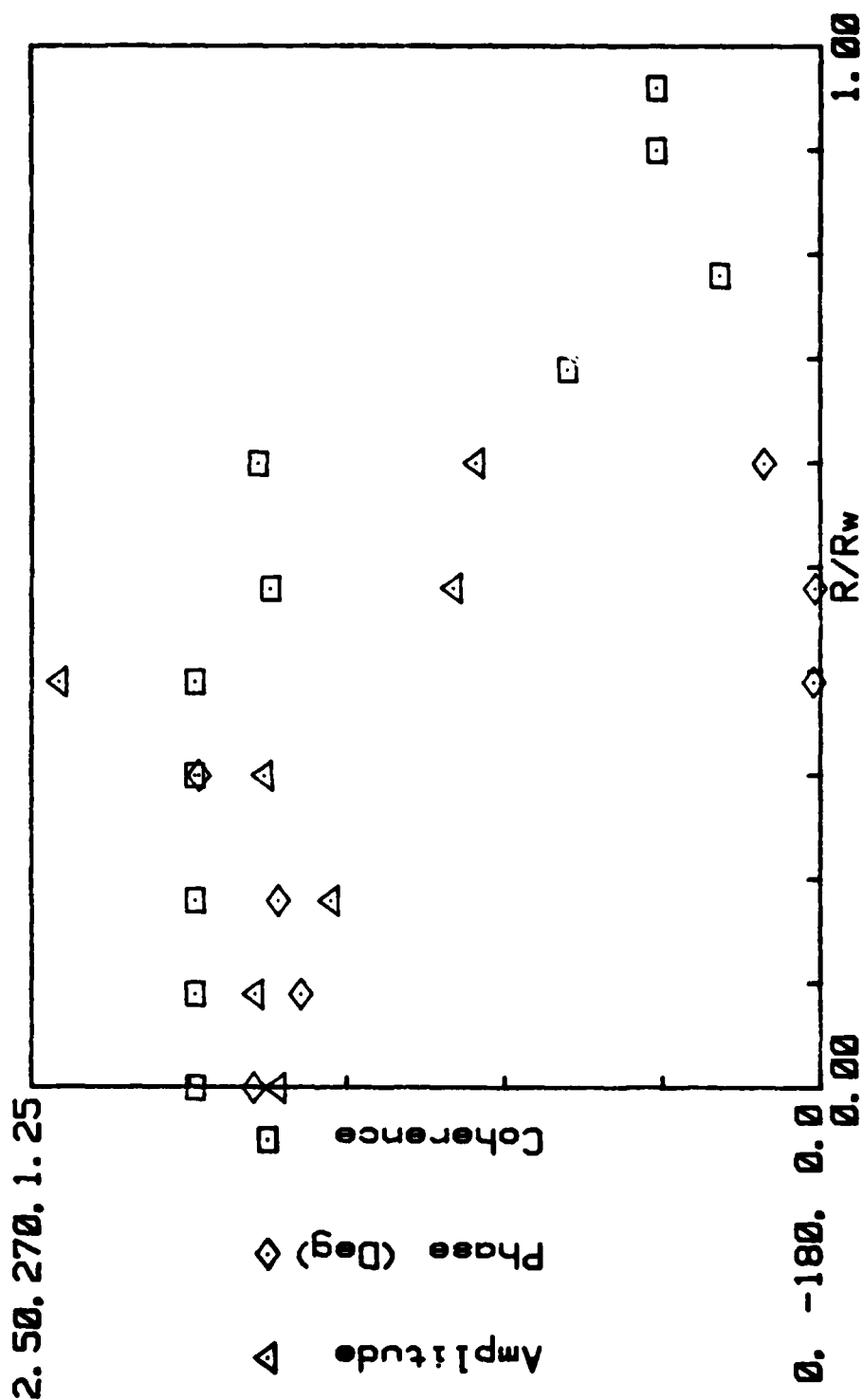


Figure C-7.

NORMALIZED ACOUSTIC VELOCITY PROFILE

Z/D = 11.50 Freq = 170.00 A/Ac = 0.60 x Max1013 = 1.00

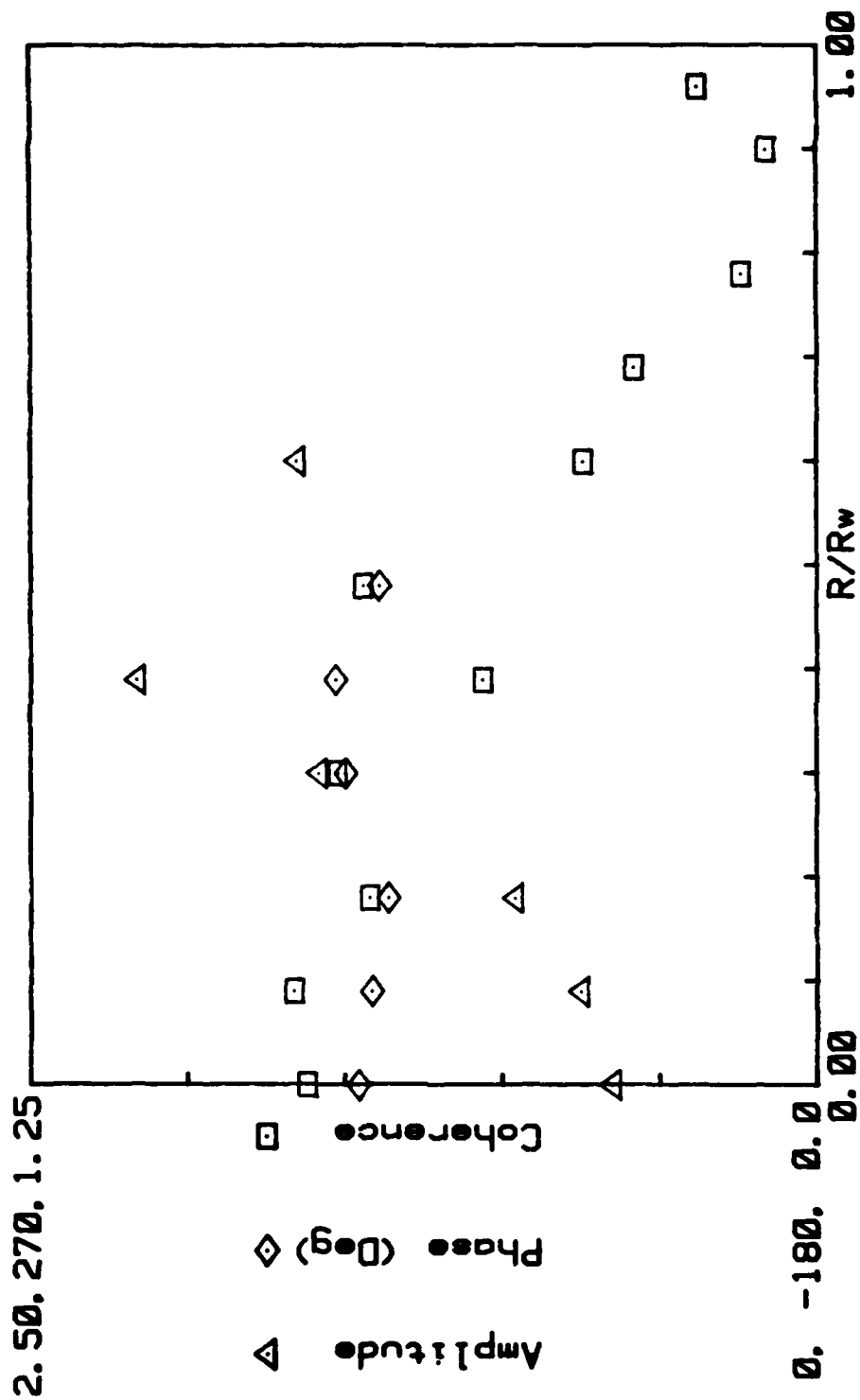


Figure C-8.

NORMALIZED ACOUSTIC VELOCITY PROFILE

Z/D = 11.50 Freq = 84.00 A/At = 3.30 X Max10f3 = 1.00

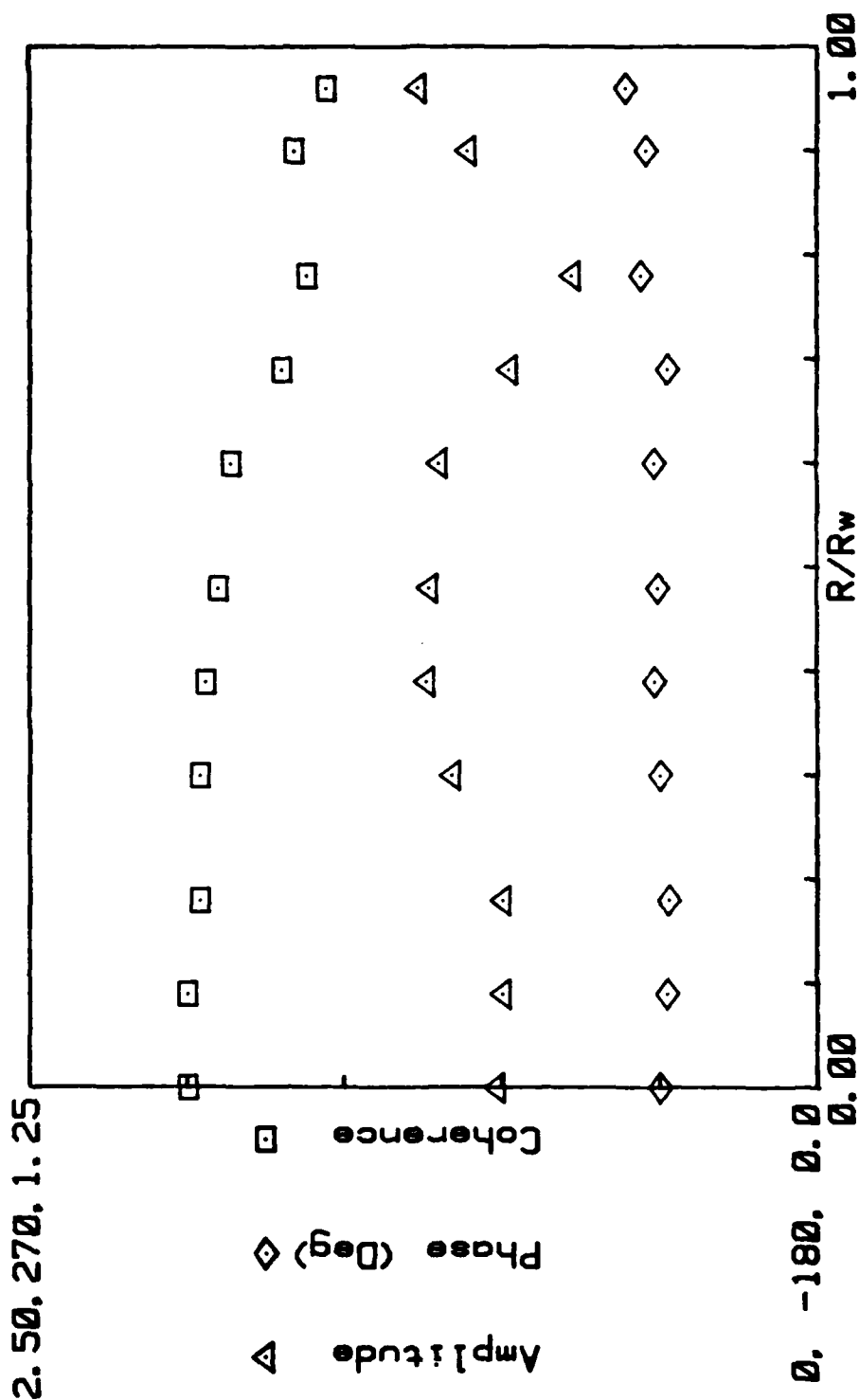


Figure C-9.

NORMALIZED ACOUSTIC VELOCITY PROFILE

Z/D = 11.50 Freq = 170.00 A/At = 3.30 X Max10t3 = 1.00

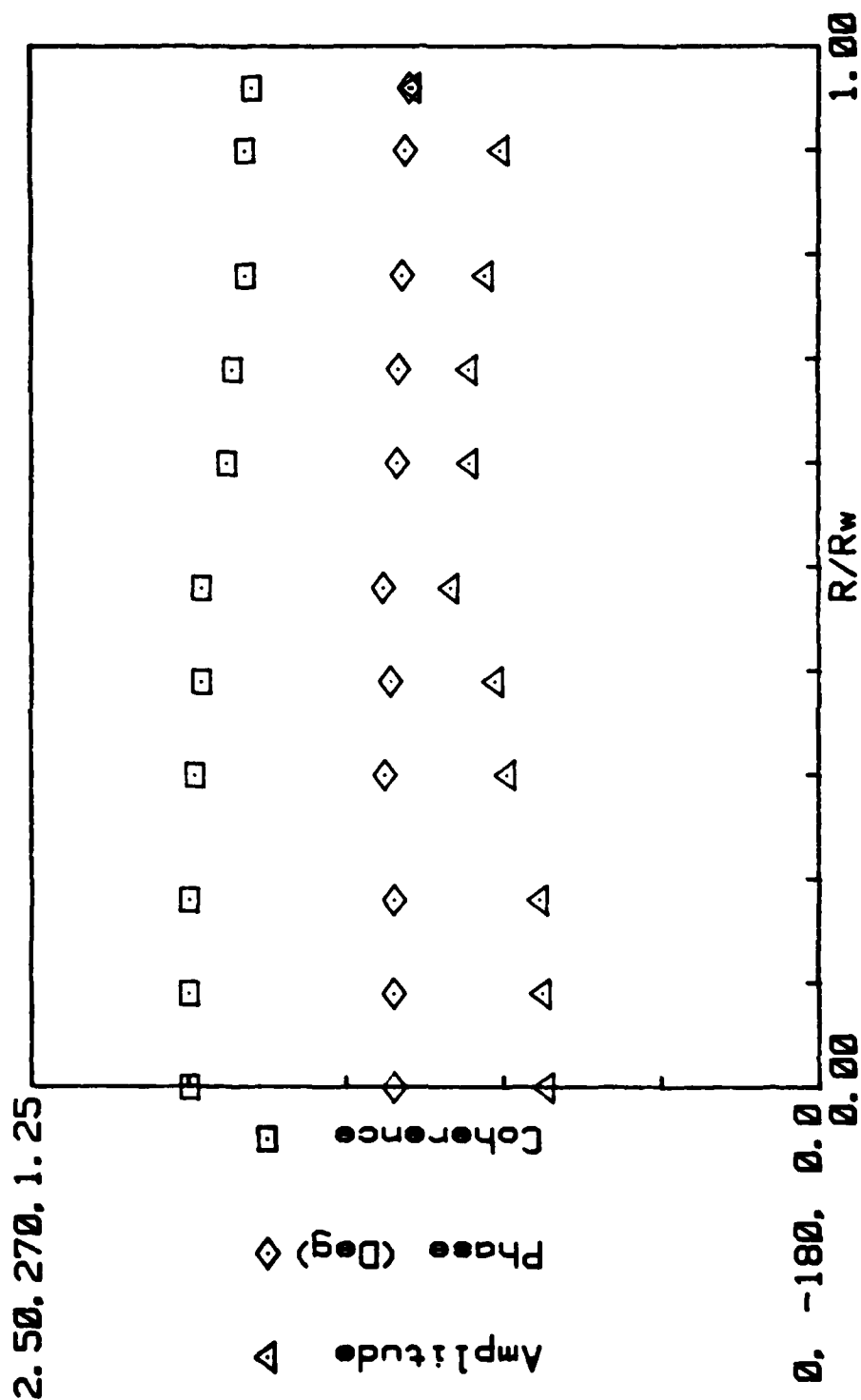
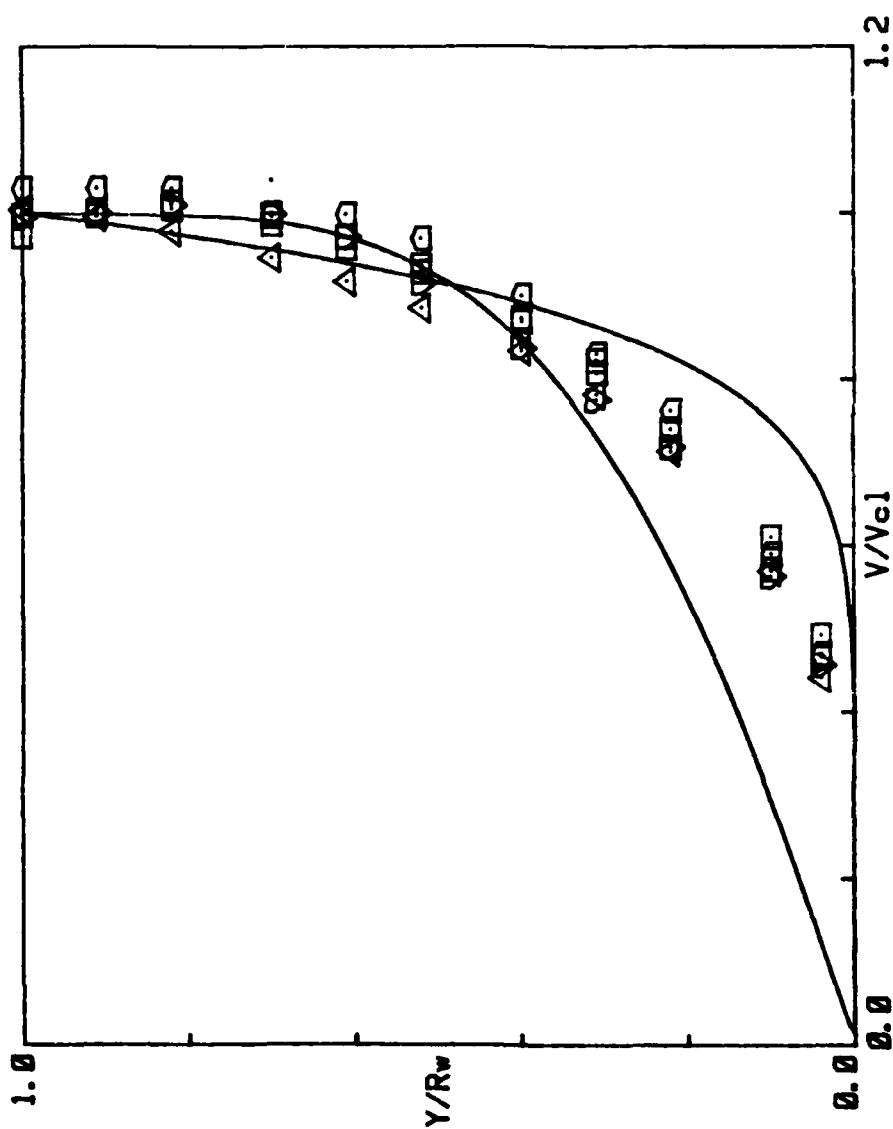


Figure C-10.

MEAN VELOCITY PROFILE



$Z/D = 11.50$

$M_s = 0.001800$

SYM	A/A_t	F Hz.
∇	0.00	0
\square	0.60	65
\square	0.60	65
\triangle	3.30	65
\square	3.30	135

Figure C-11.

TURBULENCE INTENSITY PROFILE

Z/D = 11.50 Freq = 0.00 Hz. A/A_t = 0.00 % M_∞10³ = 1.80

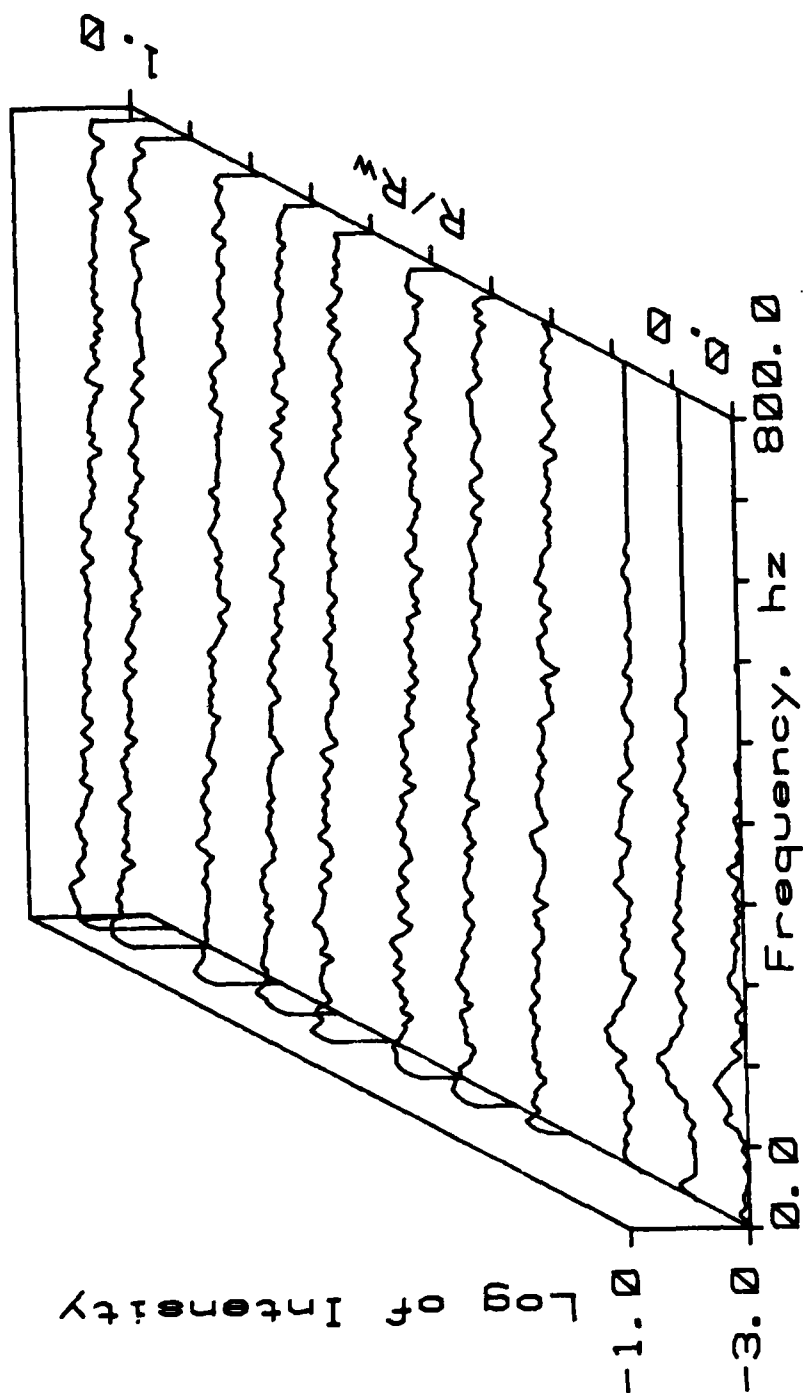


Figure C-12.

TURBULENCE INTENSITY PROFILE

Z/D = 11.50 Freq = 65.00 Hz. A/At = 0.60 % Mex1013 = 1.80

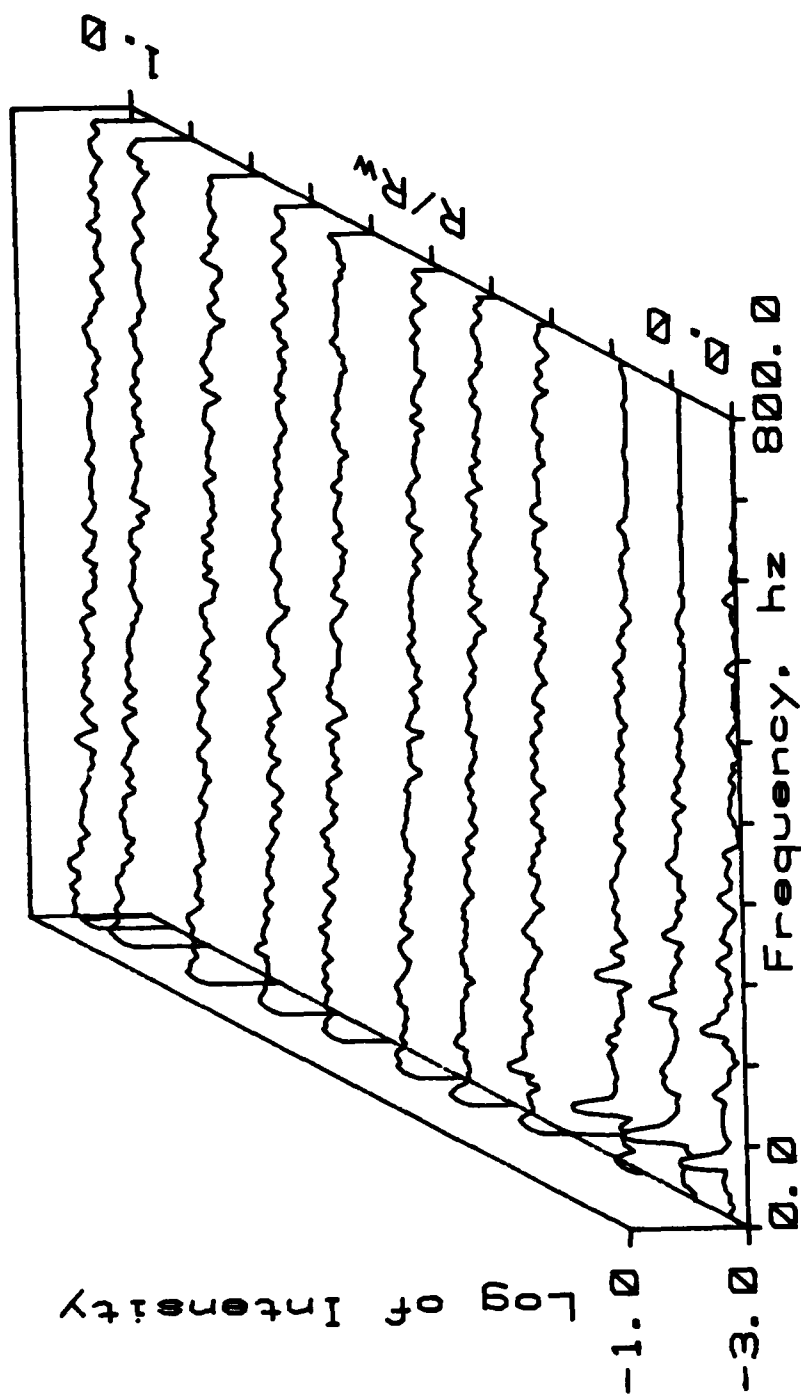


Figure C-13.

TURBULENCE INTENSITY PROFILE

Z/D = 11.50 Freq = 135.00 Hz. A/A_t = 0.60 x M₀10T3 = 1.80

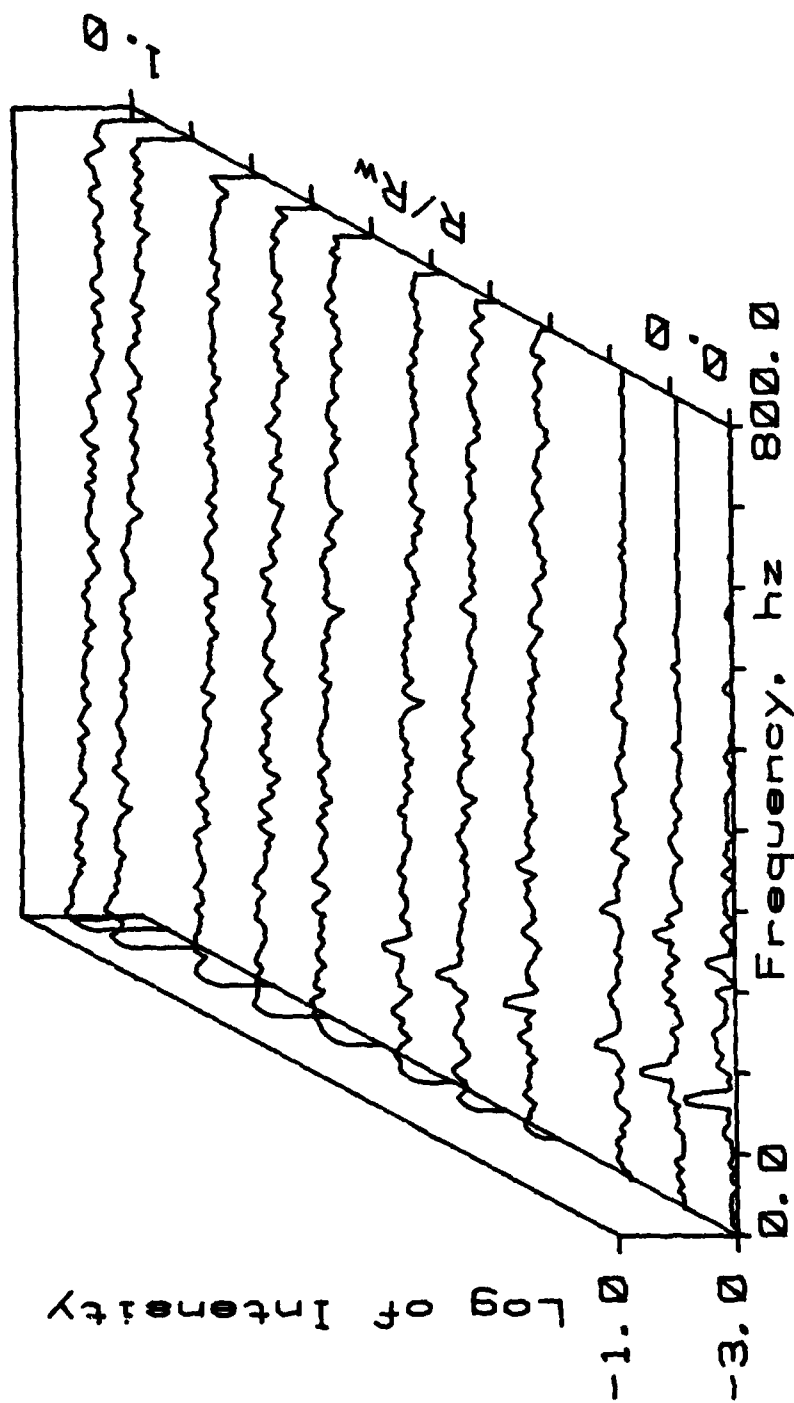


Figure C-14.

TURBULENCE INTENSITY PROFILE

Z/D = 11.50 Freq = 65.00 Hz. $\Delta/\Delta t = 3.30 \times 10^{-3}$ Max10t3 = 1.00

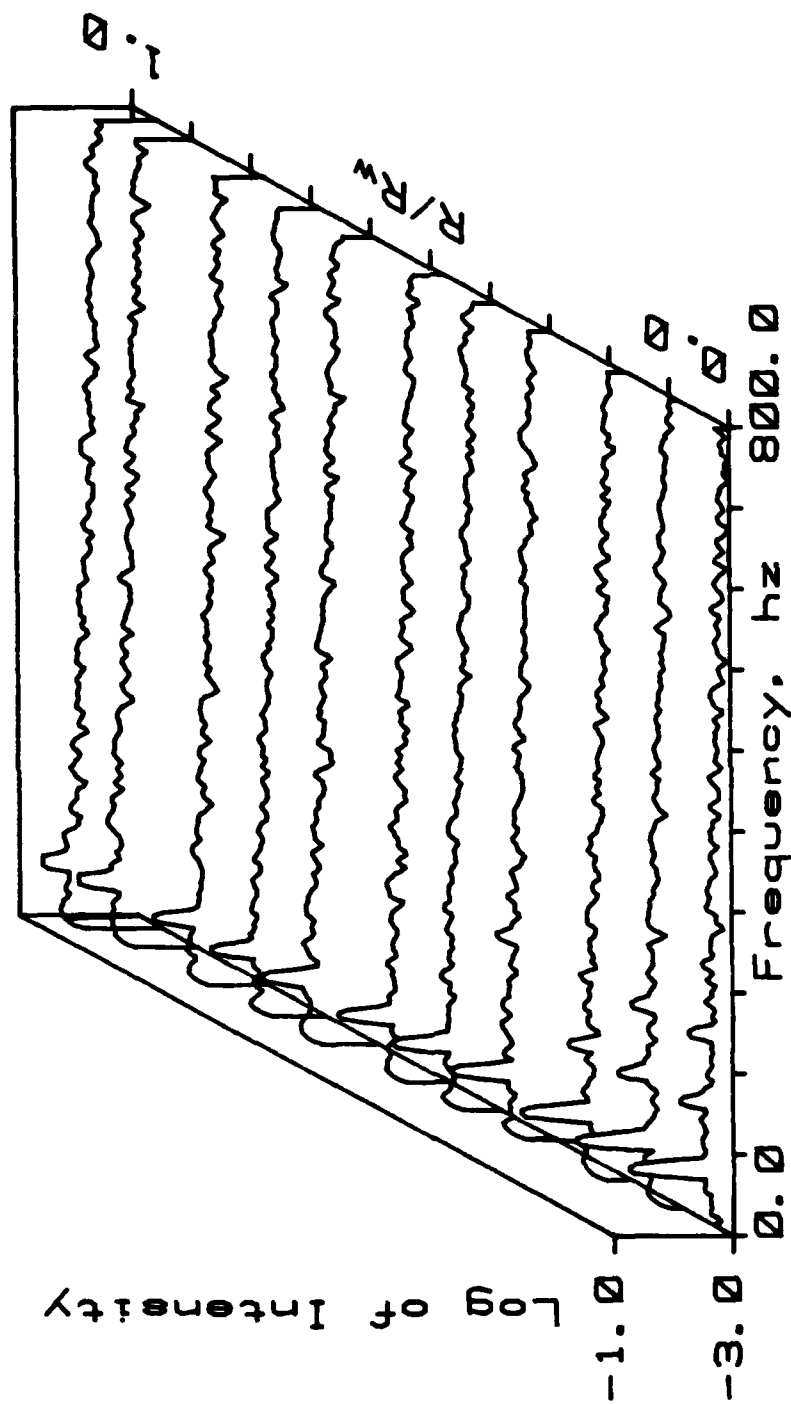


Figure C-15.

TURBULENCE INTENSITY PROFILE

Z/D = 11.50 Freq = 135.00 Hz. $\Delta/\Delta t = 3.30 \times 10^{-3}$ $M \times 10^3 = 1.80$

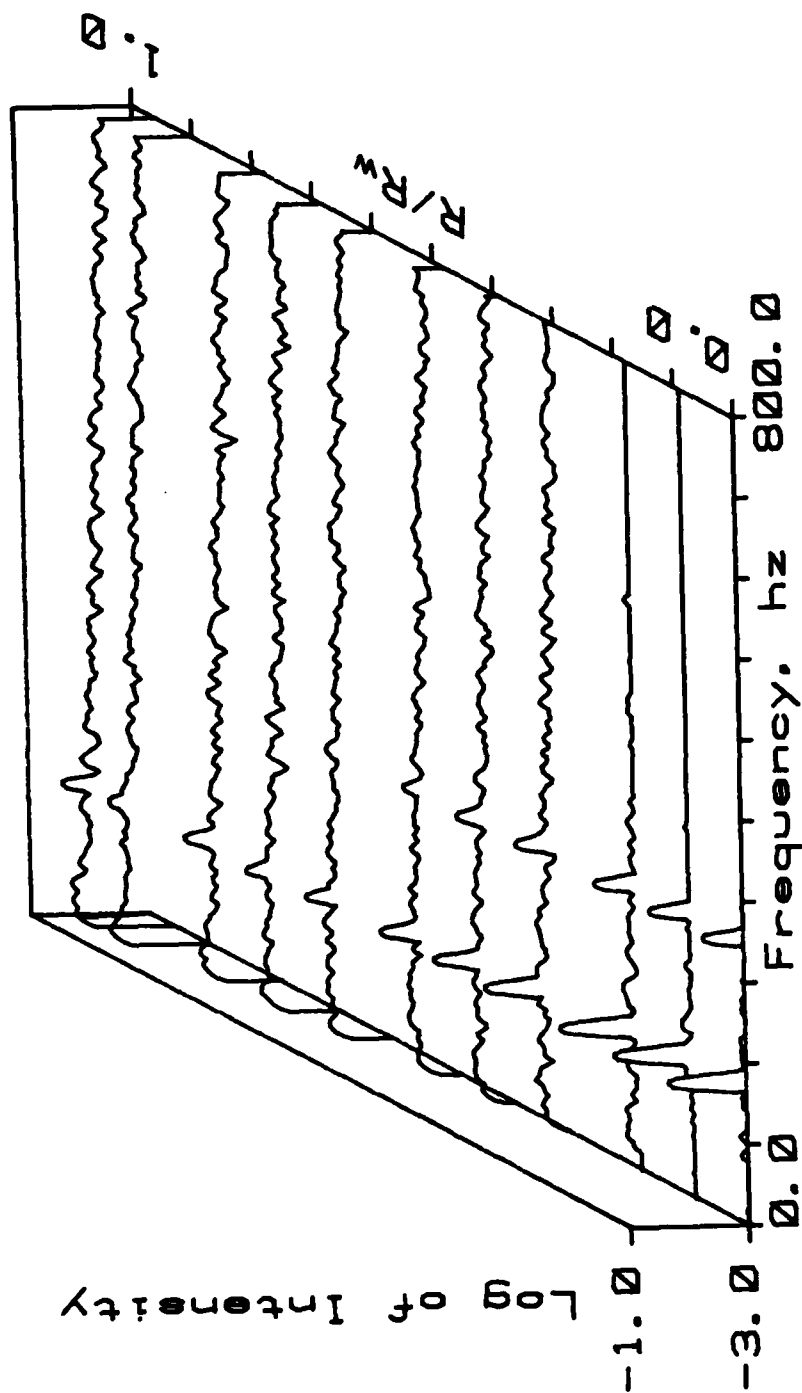


Figure C-16.

NORMALIZED ACOUSTIC VELOCITY PROFILE

Z/D = 11.50 Freq = 65.00 A/Ac = 0.60 x Mex10t3 = 1.00

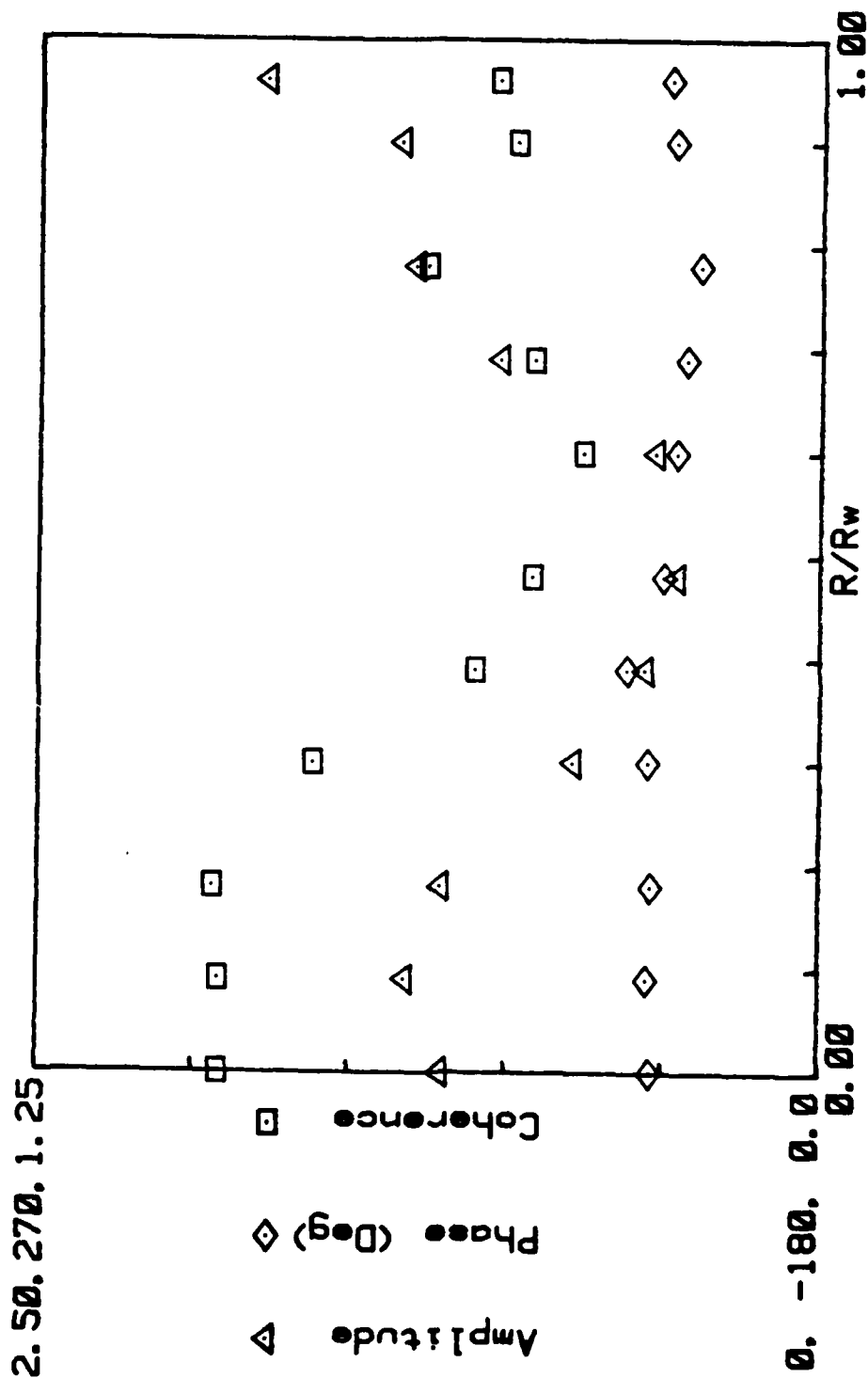


Figure C-17.

NORMALIZED ACOUSTIC VELOCITY PROFILE

Z/D = 11.50 Freq = 135.00 A/Ac = 0.60 X Max10f3 = 1.00

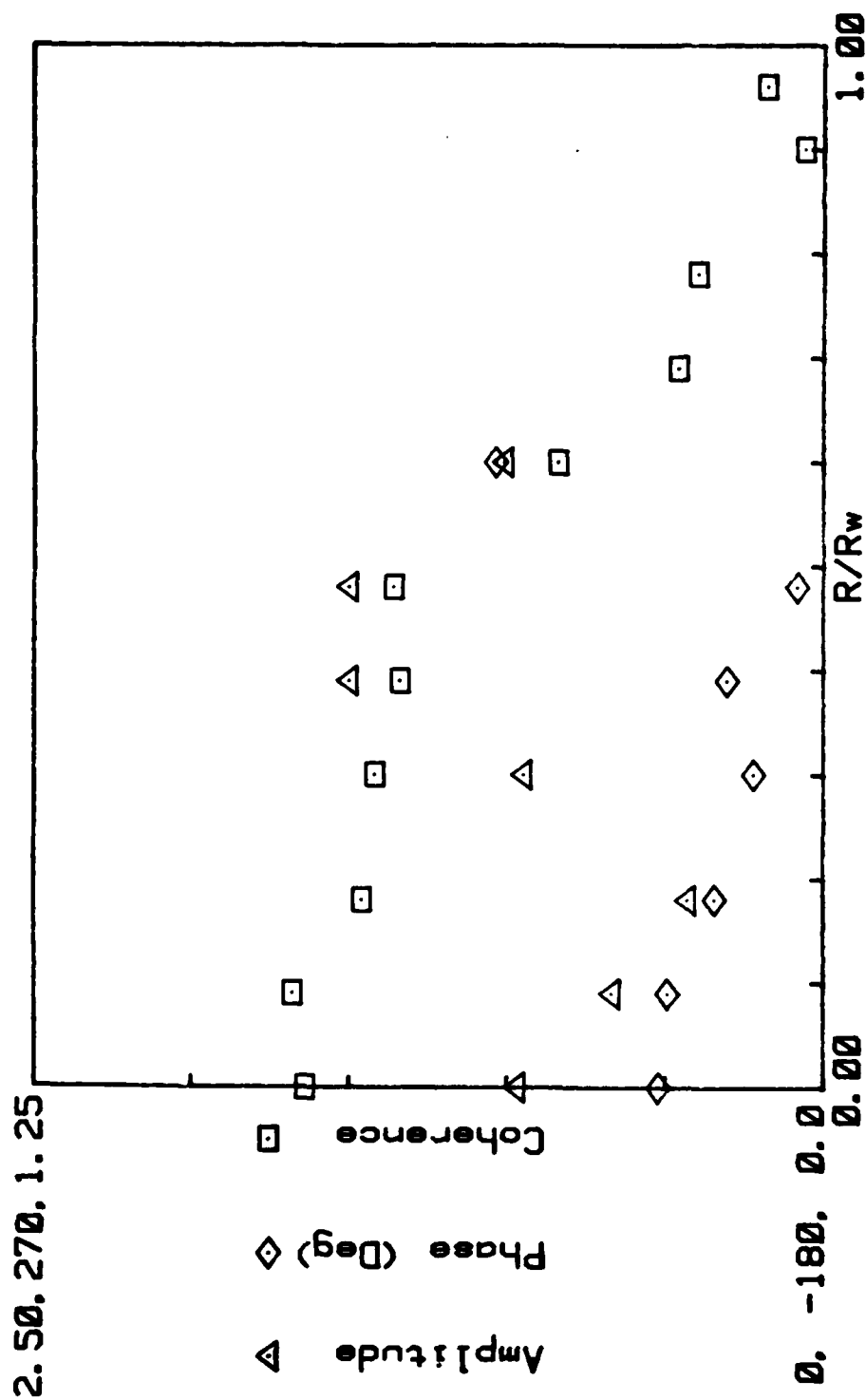


Figure C-18.

NORMALIZED ACOUSTIC VELOCITY PROFILE

Z/D = 11.50 Freq = 65.00 A/Lt = 3.38 x Max18f3 = 1.80

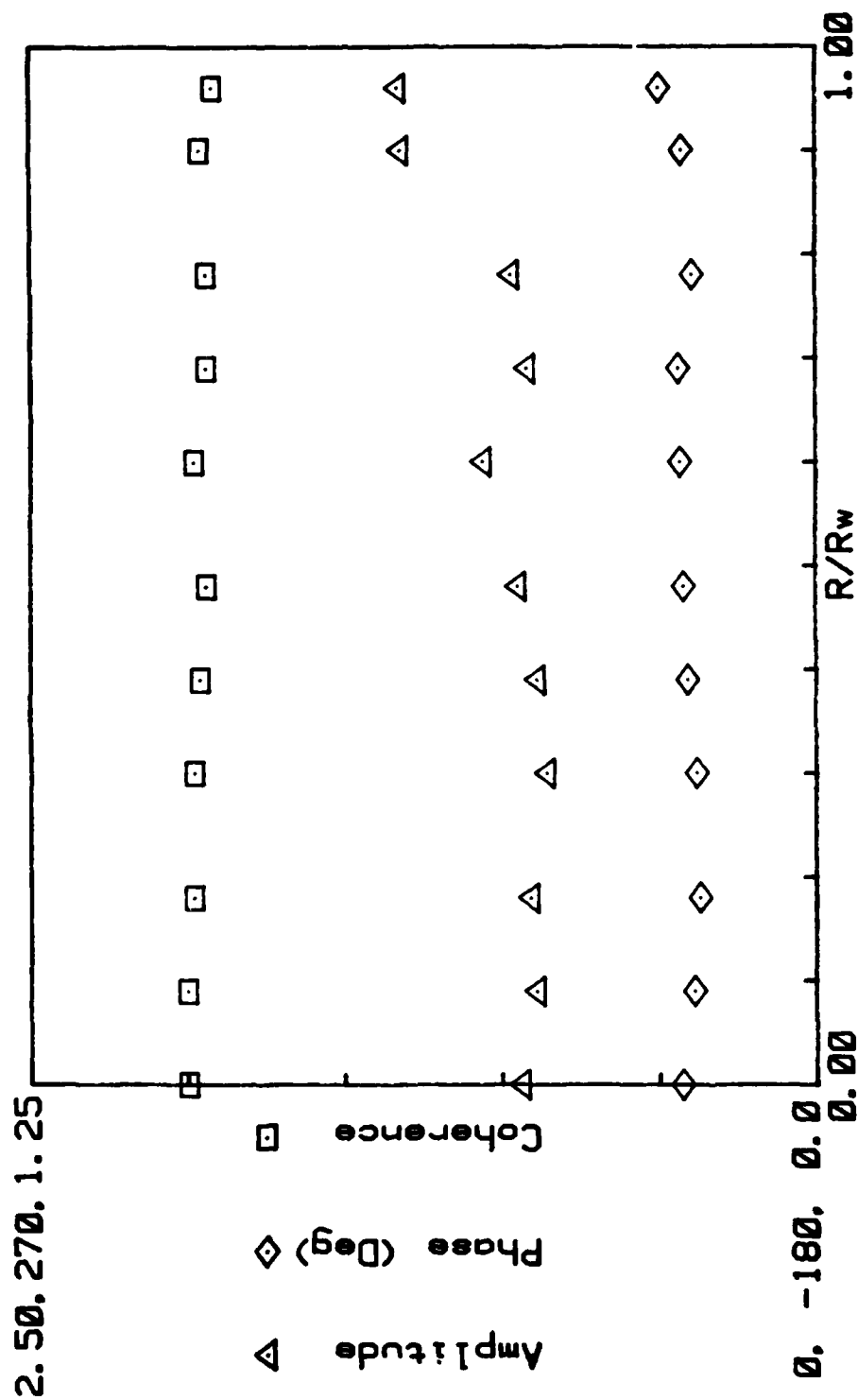


Figure C-19.

NORMALIZED ACOUSTIC VELOCITY PROFILE

Z/D = 11.50 Freq = 135.00 A/Ac = 3.30 X Max1013 = 1.00

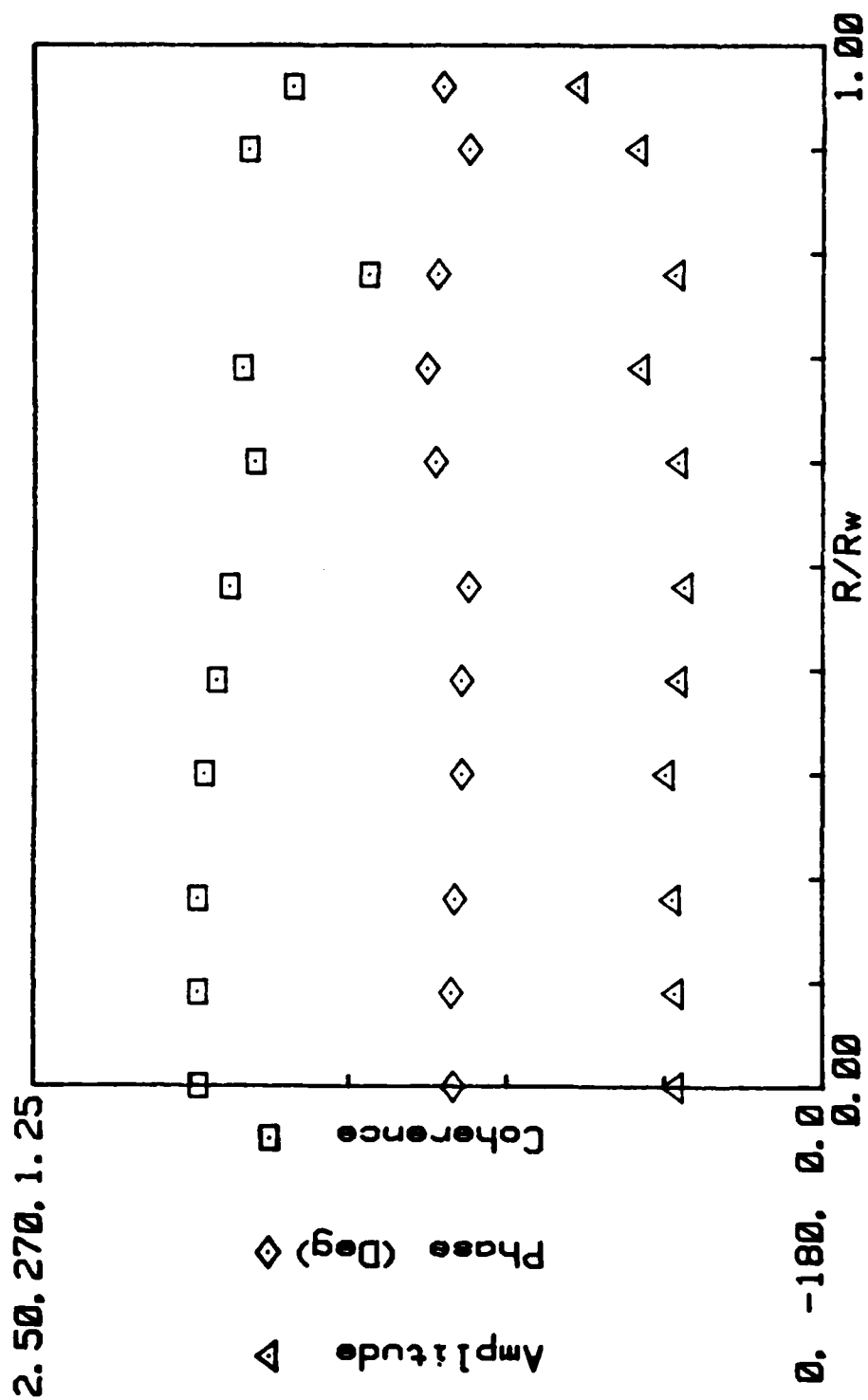


Figure C-20.

END

FILMED

4-85

DTIC